CENTRO DE INVESTIGACIÓN Y DE ESTUDIOS AVANZADOS DEL IPN
Unidad Saltillo

Functionalization of Vulcan and RGO with Ru organometallic compounds: enhanced catalytic activity of Pt/C and Pt/RGO electrocatalysts with Pt–Ru interactions for the Methanol Oxidation Reaction (MOR)

A dissertation submitted in partial satisfaction of the requirements for the degree of:

Doctor en ciencias

In:

Nanociencias y Nanotecnología

By:

M. C. Adriana Angelina Siller Ceniceros

Thesis Advisors:

Dr. Francisco Javier Rodríguez Varela

Dr. María Esther Sánchez Castro

Ramos Arizpe, Coahuila. February/2018

ACKNOWLEDGEMENTS

With eternal gratitude to God, he acts in mysterious ways to keep hope and bravery to carry on.

Likewise, is essential the love of family to understand the motivation to transform big dreams in the reality. My deepest gratitude to my beloved first teachers Mrs. Amelia Ceniceros and Mr. Alonzo Siller to give me magnificent gifts such as love and freedom to take my own choices.

My sincere thanks to Dr. Javier Rodríguez Varela for extraordinary guidance and patience during this years, I really appreciate the clarity of his clever mind to explain a complex work in easy way. Thanks for the opportunity to be part in this extraordinary project and workgroup.

I express my sincere thanks to Dr. Esther Sánchez Castro for her guidance, she is very enthusiastic guide, kind and she has profound understanding in my personal and professional life. Thanks to be a wonderful person and admirable woman.

I would like to thanks to Dr. Eduardo Martínez, Dr. Mario Sánchez, Dr. Roman Torres and Dr. Diana Morales for the experimental help and splendid contributions. I really appreciate your generosity and time.

I greatly thanks to my loved sister Malena and brother Arturo to support my singular way to think. Thanks to be my partners in our life adventures, my admiration and respect.

The life is absolutely better with friendship, thanks to Raquelin, Karitow and Luly to be my soulmates and share magnificent moments, lighting my life.

My admiration and respect to doctors: Amanda Carillo, Martha Rivas, Beatriz Ortega, Maribel Maldonado, Rocío Alfaro, Brenda Cruz, Marlene Andrade and Marcela Mireles to be extraordinary science women. I really appreciate your ingenious tips and skills, you are so brilliant.

I immensely appreciate the versatile way to understand everything, thanks to doctors: Edgar Martínez, Norberto Hernández, Julio Torres, Miguel Sneider, Jorge Ríos, Diego González, Wilian Pech and Daniel Bahena. Thanks to be simple and pragmatic, you are so clever.

I deeply acknowledge the help and support of my partners and friends in Cinvestav: Almita, Luisita, Lalo, Gaby, Fer, Dulze, Anita, Edith, Mara, Karly, Juan Carlos, César, Sylvia, Cande, Antonio, Charlie, Fercho, Ivonne, Maritere, Samuel, Perlita, Nora, Ana Laura, Carlos, Mary, Gaby, Gera, Homero, Trini, Flora, Pablito and Juanito. Thanks gays, your help and support were essentials to convert long work in enjoyable work.

Finally, thanks to Josué my youngest partner and friend, thanks to be the extraordinary lab beginner, and give me the opportunity to start the tremendous work to teach for the first time. And remember, common sense is not so common.

ABSTRACT

In this work, a novel procedure is showing to enhance the electrocatalytic activity for the oxidation reaction of methanol (MOR), which is caused by the interactions of metal Pt–Ru that are present in the electrocatalyst of type *Pt/C* (C, Vulcan XC–72) and *Pt/RGO* (RGO, graphene oxide reduced). To carry out the synthesis of the electrocatalyst, carbonaceous supports were used previously functionalized with ruthenium compounds.
In the first stage, the carbonaceous material C is functionalized with the organometallic compound $[\eta^6–C_6H_5OCH_2CH_2OH)RuCl_2]_2$ (*Ru–dim*), this support is compared with the functionalized with $RuCl_3{\cdot}XH_2O$ (*Ru-com*) and non–functionalized Vulcan, the functionalized materials were labeled as $C_{Ru\text{-}dim}$ and $C_{Ru\text{-}com}$. The carbonaceous supports are later used in the synthesis by polyol method of the electrocatalyst $Pt/C_{Ru\text{-}dim}$, $Pt/C_{Ru\text{-}com}$ and *Pt/C*.
The analysis carried out of the functionalized supports, using the infrared and Raman spectroscopy showed that the functionalization with the ruthenium compounds $C_{Ru\text{-}dim}$ and $C_{Ru\text{-}com}$ maintain the electronic sp^2 hybridization of graphitic segment of the Vulcan.

Furthermore, the results of the physicochemical characterization using the technique of X–ray diffraction (XRD) of the electrocatalyst $Pt/C_{Ru\text{-}dim}$ and $Pt/C_{Ru\text{-}com}$, suggest the formation of the Pt–Ru alloy, the results demonstrated ~50 % of ruthenium platinum alloy in both cases. The electrochemical characterization displayed through the of cyclic voltammetry technique for the ROM, the lowest on–set potential and the higher current density obtained to the electrocatalyst $Pt/C_{Ru\text{-}dim}$ compared with $Pt/C_{Ru\text{-}com}$ and *Pt/C*. Later, during the test of CO–stripping, the $Pt/C_{Ru\text{-}dim}$ exhibited the lowest on–set potential for the oxidation of carbon monoxide (CO), in addition to the presence of at least two species of CO adsorbed (CO_{ads}).

On the other hand, the second stage consisted of the functionalization of nanostructured carbonaceous support RGO, with *Ru–dim*, *Ru-com* and the organometallic compound $[(\eta^6–C_6H_4(CHMe_2)Me)RuCl_2]_2$ (*Ru-cym*). The functionalized supports were labeled as follow: $RGO_{Ru\text{-}dim}$, $RGO_{Ru\text{-}com}$, and $RGO_{Ru\text{-}cym}$. Subsequently, were synthesized the electrocatalyst $Pt/RGO_{Ru\text{-}dim}$, $Pt/RGO_{Ru\text{-}com}$, $Pt/RGO_{Ru\text{-}cym}$ and *Pt/RGO* by the polyol method.
In a similar way to the first stage, the results of the physicochemical characterization of the functionalized supports: $RGO_{Ru\text{-}dim}$, $RGO_{Ru\text{-}com}$, and $RGO_{Ru\text{-}cym}$, demonstrated the preservation of the hybridization sp^2, it promoted the constructive rehybridization avoiding the formation of hybridization sp^3 that creates defects in the RGO lattice.

The physicochemical characterization via XRD, electronic transmission electron microscopy (TEM), among others, showed the formation of the Pt–Ru alloy in the electrocatalysts: $Pt/RGO_{Ru\text{-}dim}$, $Pt/RGO_{Ru\text{-}com}$, and $Pt/RGO_{Ru\text{-}cym}$.

Finally, the electrochemical characterization showed an excellent performance for the electrocatalyst $Pt/RGO_{Ru\text{-}dim}$, compared with $Pt/RGO_{Ru\text{-}com}$, $Pt/RGO_{Ru\text{-}cym}$ and *Pt/RGO*. For example, in the test of cyclic voltammetry for the ROM, the $Pt/RGO_{Ru\text{-}dim}$ obtained the maximum value of current density and the lowest on–set potential, compared with $Pt/RGO_{Ru\text{-}com}$, $Pt/RGO_{Ru\text{-}cym}$ and *Pt/RGO*.

In summary, the electrocatalysts $Pt/C_{Ru\text{-}dim}$ and $Pt/RGO_{Ru\text{-}dim}$ show an improvement in the electrocatalytic properties for the application in direct methanol fuel cells (DMFCs).

RESUMEN

En el presente trabajo se muestra un nuevo procedimiento para mejorar la actividad electrocatalítica para la reacción de oxidación de metanol (MOR), que es originada por las interacciones metálicas Pt–Ru que están presentes en los electrocatalizadores del tipo *Pt/C* (C, Vulcan XC–72) y *Pt/RGO* (RGO óxido de grafeno reducido, por sus siglas en inglés). Para llevar a cabo la síntesis de los electrocatalizadores, se emplearon soportes carbonosos previamente funcionalizados con compuestos de rutenio.

En la primera etapa, el material carbonoso C es funcionalizado con el compuesto organometálico $[\eta^6–C_6H_5OCH_2CH_2OH)RuCl_2]_2$ (*Ru–dim*), este soporte es comparado con el funcionalizado con $RuCl_3{\cdot}XH_2O$ (*Ru–com*) y el Vulcan sin funcionalizar, los materiales resultantes fueron denominados $C_{Ru\text{-}dim}$ y $C_{Ru\text{-}com}$. Los soportes carbonosos se usaron posteriormente en la síntesis de los electrocatalizadores $Pt/C_{Ru\text{-}dim}$, $Pt/C_{Ru\text{-}com}$ y *Pt/C*, mediante la técnica de poliol.

Los análisis llevados a cabo en los soportes mediante las espectroscopías Infrarrojo y Raman muestran que la funcionalización con los compuestos de rutenio de $C_{Ru\text{-}dim}$ y $C_{Ru\text{-}com}$ mantienen la hibridación electrónica sp^2 del segmento grafitizado del Vulcan.

Por otro lado, los resultados de la caracterización fisicoquímica mediante la técnica de difracción de Rayos–X (XRD, por sus siglas en inglés) de los electrocatalizadores $Pt/C_{Ru\text{-}dim}$ y $Pt/C_{Ru\text{-}com}$, sugieren la formación de la aleación Pt–Ru, los resultados demostraron ~50 % de rutenio aleado al platino en ambos casos.

La caracterización electroquímica mostró a través de la técnica de voltamperometría cíclica para la ROM, el menor potencial de inicio y la mayor densidad de corriente para el electrocatalizador $Pt/C_{Ru\text{-}dim}$ comparado con $Pt/C_{Ru\text{-}com}$ y *Pt/C*. Posteriormente, durante la prueba de CO–stripping, el $Pt/C_{Ru\text{-}dim}$ demostró el menor potencial de inicio para la oxidación de monóxido de carbono (CO), además de la presencia de al menos dos especies de CO adsorbido (CO_{ads}).

Por otra parte, la segunda etapa consistió en la funcionalización del soporte carbonoso nanoestructurado *RGO*, con los compuestos *Ru–dim*, *Ru–com* y el organometálico $[(\eta^6–C_6H_4(CHMe_2)Me)RuCl_2]_2$ (*Ru-cym*). Los soportes funcionalizados fueron nombrados: $RGO_{Ru\text{-}dim}$, $RGO_{Ru\text{-}cym}$ y $RGO_{Ru\text{-}com}$. Posteriormente, se sintetizaron los electrocatalizadores $Pt/RGO_{Ru\text{-}dim}$, $Pt/RGO_{Ru\text{-}cym}$, $Pt/RGO_{Ru\text{-}com}$ y *Pt/RGO* por el método de poliol.

De manera semejante a la primera etapa, los resultados de la caracterización fisicoquímica de los soportes funcionalizados: $RGO_{Ru\text{-}dim}$, $RGO_{Ru\text{-}cym}$ y $RGO_{Ru\text{-}com}$, demostraron la preservación de la hibridación sp^2, es decir, se promovió la rehibridación constructiva evitando la formación de hibridación sp^3 que crea defectos en la red.

La caracterización mediante las técnicas de XRD, microscopía de transmisión electrónica (TEM, por sus siglas en inglés), entre otras, revelan la formación de la aleación Pt–Ru en los electrocatalizadores: $Pt/RGO_{Ru\text{-}dim}$, $Pt/RGO_{Ru\text{-}cym}$, $Pt/RGO_{Ru\text{-}com}$.

Finalmente, las pruebas electroquímicas revelaron el mejor desempeño para el electrocatalizador $Pt/RGO_{Ru\text{-}dim}$, comparado con $Pt/RGO_{Ru\text{-}cym}$, $Pt/RGO_{Ru\text{-}com}$ y Pt/RGO. Por ejemplo, en la prueba de voltamperometría cíclica para la ROM, el $Pt/RGO_{Ru\text{-}dim}$ obtuvo el máximo valor de densidad de corriente y el potencial de inicio menor, comparado con $Pt/RGO_{Ru\text{-}cym}$, $Pt/RGO_{Ru\text{-}com}$ y Pt/RGO. Asimismo, los electrocatalizadores $Pt/RGO_{Ru\text{-}dim}$ y $Pt/RGO_{Ru\text{-}cym}$ mostraron excelente tolerancia a la adsorción de especies CO(ads), en la prueba de CO–stripping.

En resumen, los electrocatalizadores $Pt/C_{Ru\text{-}dim}$ y $Pt/RGO_{Ru\text{-}dim}$ muestran una mejora en las propiedades electrocatalíticas para la aplicación en celdas de combustible de metanol directo (DMFCs, por sus siglas en inglés).

CONTENT

LIST OF ABBREVIATIONS

PEMFCs: Proton–exchange membrane fuel cells

DMFCs: Direct Methanol fuel cells

Ru–dim: Organometallic ruthenium compound $[(\eta^6\text{-}C_6H_5OCH_2CH_2OH)RuCl_2]_2$

Ru–cym: Organometallic ruthenium compound $[(\eta^6\text{-}C_6H_4(CHMe_2)Me)RuCl_2]_2$

Ru–com: Commercial salt $RuCl_3{\cdot}XH_2O$

C: Vulcan–XC 72

$C_{Ru\text{-}dim}$: Vulcan functionalized with *Ru–dim*

$C_{Ru\text{-}com}$: Vulcan functionalized with *Ru–com*

Pt/$C_{Ru\text{-}dim}$: Platinum electrocatalyst supported on $C_{Ru\text{-}dim}$

Pt/$C_{Ru\text{-}com}$: Platinum electrocatalyst supported on $C_{Ru\text{-}com}$

RGO: Reduced graphene oxide

$RGO_{Ru\text{-}dim}$: Reduced graphene oxide functionalized with *Ru–dim*

$RGO_{Ru\text{-}cym}$: Reduced graphene oxide functionalized with *Ru–cym*

$RGO_{Ru\text{-}com}$: Reduced graphene oxide functionalized with *Ru–com*

Pt/$RGO_{Ru\text{-}dim}$: Platinum electrocatalyst supported on $RGO_{Ru\text{-}dim}$

Pt/$RGO_{Ru\text{-}cym}$: Platinum electrocatalyst supported on $RGO_{Ru\text{-}cym}$

Pt/$RGO_{Ru\text{-}com}$: Platinum electrocatalyst supported on $RGO_{Ru\text{-}com}$

ROM: Methanol Oxidation Reaction

b.p: boiling point

m.p: melting point

^{1}H–NMR: Proton Nuclear Magnetic Resonance Spectrometry

FT–IR: Fourier Transformed Infrared Spectroscopy

Raman: Raman Spectroscopy

XRD: X-Ray Diffraction

FWHM: Full width at half maximum

d: Crystallite size

D_{planar}: Planar distance (distance between fringes)

a_{fcc}: Lattice parameter of Pt

XPS: X–Ray Photoelectron Spectroscopy

BE: Binding energy (eV)

HR–TEM: High–resolution transmission electron microscopy

SHE: Standard hydrogen electrode

ECSA: The electrochemically active surface area (in $m^2\ mgPt^{-1}$)

H_{ads}: Hydrogen adsorption region

H_{des}: Hydrogen dessorption region

CO_{des}: CO desorption region

CO_{abs}: CO absorbed

Chapter I

1. Background

1.1 Introduction

Nowadays, the electrical energy demand has increased drastically around the world. In addition, the most important energy source in the world is oil, which in turn is a precursor, used to obtain liquid hydrocarbon fuels. However, it is well known that fossil fuels resources are only located in a limited number of countries and its demand has generated a fluctuation on their prices. Another negative issue related to the use of fossil fuels is the emission of carbon dioxide to the atmosphere, a greenhouse gas that significantly participates in the global climate change scenario [1].

In recent years the generation of clean energy has taken a fundamental role for the decrease of the emission of greenhouse gases. Among the alternative energy sources, the following can be mentioned: solar, wind, nuclear and electrochemical.

Considering the environmental benefits, it is imperative to overcome the technical/commercial barriers that limit their wide use and harness the energetic potential of such alternative sources. For these reasons, the world energy council has anticipated a large contribution of renewables and alternative energy sources by 2050, compared with fossil fuels, in the global energy balance [2].

Considering its geographic position, Mexico has an enormous potential to produce energy from renewable sources. Two relevant aspects may promote their wider use in this country: i) the energy reform promoted by the Federal government, which was approved recently by the Congress; and ii) the high atmospheric pollution in most of the main cities. If the energy production scenario in Mexico is analyzed, renewable energy adds up to around 6.98 %, a small number compared to 88.69 % from fossil fuels. Consequently, the Secretary of Energy (SENER), along with other Mexican agencies such as National Council of Science and Technology (CONACYT), offer economic incentives to establish the use of alternative energy sources in domestic and industrial applications, at the same time has been providing the financial resources to research projects in the energy field [3, 4].

Worldwide, one of the most important challenges to develop high performance eco–friendly energy devices is the reduction in infrastructure costs, including those related to components materials and nanometrials [5, 6]. For example, the reduction of platinum catalyst loading or its substitution in the electrodes of the fuel cells is an attractive opportunity to bring this electrical device to commercialization status.

1.2 Fuel cells

The conversion of the chemical energy contained in a fuel into electrical energy is carried out in a device known as fuel cell. Figure 1.1 shows the components of a single proton exchange membrane fuel cell (PEMFC). The electrochemical reactions take place on the electrodes. At the anode, the oxidation of the fuel occurs as hydrogen generating negatively charges electrons that travel though an external circuit, producing an electrical current [7]. On the other side, the oxygen reduction reaction (ORR) is catalyzed at the cathode. An electrolyte, for example Nafion™ as polymeric membrane, transports ions the anode to the cathode, closing the loop. A fuel cell is sustainable energy conversion device that will generate electrical energy continuously as long as a fuel is fed to the anode.

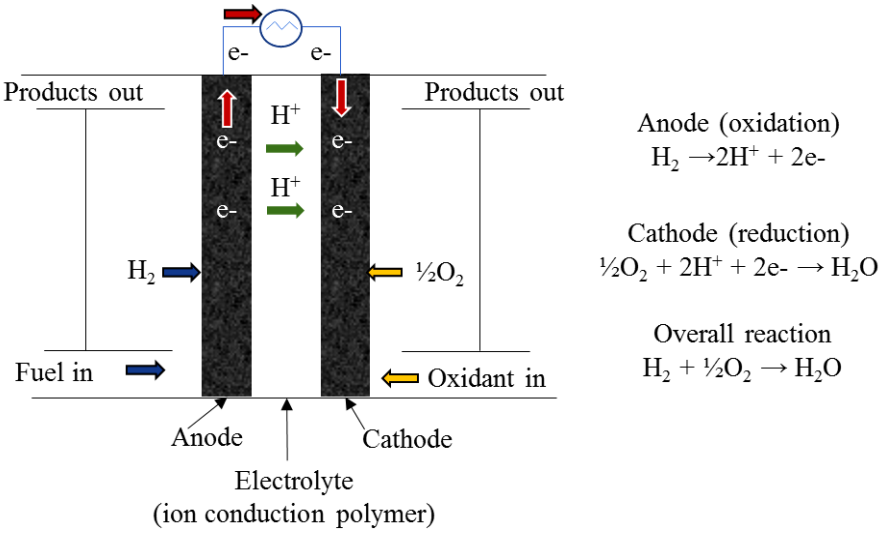

Figure. 1.1 Schematic representation of a single proton exchange membrane fuel cell (PEMFC).

Fuel cells are classified generally according to the electrolyte and the fuel used in the device. In Table 1.1 are shown the different types of fuel cells [8]. According to their characteristics and configuration, fuel cells will have an optimal operating temperature and characteristic plays an important role in potential applications. Recently, Proton Exchange Membrane Fuel Cells (PEMFCs) reveled important benefits in the engineering and operation fields to be employed in automotive technologies. Some of the essential advantages of PEMFCs are: i) low operating temperature, ii) compactness, iii) sustainable cycle–life, and iv) zero or low emissions to the atmosphere [9, 10]. However, one of the main issues to exploit completely the PEMFC technology is the hydrogen fuel storage, since 1 kg of hydrogen at standard temperature and pressure conditions occupies $11m^3$ [11].

Therefore, an attractive technology has been derivate from PEMFCs is the Direct Methanol Fuel Cell (DMFC).

Overall, the main components in both systems are the same, but the DMFCs operate with liquid methanol as fuel. Therefore, instead to the oxidation of hydrogen, the Methanol Oxidation Reaction (MOR) at the anode generates carbon dioxide (CO2) as product along with several reaction intermediates, notably carbon monoxide (CO) [12].

Table 1.1 Classification of different types of fuel cells [8]

Fuel cell type	Mobile ion	Operating temperature	Applications and notes
Alkaline (AFC)	OH^-	50–200°C	Used in space vehicles, e.g. Apollo, Shuttle.
Proton exchange membrane (PEMFC)	H^+	30–100°C	Vehicles and mobile applications, and for lower power CHP systems
Direct methanol (DMFC)	H^+	20–90°C	Suitable for portable electronic systems of low power, running for long times
Phosphoric acid (PAFC)	H^+	~220°C	Large numbers of 200-kW CHP systems in use.
Molten carbonate (MCFC)	CO_3^{2-}	~650°C	Suitable for medium- to large-scale CHP systems, up to MW capacity
Solid oxide (SOFC)	O^{2-}	500–1000°C	Suitable for all sizes of CHP systems, 2 kW to multi-MW.

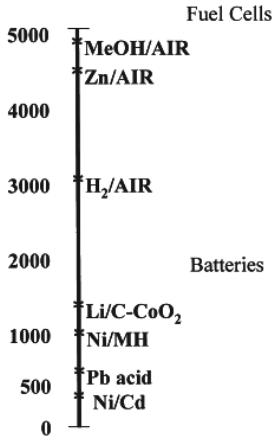

Figure. 1.2 Theoretical volumetric energy density (in Wh L^{-1}) of fuel cells and batteries [13].

In Figure. 1.2 shows the highest theoretical volumetric energy density obtained from several types of fuel cells and batteries [13]. DMFCs have an energy density of ~5000 Wh L^{-1}, higher than PEMFCs and lithium ion batteries (~3000 and 1200 Wh L^{-1}, respectively). The value in Figure 1.2 shown by DMFCs indicates their excellent potential to be employed as power sources in electronic industry and transportation, since the theoretical energy density may be considered as an indirect measure of power availability over time [13].

1.3 Description of the DMFCs

The reactions that occurring at the anode and cathode of a DMFC, as well as the overall reaction in acid media as follows [14, 15]:

Anode reaction: $CH_3OH + H_2O \rightarrow CO_2 + 6H^+ + 6e^- \quad E^0 = 0.046\,V$ (1.1)

Cathode reaction: $^3/_2\,O_2 + 6H^+ + 6e^- \rightarrow 3H_2O \quad E^0 = 1.229\,V$ (1.2)

Overall reaction: $CH_3OH + {}^3/_2\,O_2 \rightarrow CO_2 + 2H_2O \quad EMF = 1.183\,V$ (1.3)

The Gibbs free energy and electromotive force (EMF) of the overall reaction at 25 ºC and 1 atm are [16]: $\Delta G = -686\ kJ\ mol^{-1}$; $EMF = 1.183\,V$ respectively.

Reactions 1.1–1.3 represent ideal oxidation and reduction thermodynamic reactions providing 1.183 V. Therefore, in real conditions the operational voltage of DMFC is significantly lower. In the real case, the MOR is more complex, generating intermediates of several reactions, such as: formic acid, acetic acid, carbonic acid, formaldehyde, acetaldehyde and others as shown in Figure 1.3 [17].

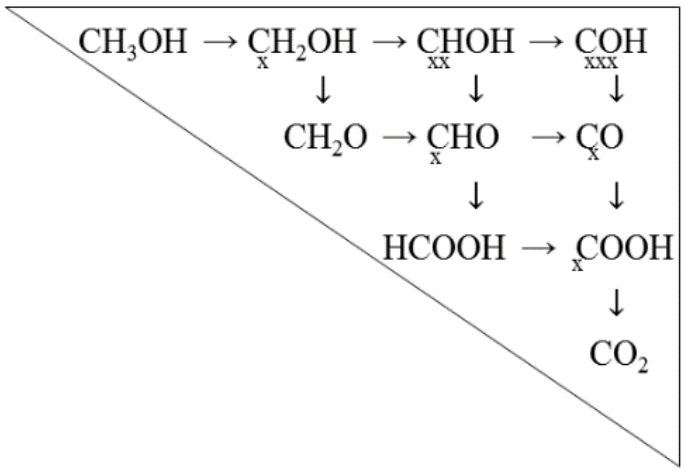

Figure 1. 3 Schematic of the different paths and reaction intermediates that could be obtained during the MOR in acid media.

It is well known that the CO is the most common and poisonous intermediary obtained from the MOR. CO–species strongly adsorb on the surface of fuel cell catalysts blocking the active sites, which are particularly notable for Pt/C, a highly active material for the reaction. At potentials below 450 mV/RHE, the MOR occurs with the adsorption of methanol molecules,

followed by sequential dehydrogenation and electron transfer, producing CO_{ads} (Pt–C≡O) as schematized in Figure 1.4 [18]. As a reference, the degree of surface coverage by CO_{ads} on pristine Pt may be around 90 % [19]. Thus, it is clear that an important challenge for the development of highly efficient DMFCs, is the development of active and innovative catalysts of Pt–based which may promote the MOR at low over potentials, showing a high tolerance to CO_{ads} poisoning effect.

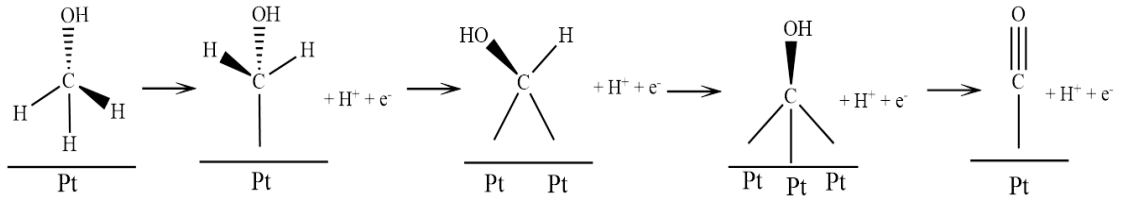

Figure 1.4 Scheme of the reaction mechanism of the methanol oxidation on Pt, resulting in the formation of CO_{ads} [18].

1.4 Enhanced catalytic activity of Pt–Ru/C Electrocatalyst in DMFCs.

The better electrocatalyst for the anode of a hydrogen/oxygen PEMFC is Pt/C. However, in a DMFC the CO–poisoning effect over Pt/C, drastically reduces its electrocatalytic activity during MOR. Pt–Ru/C alloys have demonstrated higher catalytic activity of the MOR and CO tolerance, compared to Pt/C, an enhanced performance attributed to two phenomena: the bifunctional mechanism and the ligand effect [20]. In the former, the water discharge reaction occurs on Ru at lower potentials than on Pt, generating OH^- species. Such oxygenated species oxidize the CO-species adsorbed on neighboring Pt sites to produce CO_2, allowing Pt to continue with the MOR according to the following reactions [20, 21]:

$$\mathrm{Pt} + CH_3 - OH \quad \rightarrow \quad Pt(CO)_{ads} + 4H^+ + 4e^- \quad (\mathrm{CO}\ adsorption) \quad (1.4)$$

$$\mathrm{Ru} + H_2O \quad \rightarrow \quad Ru(OH^-)_{ads} + H^+ + 1e^- \quad (H_2O\ discharge) \quad (1.5)$$

$$Pt(CO)_{ads} + Ru(OH^-)_{ads} \rightarrow Ru + Pt + CO_2 \uparrow + H^+ + 1e^- \quad (CO_2\ delivery) \quad (1.6)$$

Accordingly, in the MOR mechanism occurring on Pt–Ru/C electrocatalyst, the $Ru(OH^-)$ species appear at more negative potentials relative to Pt/C, overlapping with the potentials at

which CO_{ads} is formed. Under these conditions, Pt–Ru/C alloys have the positive effect of easily removing CO_{ads}, and avoiding the poisoning of the electrocatalyst surface. Figure 1.5 shows a scheme of these reactions [21].

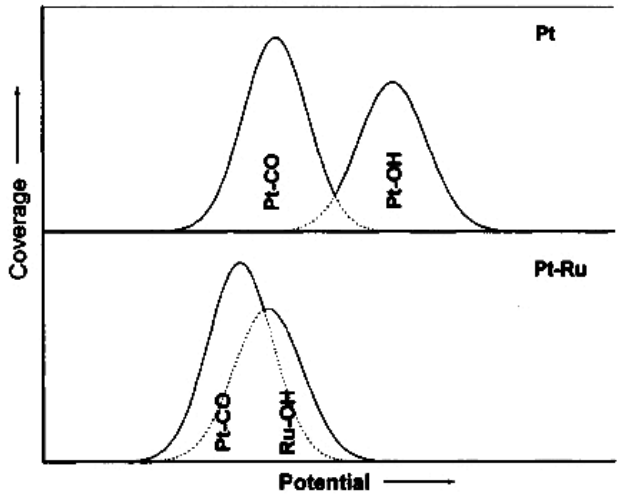

Figure 1.5 Formation of $Ru(OH^-)$ species at Pt–Ru/C, promoting the oxidation of CO_{ads} at more negative potentials compared to Pt/C [21].

Pt-Ru interactions are commonly achieved by simultaneously reducing, with the aid of a suitable chemical agent, the Pt and Ru precursors to form alloyed Pt–Ru nanoparticles anchored to a carbon support [22–25].

Meanwhile, in recent years the concept of functionalization of carbon structures has an special attention, because the morphological and electrocatalytical characteristics of fuel cell nanocatalysts can be enhanced by the surface modification of the supports [26–28]. A synergistic effect between the metallic catalyst and the functional groups on the support, has been identified as one of the main factors for the enhancement in catalytic activity [29].

1.4.1 Methodologies for the synthesis of Pt–Ru/C nanoparticles

The electrochemical activity of Pt–Ru/C catalyst is strongly affected by several characteristics: composition, structure, morphology, particle size, and degree of alloying. These properties and type of Pt:Ru interactions are influenced by the synthesis method [30] Bimetallic Pt–Ru/C catalysts with different configurations and Pt:Ru interactions have been developed and can be described as alloy, core-shell or linked monometallic nanoparticles [31].

Typically, the Pt–Ru interactions are commonly obtained by simultaneous reduction process, with the aid of an appropriate chemical agent, the Pt and Ru precursors to form alloyed Pt–Ru nanoparticles anchored on a carbon support [32–35]. Nanostructural properties as specific surface area to this type of catalysts plays an important role, where a high number of Pt and Ru active sites interact, increasing the catalytic activity for the MOR compared to monometallic Pt due to the already discussed bifunctional mechanism and ligand effect. Some widely used experimental methods for the synthesis of Pt–Ru/C (and Pt/C) nanoparticles as impregnation, colloidal, micro emulsion or Bönnemann [36–38]. Each of them has advantages and disadvantages that may have an effect on the properties of Pt–Ru/C catalysts.

Among the different impregnation procedures to obtain fuel cells catalysts, the polyol method is recognized to control the particle size growth and to promote a homogeneous dispersion of nanoparticles over carbon support. The conventional polyol method consists in the reduction of a metallic precursor in this case hexachloroplatinic acid ($H_2PtCl_6 \cdot (H_2O)_6$) employing ethylene glycol (EG) as reduction agent. The EG completely dissolves the metallic precursor and the solution is fixed to pH = 12, and then the temperature of the solution is increased to boiling point (b. p.) of EG, because it is a soft reducing agent and is necessary to apply thermal energy to accelerate the reduction of $H_2PtCl_6 \cdot (H_2O)_6$ in alkaline media. The reaction mechanism described in literature is displayed as follows [38]:

$$\text{(dehydration reaction)}$$

$$CH_2OH - CH_2OH \quad \rightarrow \quad CH_3 - CHO + H_2O \quad (1.7)$$

$$\text{(acid} - \text{base, reaction } pK_a = 6.5)$$

$$CH_2OH - CH_2OH + 2OH \cdot \rightarrow CH_2OH - CH_2O \cdot + H_2O \quad (1.8)$$

$$\text{(reduction reaction, M = Pt)}$$

$$MO_2 + 4CH_3CHO \rightarrow M + 2\,CH_3 - (CO)_2 - CH_3 + 2H_2O \quad (1.9)$$

The soft conditions favor small size of particles growth. This process is stopped due to two phenomena: i) the absorption reaction by–products over Pt surface, (predominantly, glycolates exhibited in reaction 1.8), and ii) reduction of the metallic precursor (showed in reaction 1.9). Additionally, the glycolate ligand formed in reaction 1.8 interacts weakly with specific crystalline planes of platinum nanoparticles, obtaining nanoparticles with preferential crystal plane orientation [38].

1.5 Graphitic carbon systems as supports of fuel cell electrocatalysts

A. G. Werner applied the term graphite for the first time in 1789 [39]. The elemental structure of six carbons forming regular rings and their bonding with other rings generate large planar layers. Van deer Waals forces of about 0.2 eV $atom^{-1}$ link the layers in the crystal formation a graphitic structure. Figure 1.6 displays graphite spatial arrangement and elemental parameters such as sp^2 hybridization from π bond of C=C. These characteristics result in ordered planar layers of graphite [39, 40].

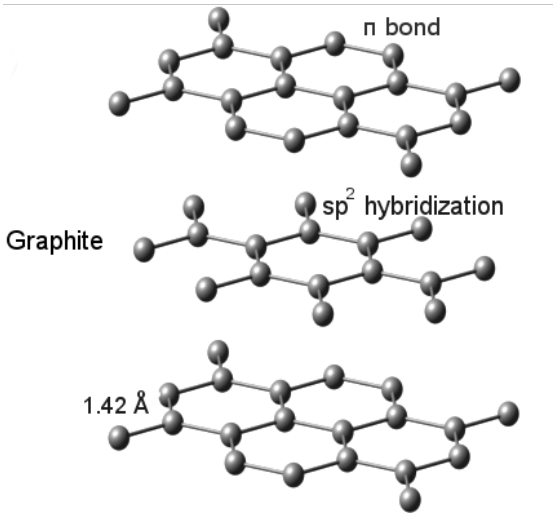

Figure 1.6. Structure and genetics characteristics of graphite

Fuel cell electrocatalysts require of the suitable graphitic carbon support to disperse the metallic nanoparticles and create a large surface area to promote the electrochemical reactions. Carbonaceous materials such as carbon black, activated carbon, coal, and other carbon nanostructures are the most employed supports to anchor metallic nanoparticles for fuel cell applications. These carbons have large surface area, high crystallinity, high chemical composition and thermal stability, and adequate porosity [41, 42]

However, besides their structural properties, in most cases graphitic carbons need to activate their surface (activated carbon support) to become hydrophilic and be able to appropriately anchor metallic nanoparticles.

1.5.1 Vulcan XC–72

Vulcan XC–72 (C) is a mesoporous graphitic carbon black, and this material is the most popular carbon support in PEM and DMFCs applications (see Figure 1.7). Cabot Corporation is the supplier of this carbonaceous waste obtained from aromatic waste oil found in petroleum refineries. The relevance of this graphitic support consists in the presence of native surface oxygen functional groups; therefore, it is not required to carried out a functionalization process. Such a surface composition makes Vulcan an excellent hydrophilic support favoring a good dispersion and anchorage of metal nanoparticles [43, 44].

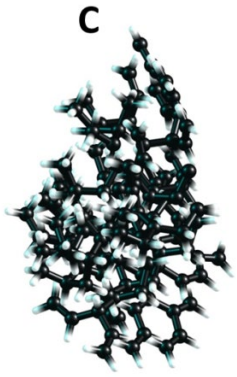

Figure 1.7 Schematic representation of Vulcan XC-72 (C) structure.

1.5.2 Nanostructured support, Reduced Graphene Oxide (RGO)

Nowadays, an attractive option to carbon supports to be functional in Fuel cells applications is the incorporation of nanostructured carbon support, due to the characteristics such as: large surface area, excellent conductivity and mechanical properties [45].

Moreover, Graphene (G) is a novel carbon structure reported for the first time in 2004 and described as isolated monocrystalline graphitic layer with extraordinary electronic behavior and large surface area [46, 47]. The hexagonal carbon structure of graphene is integrated by C=C and C-C conjugated bonds, and possesses sp^2 and σ hybridization bonds likewise aromatic ring. Additionally, it has a half filled π orbital, this half-filled π orbital is perpendicular to the graphene layer, which promotes its semimetal or transition metal electronic behavior [48]. This material represents the basic structure for the construction of other carbon assemblies, such as 0D buckyballs, 1D nanotubes and 3D graphite [49]. However, carbon nanostructures need to be functionalized to create molecular interactions with metallic nanoparticles to be available in fuel cells applications.

On the other hand, there are carbon nanostructures such as graphene oxide (GO) and reduced graphene oxide (RGO) that display similar properties to the graphene and are synthesized

using relatively inexpensive chemical methods, obtaining a considerable yield of material [50–52]. Figure 1.8 displays the representation of RGO structure. Moreover, the principal advantage of GO and RGO is the intrinsic functional groups in the lattice, such as: acid (–COOH), aldehyde (–COH), epoxy (–O–), hydroxyl (–OH) and other oxidized species, this fact helps to create reactive carbon supports.

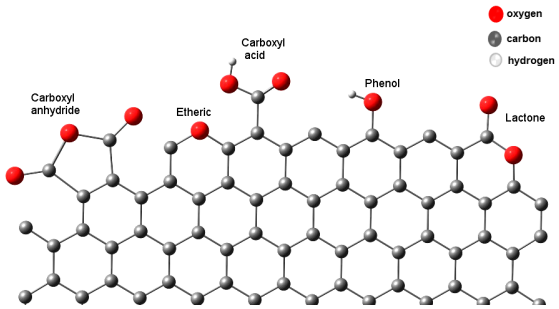

Figure 1.8 Illustration of reduced graphene oxide structure (RGO).

Furthermore, RGO is an attractive material to be applied in fuel cells field due to the duality in its characteristics, from graphene and graphene oxide. RGO carbon nanostructure, displays the sp^2 hybridization inherent of G. The π–orbital from sp^2 hybridization of C=C interacts to d–orbital of platinum, obtaining excellent dispersion of electrocatalyst over RGO surface [53, 54]. This affinity results in overlapping orbital, which create strong interactions or chemical bonds schematized in (Figure 1.9) [55]. Additionally, possess the oxygen functional groups likewise GO to create hydrophilic carbon support and facile interaction with organic fuel during the oxidation process carried out by DMFC [56, 57].

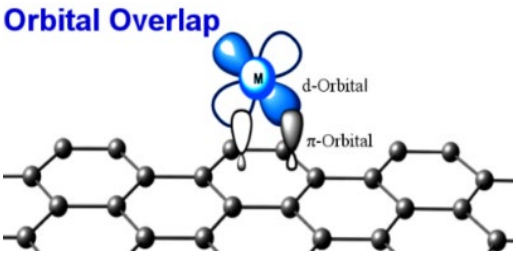

Figure 1.9 Schematic representation of orbital overlapping between a transition metal (d–orbital, Pt) and aromatic ring (π-orbital).

1.6 Functionalization of graphitic carbon supports

According to the above described, the surface functionalization of supports, it is required in most of the cases, in order to enhance the dispersion of metallic nanoparticles and therefore enhance their electrocatalytic performance.

In the case of electrocatalysts for fuel cells, the surface functionalization of nanostructured carbon supports is carried out mainly through three methodologies: i) support modification, generally consisting of a doping process where carbon atoms are displayed by heteroatoms such as nitrogen, boron, sulfur or fluorine [58, 59]; ii) organic functionalization, which involves for example polymeric functionalization of RGO support via non covalent interactions [60, 61], and the oxidation of Vulcan via acidification, employing strong acids with the finality to introduce reactive organic functional groups that promote the anchoring and dispersion of metallic nanoparticles [62]; and iii) Inorganic functionalization, a process involving metal nanoparticles like Au, Ag, Pt, Ru, Pd, Co and others, generating metal carbon hybrids from methods such as microwave treatment, electro less plating, laser irradiation, physical or chemical vapor deposition [63–65].

It is important to note, conversely, that the surface functionalization with aggressive chemicals in some cases modify the electronic structure of the supports, distorting the graphitized lattice of the carbon material and avoiding higher sp^2 rehybridization [66]. This type of chemical modification increases the disorder of the carbons by hybridization due to a shift from sp^2 to sp^3 orbital, which should be avoided in order to have a high–performance support.

Recently, an innovative surface functionalization route of carbon supports route has been proposed [67, 68]. For the first time, Vulcan XC-72 has been functionalized with the ruthenium organometallic complex $[(\eta^6\text{-}C_6H_5OCH_2CH_2OH)RuCl_2]_2$ labeled as Ru–dim. The $C_{Ru\text{-}dim}$ has been employed to synthesize the $Pt/C_{Ru\text{-}dim}$ catalyst. This anode has demonstrated a remarkable catalytic activity for the MOR in terms of onset potential and peak mass current density. It has also shown a high tolerance to CO_{ads}. Also, surface groups have been formed on the Vulcan support, promoting the efficient dispersion of Pt nanoparticles and promoting a synergistic effect between good dispersion and Pt-Ru interactions. The Raman characterization indicated that the graphitized lattice of Vulcan has not been distorted during the formulation of $C_{Ru\text{-}dim}$ [67]. Moreover, XRD and XPS analysis confirmed the formation of Pt–Ru alloyed phases, which improved the performance of $Pt/C_{Ru\text{-}dim}$ for the MOR compared to Pt/C and $Pt/C_{Ru\text{-}com}$ catalyst (Pt supported on Vulcan functionalized with a commercial salt, $RuCl_3 \cdot XH_2O$) [67].

Following the successful functionalization of Vulcan, the next step has been the surface modifications of Reduced Graphene Oxide (RGO) with similar process. Using Ru–dim as the organometallic complex, analogous $Pt/RGO_{Ru\text{-}dim}$ has been synthesized, which also showed a higher catalytic activity for the MOR than Pt/RGO, $Pt/RGO_{Ru\text{-}com}$ catalysts [68]

1.7 Organometallic compounds

The organometallic chemistry is described as "The chemistry of metal-carbon bonds" [69]. Organometallic compounds have one or more metal centers and organic or nonmetallic segments (ligand).

The attraction force that forms the unusual metal–carbon bond (M–C) is typically called coordination compound [70]. According to Werner`s theory, the strength of bonding of the ligand atom (nucleophile) is the coordination number, that is, the number of electrons donated from ligand to the metal (electrophile) [71].

Organometallic complexes have an interesting versatility of chemical properties provided by the metal ligand (M–L) interactions. That is, the electronic, thermodynamic and kinetic characteristics of metal centers (electro acceptor) may be modulated using the suitable ligand (electron donator), producing a chemically stable or reactive compound. Modifications of the metal behavior are attributed to functionality of the ligand to promote different coordination geometries. It is important to mention that the coordination numbers modify the symmetry, length and angle of the M–L bond [72, 73]. As result, key issues in the design of advanced materials are the interatomic interactions of molecular orbital, which may indicate strong or weak attraction between metal ligand.

Molecular orbitals play a significant role to understand the affinity between electron donations from σ or π orbitals of the ligand to electron acceptance into the d–block of transition metals. The electronic M–L interactions may be better understood analyzing Figure 1.10: a) represents an M–C σ–bond of the lone–pair donor from CO ligand; b) shows the orbitals, where the red arrow indicates the electron π–donor from filled π orbital attributed to ethylene, bonding the empty d_π orbitals of the transition metal. Back donation, is schematized with green arrows describing the electron acceptance of d_π orbital of the transition metal to the empty overlapped π^* assigned to C=C bonds; c) the red arrow indicates the electronic interactions of σ–donator orbital from molecular hydrogen, bonding the d_σ orbital with the transition metal orbital. Back donation is similarly indicated by the green arrows, considering the overlapping of filled d_π orbital from the metal to σ^*–orbital attributed to H–H bong [70, 74].

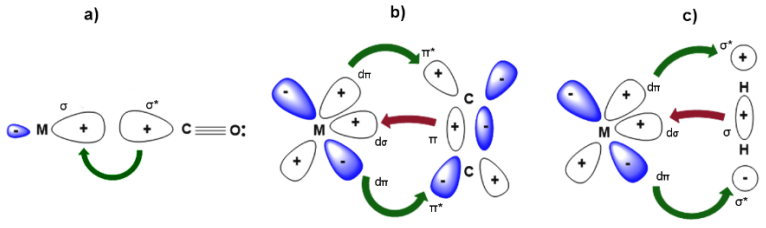

Figure 1.9 a) Lone–pair donor, b) π–bonding electron pair donor, and c) σ–bonding electron pair donor.

The back donation interaction, between π* orbital of carbon with sp2 hybridization and dπ orbital from metal transition showed in Figure 1.10 b), represents an extraordinary opportunity to employ organometallic compounds to interact with unsaturated carbon structures as carbon rings, the elemental units to conform novel carbon nanostructures, such as: carbon nanotubes, fullerenes, graphene and other structures [75–78].

Moreover, transition metals have the capacity to coordinate one or more atoms from carbon structures, a property known as *hapticity* (η) where "the number of atoms of the organic moiety are attached to the metal atom is specified by the appropriated Greek numerical prefix, mono, di, tri, tetra, penta, hexa, hepta, octa, etc." [79]. Specifically, η^6 *hapticity*, corresponds to the coordination of six carbon atoms with the transition metal. In organometallics, six carbons with sp^2 hybridization building a hexagonal ring are also known as "arene". This η^6-arene, π- ligand is structurally analogue to the honeycomb ring that forms the graphitic structures, fostering the η^6 ligands [80].

In recent studies, organometallic complexes of chromium (Cr) such as (η^6–arene)$Cr(CO)_3$ and $Cr(CO)_6$, have been employed to functionalize single-walled carbon nanotubes (SWCNT) and graphene [81–85]. The Cr fulfills the conditions to be η^6-coordinated using empty d_π orbitals to overlap the π orbital from sp^2 hybridization of benzoic rings from carbon nanostructured material [83-86]. As a result, SWCNTs have been functionalized with (η^6-arene)$Cr(CO)_3$ via the coordination with Cr, forming the chemically stable (η^6-arene)$_2$Cr structure, where CO ligands were substituted by the arene ring from the CNTs [87]. Another opportunity to functionalize carbon structures is by using ruthenium atom in the dimeric organometallic complexes, i.e., [(η^6–$C_6H_5OCH_2CH_2OH$) $RuCl_2$]$_2$ and [(η^6–$C_6H_5CH(CH_3)_3$) $RuCl_2$]$_2$. These compounds have similar polymeric structures that promote a complete covering of the carbon surface during functionalization.

Therefore, organometallic transition metals have vast potential for taking advantage of the coordination with graphitic carbon structures. Nevertheless, the wide range of applications using organometallic compounds in electrocatalysis is not completely understood.

References

Chapter I

[1] S. Chu, A. Majumdar. Opportunities and challenges for a sustainable energy future. Nature 488 (2012) 294–303.

[2] J. P. Painuly. Barriers to renewable energy penetration; a framework for analysis. Renew Energy. 24 (2001) 73–89.

[3] M. Jano-Ito, D. Crawford-Browna. Socio-technical analysis of the electricity sector of Mexico: Its historical evolution and implications for a transition towards low-carbon development. Renew Sust Energ Rev. 55 (2016) 567–590.

[4] G. S. Alemán-Nava, V. H. Casiano-Flores, D. L. Cárdenas-Chávez, R. Díaz-Chavez, N. Scarlat, J. Mahlknecht, J-F. Dallemand, R. Parra. Renewable energy research progress in Mexico: A review. Renew Sust Energ Rev. 32 (2014) 140–153.

[5] E. Traversa, H. Idriss. Materials for renewable and sustainable energy provide the connection between materials, energy, and sustainability. Mater Renew Sust Energy. 1 (2012) 1–2.

[6] A. Lavacchi, H. Miller, F. Vizza, Nanotechnology in electrocatalysis for energy, Springer, New York, 2017.

[7] J.H. Hirschenhofer, D.B. Stauffer, R.R. Engleman, M.G. Klett. (Eds.), Fuel cell handbook (Fourth Edition). National Energy Technology Laboratory U.S. 1998, 1–2.

[8] J. Larminie, A. Dicks. (Eds.) Fuel cell systems explained (Second Edition). John Wiley & Sons Ltd, Chichester, England, 2003, pp. 14–16.

[9] A. F. Ghenciu. Review of fuel processing catalysts for hydrogen production in PEM fuel cell systems. Curr. Opin. Solid State Mater. Sci. 6 (2002) 389–399.

[10] D. Garraín, Y. Lechón, C. de la Rúa. Polymer electrolyte membrane fuel cells (PEMFC) in automotive applications: environmental relevance of the manufacturing stage. SGRE 2 (2011) 68–74.

[11] G. Principi, F. Agresti, A. Maddalena, S. Lo Russo. The problem of solid state hydrogen storage. Energy 34 (2009) 2087–2091.

[12] S. Chakraborty, M. G. Simoes, W. E. Kramer. (Eds.) Power Electronics for renewable and distributed energy systems: a sourcebook of topologies, control and integration (green energy and technology). Springer, London, England, 2013, 193–194.

[13] C.K. Dyer. Fuel cells for portable applications. J. Power Sources 106 (2002) 31–34.

[14] H. Liu, J. Zhang. (Ed.) Electrocatalysis of direct methanol fuel cells: from fundamentals and applications. Wiley-VCH Verlag GmbH & Co. KGaA, Weinheim. (2009), pp. 40–60.

[15] J. A. Anderson, M. Fernández García. (Eds.) Supported metals in catalysis (Second edition). Imperial Collage Press, London, England, 2012, 407–493.

16] A. S. Aricò, S. Srinivasan, V. Antonucci. DMFCs: from fundamental aspects to technology development. Fuel Cell, 1 (2001) 133–161.

[17] S. K. Kamarudin, F. Achmad, W. R. W. Daud. Overview on the application of direct methanol fuel cell (DMFC) for portable electronic devices. Int. J. Hydrogen Energy 34 (2009) 6902–6916.

[18] M. P. Hogarth, G. A. Hards. Direct methanol fuel cells: technological advances and further requirements. Platinum Metals Rev. 40 (1996) 150–159.

[19] J. Zhang. PEM fuel cell electrocatalysts and catalyst layers: fundamentals and applications, Springer, London, 2008.

[20] H. Liu, Ch. Song, L. Zhang, J. Zhang, H. Wang, D.P. Wilkinson. A review of anode catalysis in the direct methanol fuel cell. J. Power Sources 155 (2006) 95–110.

[21 R. E. White, C. Vayenas, M. E. Gamboa-Aldeco. Modern aspects of electrochemistry no. 40. Springer, New York, 2007.

[22] T. Maiyalagan, T.O. Alaje, K. Scott, Highly stable Pt–Ru nanoparticles supported on three-dimensional cubic ordered mesoporous carbon (Pt–Ru/CMK-8) as promising electrocatalysts for methanol oxidation, J. Phys. Chem. C 116 (2012) 2630–2638.

[23] J.R.C. Salgado, F. Alcaide, G. Álvarez, L. Calvillo, M.J. Lázaro, E.J. Pastor, Pt–Ru electrocatalysts supported on ordered mesoporous carbon for direct methanol fuel cell, J. Power Sources 195 (2010) 4022–4029.

[24] L. Ren, Y. Xing, Effect of pH on PtRu electrocatalysts prepared via a polyol process on carbon nanotubes, Electrochim. Acta 53 (2008) 5563–5568.

[25] S. Yang, Ch. Zhao, Ch. Ge, X. Dong, X. Liu, Y. Liu, Y. Fang, H. Wang, Z.J. Li, Ternary Pt–Ru–SnO2 hybrid architectures: unique carbon-mediated 1-D configuration and their electrocatalytic activity to methanol oxidation, Mater. Chem. 22 (2012) 7104–7107.

[26] E. Antolini, Carbon supports for low-temperature fuel cell catalysts, Appl. Catal. B: Environ. 88 (2009) 1–25.

[27] L. Calvillo, M.J. Lázar, E. García-Bordejé, R. Moliner, P.L. Cabot, I. Esparbé, E. Pastor, J.J. Quintana, Platinum supported on functionalized ordered mesoporous carbon as electrocatalyst for direct methanol fuel cells, J. Power Sources 169 (2007) 59–64.

[28] A. Capelo, M.A. Esteves, A.I. de Sá, R.A. Silva, L. Cangueiro, A. Almeida, R. Vilar, C.M. Rangel, Stability and durability under potential cycling of Pt/C catalyst with new surface-functionalized carbon support, Int. J. Hydrogen Energy 41 (2016) 12962–12975.

[29] J.R.C. Salgado, R.G. Duarte, L.M. Ilharco, A.M. Botelho do Rego, A.M. Ferraria, M.G.S. Ferreira, Effect of functionalized carbon as Pt electrocatalyst support on the methanol oxidation reaction, Appl. Catal. B: Environ. 102 (2011) 496–504.

[30] D. R. M. Godoi, J. Perez, H. M. Villullas. Influence of Particle Size on the Properties of Pt–Ru/C Catalysts Prepared by a Microemulsion Method J. Electrochem. Soc. 154 5 (2007) B474–B479.

[31] S. Alayoglu, A. U. Nilekar, M. Mavrikakis, B. Eichhorn. Ru–Pt core–shell nanoparticles for preferential oxidation of carbon monoxide in hydrogen. Nat. Mater. 7 (2008) 333–338.

[32] T. Maiyalagan, T.O. Alaje, K. Scott. Highly stable Pt–Ru nanoparticles supported on three-dimensional cubic ordered mesoporous carbon (Pt–Ru/CMK-8) as promising electrocatalysts for methanol oxidation. J. Phys. Chem. C, 116 (2012) 2630–2638.

[33] J.R.C. Salgado, F. Alcaide, G. Álvarez, L. Calvillo, M.J. Lázaro, E.J. Pastor. Pt–Ru electrocatalysts supported on ordered mesoporous carbon for direct methanol fuel cell. J. Power Sources 195 (2010) 4022–4029.

[34] L. Ren, Y. Xing. Effect of pH on PtRu electrocatalysts prepared via a polyol process on carbon nanotubes. Electrochim. Acta 53 (2008) 5563–5568.

[35] S. Yang, Ch. Zhao, Ch. Ge, X. Dong, X. Liu, Y. Liu, Y. Fang, H. Wang, Z.J. Li. Ternary Pt–Ru–SnO_2 hybrid architectures: unique carbon-mediated 1-D configuration and their electrocatalytic activity to methanol oxidation. Mater. Chem. 22 (2012) 7104–7107.

[36] S. L. Suib. New and future developments in catalysis: batteries, hydrogen storage and fuel cells. Elsevier, Netherlands, 2013.

[37] D. P. Wilkinson, J. Zhang, R. Hui, J. Fergus, X. Li. Proton exchange membrane fuel cells. D. Thompsett. Recent developments in electrocatalyst activity and stability for proton exchenge membrane. Fuell Cell. CRS Press USA, 2010.

[38] A. A. Hashim (Ed.), The Delivery of Nanoparticles, InTech, China, 2012, 403–430.

[39] B. Kwiecińskaa, H.I Petersen, Graphite, semi-graphite, natural coke, and natural char classification-ICCP system, Int. J. Coal Geol 57 (2004) 99–116.

[40] D. D. L. Chung, Review Graphite, J. Mater. Sci. 37 (2002) 1475–1489.

[41] E. Antolini. Carbon supports for low-temperature fuel cell catalysts. Appl. Catal., B. – Environ 88 (2009) 1–24.

[42] E. Bailón-García, F. J. Maldonado-Hódar, A. F. Pérez-Cadenas, F. Carrasco-Marín, Catalysts supported on carbon materials for the selective hydrogenation of citral, Catalysts 3 (2013) 853–877.

[43] X. Yu, S. Ye. Recent advances in activity and durability enhancement of Pt/C catalytic cathode in PEMFC: Part I. Physico-chemical and electronic interaction between Pt and carbon support, and activity enhancement of Pt/C catalyst. J. Pow. Sour. 172 (2007) 133–144.

[44] I. J. Sanders, T. L. Peeten (Eds.), Carbon Black: Production, properties and uses: chemical engineering methods and technology materials science and technologies series, Nova Science Publishers, Inc. New York, 2011, 1–27.

[45] P. Trogadas, T. F. Fuller, P. Strasser, Carbon as catalyst and support for electrochemical energy conversion, Carbon 75 (2014) 5–4 2.

[46] K. S. Novoselov, A. K. Geim, S. V. Morozov, D. Jiang, Y. Zhang, S. V. Dubonos, I. V. Grigorieva, A. A. Firsov, Electric field effect in atomically thin carbon films. Science 306 (2004) 666–669.

[47] J. Güttinger, F. Molitor, C. Stampfer, S. Schnez, A. Jacobsen, S. Dröscher, T. Ihn, K. Ensslin. Transport through graphene quantum dots, Rep. Prog. Phys. 75 (2012) 126502 1-24.

[48] A. H. Castro Neto, F. Guinea, N. M. R. Peres, K. S. Novoselov, A. K. Geim, The electronic properties of graphene, Rev. Mod. Phys. 81 (2009) 109–162.

[49] A. K. Geim, K. S. Novoselov, The rise of graphene, Nat. Mater. 6 (2007) 183–191.

[50] S. Pei, H–M Cheng, The reduction of graphene oxide, Carbon, 50 (2012) 3210–3228.

[51] H. Yang, H. Li, J. Zhai, L. Sun, H. Yu, Simple synthesis of graphene oxide using ultrasonic cleaner from expanded graphite, Ind. Eng. Chem. Res. 53 (2014) 17878–17883.

[52] S. N. Alam, N. Sharma, L. Kumar, Synthesis of graphene oxide (GO) by modified hummers method and its thermal reduction to obtain reduced graphene oxide (rGO), Graphene 6 (2017) 1–18.

[53] X. Wang, X. Zhang, X. He, A. Ma, L. Le S. Lin, Facile electrodeposition of flower-like PMo12-Pt/rGO composite with enhanced electrocatalytic activity towards methanol oxidation, Catalysts 5 (2015) 1275–1288.

[54] T. H. Thi–Vu, T. T. Thi –Tran, H. N. Thi–Le, L. T. Tran, P. H. Thi–Nguyen, M. Dang–Nguyen, B. Ngoc–Quynh, Synthesis of Pt/rGO catalysts with two different reducing agents and their methanol electrooxidation activity, Mater Res Bull. 73 (2016) 197–203.

[55] Q. Qi, H. Liu, W. Feng, H. Tian, H. Xu, X. Huang, Theoretical investigation on the interaction of subnano platinum clusters with graphene using DFT methods, Computational Materials Science. 96 (2015) 268–276.

[56] S. Wu, J. Liu, Z. Tian, Y. Cai, Y. Ye, Q. Yuan, Ch. Liang. Highly dispersed ultrafine Pt nanoparticles on reduced graphene oxide nanosheets: in situ sacrificial template synthesis and superior electrocatalytic performance for methanol oxidation, ACS Appl. Mater. Interfaces 7 (2015) 22935−22940.

[57] D. Das, I. Basumallick, S. Ghosh, Methanol and ethanol electro-oxidation on to platinum loaded reduced graphene oxide surface for fuel cell application, Br. J. Appl. Sci. 7 (2015) 630−641.

[58] M. Aliofkhazraei, (Ed.). Advances in graphene science, InTech, Shanghai, 2013, 161−189.

[59] H. Song, L. Yang, Y. Tang, D. Yan, C. Liu, S. Luo, Three-dimensional nitrogen-doped reduced graphene oxide–carbon nanotubes architecture supporting ultrafine palladium nanoparticles for highly efficient methanol electrooxidation, Chem. Eur. J. 21 (2015) 16631–16638.

[60] J. Lu, Y. Li, S. Li, S. P. Jiang, Self–assembled platinum nanoparticles on sulfonic acid-grafted graphene as effective electrocatalysts for methanol oxidation in direct methanol fuel cells, Sci Rep. 6 (2016) Number: 21530.

[61] T. Gatti, N. Vicentini, M. Mba, E. Menna, Organic functionalized carbon nanostructures for functional polymer-based nanocomposites, Eur. J. Org. Chem. 6 (2016) 1071–1090.

[62] M. Toupin, D. Bélanger, Spontaneous functionalization of carbon black by reaction with 4-nitrophenyldiazonium cations, Langmuir 24 (2008) 1910–1917.

[63] D. Eder, R. Schlögl, (Eds.). Nanocarbon-inorganic hybrids: next generation composites for sustainable energy applications, Walter de Gruyter Gmbh & co, Berlin, 2014, 171−199.

[64] G. G. Wildgoose, C. E. Banks, R. G. Compton. Metal nanoparticles and related materials supported on carbon nanotubes: methods and applications, Small 2 (2006) 182–193.

[65] [49] S. H. Joo, S. J. Choi, I. Oh, J. Kwak, Z. Liu, O. Terasaki, R. Ryoo. Ordered nanoporous arrays of carbon supporting high dispersions of platinum nanoparticles, Nature 412 (2001) 169–172.

[66] A. Ciesielski, P. Samorì, Supramolecular approaches to graphene: from self-assembly to molecule-assisted liquid-phase exfoliation, Adv. Mater. 28 (2016) 6030–6051.

[67] A. A. Siller-Ceniceros, M. E. Sánchez-Castro, D. Morales-Acosta, J. R. Torres Lubian, E. Martínez G, F. J. Rodríguez Varela, Innovative functionalization of Vulcan XC-72 with Ru organometallic complex: Significant enhancement in catalytic activity of Pt/C

electrocatalyst for the methanol oxidation reaction (MOR), Appl. Catal., B. 209 (2017) 455-467.

[68] A. A. Siller-Ceniceros, M. E. Sánchez-Castro, F. J. Rodríguez Varela, Morales-Acosta, J. R. Torres-Lubian, E. Martínez-Guerra. Organometallic functionalization of graphene: Novel route to form Pt-Ru alloys as electrocatalyst for Methanol Oxidation Reaction, Memory of XVI International Congress of the Mexican Hydrogen Society, Querétaro, 2016, 172–176.

[69] D. Astruc, Organometallic chemistry and catalysis, Springer, Berlin, 2007.

[70] R. H. Crabtree (Ed.), The organometallic chemistry of the transition metals (Third edition). Jhon Wiley & Sons., Inc., New Jersey, 2001, 1-28.

[71] S. Chatterjee (Ed.), Encyclopedia of inorganic chemistry (Vol. 1), Discovery Publishing House Pvt. Ltd. New Delhi, (2012), 68-82.

[72] K. L. Haas, K. J. Franz, Application of metal coordination chemistry to explore and manipulate cell biology, Chem. Rev. 109 (2009) 4921–4960.

[73] R. Schrock, Multiple metal–carbon bonds for catalytic metathesis reactions (nobel lecture), Angew. Chem. Int. Ed. 45 (2006) 3748–3759.

[74] A. Yamamoto, Organotransition metal chemistry: fundamental concepts and applications, Jhon Wiley & Sons., Inc Publication, Hoboken, New Jersey, (1986).

[75] L. J. Brennan, Y. K. Gun'ko, Advances in the organometallic chemistry of carbon nanomaterials. Organometallics, 34 (2015) 2086-2097.

[76] E. L. Sceats, J. C. Green. Noncovalent interactions between organometallic metallocene complexes and single-walled carbon nanotubes, J. Chem. Phys. 125 (2006) 154704 1-12.

[77] E. D. Jemmis, M. Manoharan, P. K. Sharma, Exohedral η^5 and η^6 transition-metal organometallic complexes of C_{60} and C_{70}: a theoretical study, Organometallics 19, (2000) 1879-1887.

[78] J. Ran, M. W. Wong, Saturated hydrocarbon−benzene complexes: theoretical study of cooperative CH/π interactions. J. Phys. Chem. A 110 (2006) 9702-9709.

[79] F. A. Cotton, Proposed nomenclature for olefin-metal and other organometallic complexes, J. Am. Chem. Soc. 90, (1968), 6230-6232.

[80] A. M. Avdoshenko, I. N. Loffe, G. Cuniberti, L. Dunsch, A. A. Popov. Organometallic complexes of graphene: toward atomic spintronics using a graphene web. ACS Nano 5 (2011) 9939-9949.

[81] R. C. Haddon, S. Sarkar, S. Niyogi, E. Bekyarova, M. E. Itkis, X. Tian, F. Wang, Organometallic chemistry of extended periodic π-electron systems. U.S. Patent US20130202515, (2013).

[82] S. Sarkar, S. Niyogi, E. Bekyarova, R. C. Haddon, Organometallic chemistry of extended periodic π-electron systems: hexahapto-chromium complexes of graphene and single-walled carbon nanotubes. Chem. Sci. 2 (2011) 1326−1333.

[83] S. Sarkar, R. C. Haddon. Organometallic complexes of graphene and carbon nanotubes: introducing new perspectives in atomtronics, spintronics, high mobility graphene electronics and energy conversion catalysis. -arXiv preprint arXiv: 1409-5194, (2014).

[84] K.T. Iijima (Ed.), Carbon nanotubes and graphene (Second edition), Elsevier, Oxford (2014), 201–224.

[85] M. Antonietti, K. Müller (Ed.), Chemical synthesis and applications of graphene and carbon materials. Wiley-VCH, Wheinheim, (2017), 87–110.

[86] E. B. Bekyarova, S. Niyogi, S. Sarkar, X. Tian, M. Chen, M. L Moser, K. Ayub, R. H. Mitchell, R. C Haddon. Stereochemical effect of covalent chemistry on the electronic structure and properties of the carbon allotropes and graphene surfaces. Synthetic Met. 210 (2015) 80–84.

[87] S. Sarkar, M. L. Moser, X. Tian, X. Zhang, Y. F. Al−Hadeethi, R. C. Haddon, Metals on graphene and carbon nanotube surfaces: from mobile atoms to atomtronics to bulk metals to clusters and catalysts. Chem. Mater. 26 (2014) 184−195.

Chapter II

3. Hypothesis

The ruthenium organometallic compounds have aromatic groups in its structure, similar to benzoic rings present in the graphitic carbon structure, it could lead to affinity between both materials, possibly getting a significant amount of ruthenium sites on the carbon supports.

Furthermore, functionalized carbonaceous supports will be an attractive option to be employed in the synthesis of electrocatalysts type Pt/C and Pt/RGO. These electrocatalysts will be able to form Pt–Ru interactions, in order to be applied as anode to MOR in a half–cell reaction.

Chapter III

3. Objectives

3.1 General objective

Synthesize and characterize ruthenium organometallic compounds, to evaluate its performance for the functionalization of nanostructured carbon systems, and from these functionalized supports to develop electrocatalysts type Pt/C and Pt/RGO. Subsequently, apply the electrocatalysts to evaluate the MOR in acid media.

3.2 Specific objectives

* Synthesis and physicochemical characterization of organometallic compounds $[\eta^6–C_6H_5OCH_2CH_2OH)RuCl_2]_2$ (*Ru–dim*) and $[(\eta^6–C_6H_4(CHMe_2)Me)RuCl_2]_2$ (*Ru-cym*).

* Functionalization and physicochemical characterization of Vulcan XC-72 with home–made ruthenium organometallic compound *Ru–dim* and their comparison with functionalized support using commercial salt of ruthenium.

* Functionalization and physicochemical characterization of carbon nanostructured support, RGO with commercial and home–made ruthenium organometallic compounds *Ru–dim* and *Ru–cym* to be compared.

* Synthesis and physicochemical characterization of electrocatalyst type Pt/C and Pt/RGO, employing functionalized carbon supports to be applied as anode to evaluate their electrochemical activity to MOR in acid media.

Chapter IV

4. Experimental section

4.1 Chemical reagents and laboratory supplies

The following chemical reagents of analytical grade were used in this project. Vulcan XC-72 (99.95%) and reduced graphene oxide (Graphene, 75% exfoliation) were obtained from Cabot Corp. and ID-Nano, respectively. Ruthenium chloride ($RuCl_3 \cdot XH_2O$) (40-49% Ru), ethylene glycol ($C_2H_6O_2$) (99.8%), 1−metoxy−1,4−ciclohexadiene ($C_6H_7OCH_3$) (85%), 1−isopropyl−4-methylcyclohexa−1,3−diene (85%, α-terpinene), ethanol (C_2H_5OH) (99.9%), methanol (CH_3OH) (99.9%), isopropyl alcohol (C_3H_7OH) (99.97%), ethylic ether ($(C_2H_5)_2O$) (99.9%), chloroform ($CHCl_3$) (99.9%), benzophenone ($C_{13}H_{10}O$) (99%), phosphorus pentoxide (P_2O_5) (97%), iodine (I_2) (99.8%), magnesium (Mg) (99.98%), sodium sulphate (Na_2SO_4) (≥ 99%), tetrahydrofuran (THF, C_4H_8O) (99%), methylene chloride (CH_2Cl_2) (99.8%), deuterated water (D_2O) (99.99%), dimethyl sulfoxide (DMSO, C_2H_6OS) (99.96%), Chloroform-d (CCl_3D) (99.8%), chloroplatinic acid hexahydrate ($H_2PtCl_6 \cdot XH_2O$) (≥ 37.50% Pt), Nafion solution 117 (5 wt. %), sulfuric acid (H_2SO_4) (95-99%), nitric acid (HNO_3) (70%) and sodium hydroxide (NaOH) (97%), were purchased from Sigma Aldrich. Sodium metallic (Na^0), deionized and distilled water were acquired from Jalmeck. pH calibration standards (4.00±0.01, 7.00±0.01 and 10.00±0.01) were obtained from Thermo Fisher Scientific. Liquid nitrogen $N_{2(l)}$, ultra−high purity 99.9% of gases as Argon $Ar_{(g)}$, carbon monoxide $CO_{(g)}$ and Nitrogen $N_{2(g)}$ were purchased from INFRA.

The Schelnk line (crystal instrumentation) was used for the synthesis of organometallic compounds. The following laboratory supplies were employed during the experimentation: Distillation system (crystal instrumentation), reflux system(crystal instrumentation), thermo–circulator (Volta–Lab), high–vacuum pump (Hanning Elektro–Werke), vacuum pump (Gast Manufacturing Inc.), ultrasonic bath (Branson), mechanical convection oven (Lab–line), digital balance (Ohaus), electric dryer (Sanpla), stainless steel hood (TecnoLab), hypodermic syringes (Cadence Science), Double–tipped cannula (Sigma–Aldrich), filter cannula (Sigma–Aldrich), Dewar flask (Thermo–Scientific), pH meter (Conductronic), digital stirring hot plate (Thermo–Scientific), rheostat (Stuco Energy Products CO.), filter paper (Whatman), filter membrane (Durapore), Micropipette (Nichipet), beral pipette (Simport), hermetic plastic tube (Eppendorf) and suba seal (Sigma–Aldrich).

4.2 Synthesis of Ru organometallic compounds

A Schlenk line with inert atmosphere was used to obtain the Ru compounds. The glassware was previously washed and heated at 95 ºC overnight to eliminate moisture. Dried solvents were used during the synthesis of organometallic complexes to avoid the formation of

metallic oxides. Each solvent was subjected to a specific drying agent to increase the drying efficiency (See Table 4.1) [1].

Table 4.1 Drying agents implemented to eliminate humidity of polar solvents [1].

Solvent	Drying agent	Reflux (time)
Ethanol	Mg^0/I_2	3 h
Ethylic ether, Tetrahydrofuran	$Na^0/ C_{13}H_{10}O$	2 h
Mytilene chloride	P_2O_5	2 h
Chloroform	Na_2SO_4 (48h at RT.)	–

4.2.1 Synthesis of Ru–dim

The organometallic compound $[(\eta^6–C_6H_5OCH_2CH_2OH)\ RuCl_2]_2$ (*Ru–dim*) was based following the methodology reported in [2], with slight modifications as follows: methoxy-1,4-cyclohexadiene (2.25 mL, 19.2 mmol) was added to an ethylene glycol solution (15 mL) of ruthenium trichloride trihydrate (1.0 g, 3.82 mmol), followed by heating at 120 °C for 3 h. The solution was washed with 5 mL of ethylic ether and ethanol for three times to posterior dried solution in vacuum to obtain solid material. *Ru–dim* was obtained as orange/brown powder in 59.3 % (702 mg, 1.13 mmol) and (m.p. 150 °C). ^{1}H-NMR (500 MHz, D_2O, δ ppm): 3.94 (t, 4 H, CH_2, J = 7.1 Hz), 4.32 (t, 4 H, CH_2), 5.52 (m, 2 H, *Ph*), 5.54 (m, 4 H, *Ph*), 6.07 (t, 4 H, A *Ph*, J = 9.2 Hz).

4.2.2 Synthesis of Ru–cym

The $[(\eta^6\text{-}C_6H_4(CHMe_2)Me)RuCl_2]_2$ (*Ru–cym*) compound was synthetized following an established methodology in [3], with modifications: $RuCl_3{\cdot}H_2O$ (2 g, 9.6 mmol) and 1-isopropyl-4-methylcyclohexa–1,3–diene (10 mL) in dry ethanol (90 mL) were refluxed for 4 h. A red-brown powder was obtained and washed with diethyl ether to remove any excess of α–terpinene. Afterwards, in order to purify the Ru–cym compound, 5 ml of dry chloroform were added to the solution which was frozen by submerging it in liquid nitrogen (–195 ºC) for 5 min. Then, vacuum was carried out for three times. Compound *Ru–cym* was obtained as orange/reddish powder in 71.5 % (2.1112 g, 3.44 mmol) and (m.p. 247 °C). ^{1}H-NMR (500 MHz, CCl_3D_2, δ ppm): 1.25 (d, 6 H, CH (CH_3)$_2$, J = 7.2 Hz), 2.13 (s, 3H, C_6H_4 CH_3), 2.89 (m, 1 H, CH (CH_3)$_2$), 5.32 (d, 2 H, η^6–C_6H_4 J = 6.0 Hz), 5.45 (d, 2 H, η^6–C_6H_4, J = 6.0 Hz).

4.3 Functionalization of carbon supports with ruthenium compounds

4.3.1 Synthesis of functionalized Vulcan supports: $C_{Ru\text{-}dim}$ and $C_{Ru\text{-}com}$

$C_{Ru\text{-}dim}$ was obtained from the functionalization of Vulcan XC–72 with the organometallic compound, starting from a *Ru–dim*: Vulcan molar ratio of 1:10 [4], as follows: 104.16 mg (0.168 mmol) of *Ru–dim* and 20 mg (1.68 mmol) of Vulcan were stirred in 8 mL of THF under $Ar_{(g)}$ atmosphere and refluxing conditions for 24 h at 130 °C. The black solution generated was transferred into a Schlenk tube, filtered through a cannula, washed with dried THF and finally dried in vacuum for 12 h, resulting in a black/reddish powder.

$C_{Ru\text{-}com}$ was obtained following the same procedure described above, starting from 43.93 mg (0.168 mmol) of commercial $RuCl_3 \cdot XH_2O$ and 20 mg of Vulcan, resulting in a black powder. Figure 4.1 shows a scheme of the procedure. Additionally, non–functionalized Vulcan (C) was used without further treatment as support.

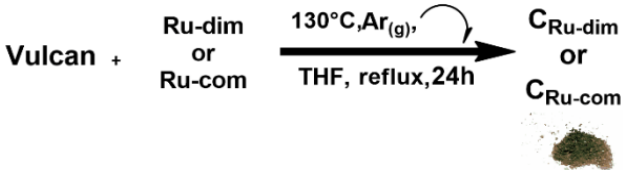

Figure 4.1 Reactions of the experimental procedure for Vulcan functionalization, (black/reddish powder) [4].

4.3.2 Synthesis of functionalized reduced graphene oxide supports: $RGO_{Ru\text{-}dim}$, $RGO_{Ru\text{-}cym}$ and $RGO_{Ru\text{-}com}$

Functionalization of reduced graphene oxide (RGO) to obtain *$RGO_{Ru\text{-}dim}$, $RGO_{Ru\text{-}cym}$ and $RGO_{Ru\text{-}com}$* was performed under the same conditions and molar stoichiometry between Ru precursors and carbon as described for Vulcan. In addition, graphene was also functionalized with the Ru–cym compound to obtain *$RGO_{Ru\text{-}cym}$* starting with 102.88 g (0.168 mmol) of Ru precursor and 20 mg of RGO. The only difference relative to the other supports was that the refluxing temperature was set to 72 ºC [4, 5]. In the case of C and non–functionalized RGO were also tested as support. Figure 4.2 shows a scheme of the experimental procedure.

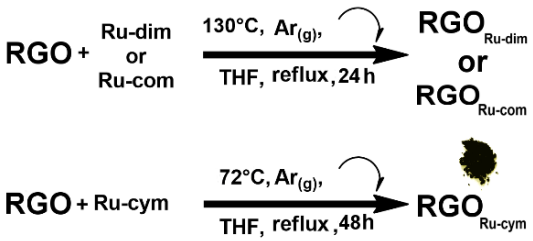

Figure 4.2 Reactions of the experimental procedure for reduced graphene oxide $RGO_{Ru\text{-}dim}$, $RGO_{Ru\text{-}com}$ and $RGO_{Ru\text{-}cym}$, (black powder) [4, 5].

4.4 Synthesis of electrocatalysts anodes based on Platinum

4.4.1 Synthesis of Pt/C and Pt/RGO electrocatalysts

The 20 wt. % *Pt/C, Pt/*$C_{Ru\text{-}dim}$*, Pt/*$C_{Ru\text{-}com}$*, Pt/RGO, Pt/*$RGO_{Ru\text{-}dim}$*, Pt/*$RGO_{Ru\text{-}cym}$ and *Pt/*$RGO_{Ru\text{-}com}$ electrocatalysts were synthesized via the polyol method with ethylene glycol (EG) as reducing agent, in Figure 4.3 is represented the chemical equation and conditions of synthesis [6, 7]. Separately, 80 mg of the corresponding carbon support was dispersed for 30 min. by ultrasound in 48 mL of EG. The appropriate amount of $H_2PtCl_6{\cdot}6H_2O$ (53.3 mg) was dispersed in an ultrasonic bath for 30 min in 2 mL of EG and added to the carbon solution. The mixture was subjected to magnetic stirring for 1 h, followed by the adjustment of the pH to 12 by adding NaOH (1 mol L^{-1}).

Afterwards, the temperature was increased to 130 ºC under refluxing and stirring conditions, maintaining a constant temperature for 3 h and left to cool down to room temperature. Subsequently, 4 mL of H_2SO_4 (1 mol L^{-1}) was used to adjust the pH=2, maintaining stirring for another 3 h. The solution was filtered, and the dark powder obtained was washed and dried under vacuum atmosphere. Figure 4.3 shows the synthesis conditions to obtain the Pt–based electrocatalysts.

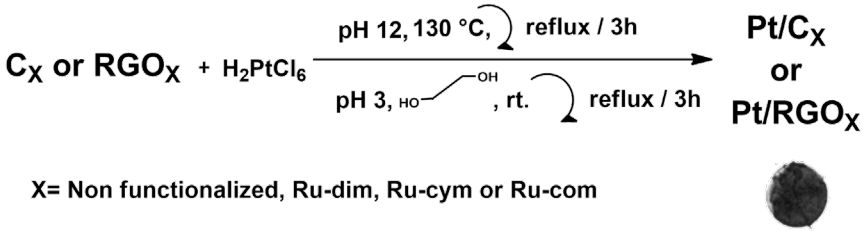

Figure 4.3 Reactions of the experimental conditions to synthesize the *Pt/C, Pt/*$C_{Ru\text{-}dim}$*, Pt/*$C_{Ru\text{-}com}$*, Pt/G, Pt/*$RGO_{Ru\text{-}dim}$*, Pt/*$RGO_{Ru\text{-}cym}$ and *Pt/*$RGO_{Ru\text{-}com}$ electrocatalysts, (black powder) [6, 7].

4.5 Physicochemical characterization

4.5.1 Nuclear Magnetic Resonance (NMR)

Dimers of organometallic complexes Ru–dim and Ru–cym were characterized by ^{1}H–NMR spectroscopy. Chemical analyses were obtained in a 500 MHz Bruker Advance III (using a 5 mm direct broad band with Z–grad (PABBO-1H/D Z–GRAD). The ^{1}H chemical shifts were referenced to residual no deuterated solvent. Ru-dim was dissolved in Deuterated water (D_2O) (99.99%) and Ru-cym was dissolved in dimethyl sulfoxide (DMSO) (99.96%).

4.5.2 Fourier Transform infrared spectroscopy (FT–IR)

FT–IR spectra were acquired using a Thermo-Nicolet 6700 spectrometer in the 4000 to 600 cm^{-1} region, with a nominal resolution of 4 cm^{-1} using the ATR technique. The chemical functional groups of experimental spectra were evaluated with the OMNIC software.

4.5.3 Raman Spectroscopy (Raman)

Raman micro-analysis was performed in confocal μ-Surf explorer microscope (Horiba) using laser pulse energy of 2.33 eV (532 nm). All microanalysis images were taken at 10x magnification. The acquisition time for non–functionalized C and RGO were 30 s with a 50% filter. In the case of functionalized supports, the parameters were 10 s and 25%, respectively. Spectra were recorded over the 4000–400 cm^{-1} range. The relationship between the intensities of the G and D bands (I_D/I_G ratio) was used to determine the rehybridization after functionalization of carbon supports. It is important to note that the G–band represents the degree of graphitization (C–sp^2 hybridization), while the D–band is due to the lattice disorder or defects (sp^3 hybridization). The spectra in Figure 4.4 a) show the thypical bands assigned to multilayer carbon nanostructured material at three different laser energies [8].

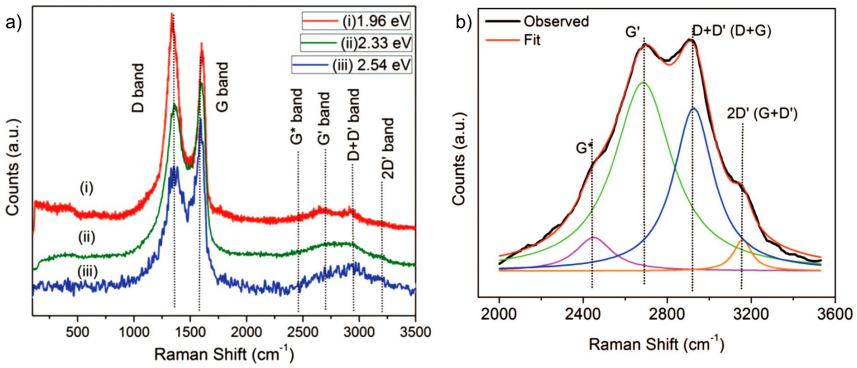

Figure 4.4 a) Raman spectra of exfoliated RGO using three differents laser energies. b) Multiple peak for 2D region of multilayer graphene [8].

Furthermore, the deconvolution in Figure 4.4 b) of 2D band also known as G´ band is another important parameter to known if the carbon lattice is a monolayer, bilayer or multilayer.

4.5.4 X-Ray Diffraction (XRD)

XRD patterns were recorded in an Empyrean PANalytical diffractometer with a Bragg–Brentano geometry operated at 40 kV and 45 mA, using a Cu-K_α radiation source (λ=1.5406 Å) in the 2θº range of 5–100° with a step scan of 0.0167 (2θº) and 59 s per step. The patterns collected were plotted with Match! ™ Sofware. The crystal structures of face-centered cubic (fcc) platinum and hexagonal close-packed (hcp) ruthenium, where identified with the JCPDS–04–0802 and JCPDS–06–0663 cards, respectively. Figure 4.5 illustrates the structure of both metals.

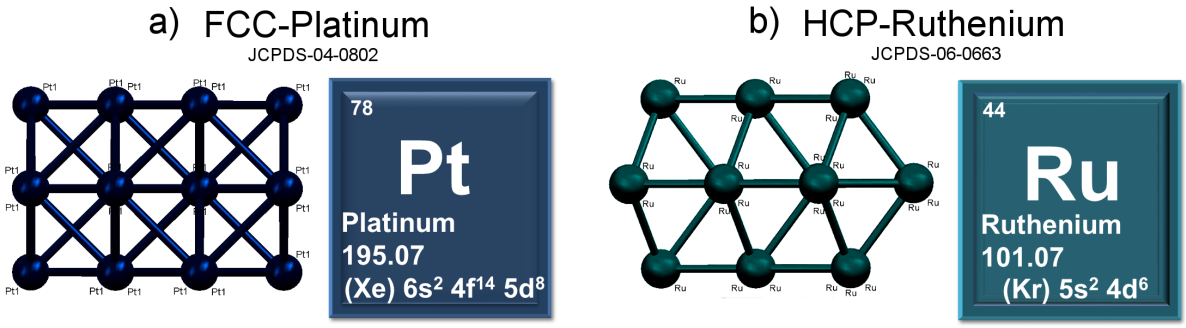

Figure 4.5 Crystal structures of a) fcc–Pt and b) hcp–Ru, developed with Mercury software (Cambridge Crystallographic Data Centre).

International Centre for Diffraction Data (ICDD) established the crystal structures of face-centered cubic (fcc) to platinum and hexagonal close-packed (hcp) of ruthenium, described by cards JCPDS–04–0802 and JCPDS–06–0663 illustrated in Figure 4.5 a) and b), respectively.

The crystallite size (d) of electrocatalysts was determined from the diffraction patterns by using Scherrer's equation [9]:

Equation 4.1: $$d=\frac{0.9\times\lambda_{\alpha 1}}{\beta_{2\theta}\times \cos\theta_{max}}$$

where $\lambda_{\alpha 1}$ is the X–ray wavelength source (CuK_{α}=1.54056 Å). The parameter $\beta_{2\theta}$ is the full width at half maximum (FWHM) in radians and θ_{max} corresponds to angle position of the peak in 2θº scale.

The lattice parameter (a_{fcc}) of Pt was calculated with the following equation [10]:

Equation 4.2: $$a_{fcc}=\frac{\sqrt{2}\,\lambda_{\alpha_1}}{\sin\theta_{max}}$$

where $\lambda_{\alpha 1}$ and θ_{max} have the same meaning as calculation described in Equation 4.1. From the Vegard's law [11] the atomic fraction of Ru alloyed (X_{Ru}) was calculated [12]:

Equation 4.3: $$a_{fcc}= l_{oc}- k\, X_{Ru}$$

where l_{oc} = 3.9155 Å is the lattice parameter for pure platinum supported on carbon and k =0.124 Å is a constant.

4.5.5 Scanning Electron Microscopy coupled with Energy Dispersive Spectroscopy (SEM-EDS)

The morphology of organometallic compounds and the carbon supports was determined in a Philips XL30 SEM apparatus, under an accelerating voltage of 20 kV. The chemical composition of the carbon supports and the Pt electrocatalysts was determined with the same apparatus equipped with the Energy Dispersive Spectroscopy (EDS) technique. Five quantitative microanalyses in different areas of the samples were taken and averaged.

4.5.6 High–Resolution Transmission Electron Microscopy (HR–TEM)

The electrocatalysts were characterized by HR–TEM, with high–angle annular dark field scanning/transmission electron microscopy (HAADF–STEM) and chemical mapping in a Jeol JEM–ARM200F microscope, operating at 30 kV. Images, selected area electron diffraction (SAED) pattern and histograms of nanoparticles were treated with Gatan Digital Micrograph software.

4.5.7 X-Ray Photoelectron Spectroscopy (XPS)

The chemical surface composition was studied by X–Ray Photoelectron Spectroscopy (XPS) in a Thermo Scientific Escalab 250 Xi instrument having an Al–K_{α} (1486.68 eV) source and operating at ~10 mbar. The X–ray voltage and power were 14 kV and 350 W, respectively.

The spectra were obtained using a pass energy of 20 eV. Peak fitting with Voight profiles was performed using the AAnalyzer™ software [13]. The baseline corrections were made using the Shirley-Sherwood method. Binding energies were calibrated to the C (1s) peak fixed at 284.8 eV.

XPS analysis has a sensibility to determinate the chemical composition of sample surface and depth nearby 10 nm. For deeper regions, angle resolved XPS analysis is necessary [14]. In this work, the elemental composition (% at.) of the electrocatalysts was calculated with the following equation [15–16]:

Equation 4.4: $$\% \text{ at.} = \frac{\frac{A_i}{S_i}}{\sum_j^m \frac{A_j}{S_j}}$$

where A_i is area under photoelectron peak of element *i;* S_i is the ratio between the intensity of the photoelectron peak of element *i* and the number of atoms per cm^3 [18]; and *j* and *m* represent the number of elements in the sample.

4.6 Electrochemical Characterization

Electrochemical measurements were carried out in a three-electrode electrochemical cell using a VoltaLab PGZ301 potentiostat/galvanostat. Figure 4.6 a) shows an image of the cell set-up.

The counter-electrode was a Pt foil, while the reference electrode was of the Ag/AgCl type, although the potentials have been referred to the Standard Hydrogen Electrode (SHE). To build the thin–film working electrodes, a mirror-finished glassy carbon disk (5 mm diameter) was used. Catalytic inks were prepared by separately sonicating 10 mg of Pt/$C_{Ru\text{-}dim}$, Pt/$C_{Ru\text{-}com}$, Pt/C, Pt/$RGO_{Ru\text{-}dim}$, Pt/$RGO_{Ru\text{-}cym}$, Pt/$RGO_{Ru\text{-}com}$ or Pt/RGO for 30 min, in a mixture containing 2 mL isopropyl alcohol and 5 µL Nafion solution. Then, aliquots of 10 µL of each electrocatalyst were deposited over the glassy carbon as shown in Figure 4.6 b) and let to dry.

Cyclic voltammograms (CVs, in mA cm^{-2} or mA $mg^{-1}{}_{Pt}$) were acquired in N_2-saturated 0.5 mol L^{-1} H_2SO_4, in the 0.05 to 1.2 V (vs. SHE) potential range, at a scan rate of 20 mV s^{-1}. The electrochemically active surface area (ECSA, in m^2 $mgPt^{-1}$) of each electrocatalyst was calculated from the H_{des} region of the CVs with equation [17]:

Equation 4.5: $$\text{ECSA} = \frac{Q}{Q_{H_{des}} x\, L_{Pt}}$$

where Q is the integrated current under the area of H_{des} (µC cm^{-2}) region illustrated in Figure 4.7 a) to characteristic behavior of Pt/C catalyst, Q_{Hdes} is the adsorption charge for an atomic

layer of hydrogen on catalyst surface, Q_{Hdes}=210 µC cm^{-2} for smooth platinum surface. L_{Pt} is the amount of Platinum on geometric area of electrodes (µg).

In order to evaluate the catalytic activity for the MOR, the polarization curves were acquired in the same conditions, adding 0.5 mol L^{-1} CH_3OH to the electrolyte. CO–stripping measurements were carried out bubbling CO into the cell for 10 min while polarizing the electrode at 0.075 V (vs. SHE), followed by Ar purging for 20 min. Then, CVs were recorded at 20 mV s^{-1} in the range of 0.05 to 1.2 V (vs. SHE) detecting CO desorption (CO_{des}) pick. Figure 4.7 a) illustrates the hydrogen adsorption–desorption, double layer and platinum oxides regions. Additionally, the CV after CO-stripping test of Pt/C catalyst is represented in Figure 4.7 b), showing the CO_{des} region.

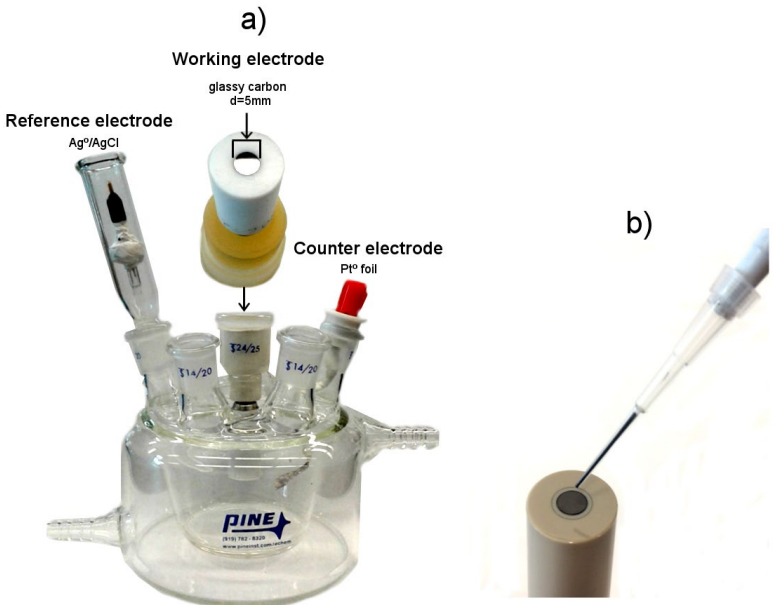

Figure 4.6 a) Image of the electrochemical cell showing the three electrodes. b) Image of the deposition of catalytic ink over the glassy carbon disk.

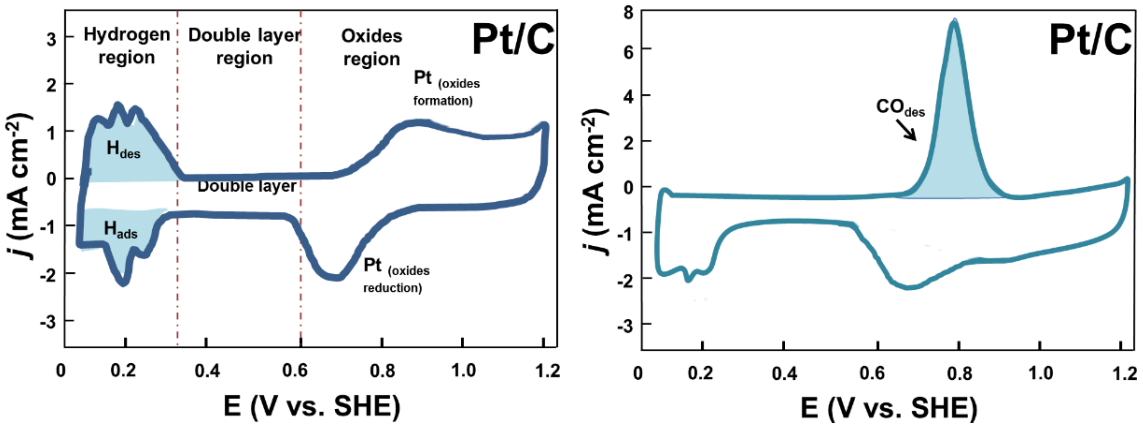

Figure 4.7 CVs of the electrochemical characterization of Pt/C electrocatalysts. a) Under N_2 atmosphere showing the H_{ads}/H_{des} regions, double layer region and typical regions of oxidation-reduction reactions. b) CO desorption region (CO_{des}), obtained after CO-stripping test.

References

Chapter IV

[1] W.L.F. Armarego and Ch. L.L. Chai, Purification of laboratory chemicals (fifth edition). Elsevier science, New york, 2003.

[2] J. Soleimannejad, C. White, A Convenient one–pot synthesis of a functionalized–arene ruthenium half-sandwich compound $[RuCl_2(\eta^6–C_6H_5OCH_2CH_2OH)]_2$, Organometallics, 24 (2005) 2538–2541.

[3] S. B. Jensen, S. J. Rodger and M. D. Spicer. Facile preparation of η^6–*p*–cymene ruthenium diphosphine complexes. Crystal structure of $[(\eta^6–p–cymene)Ru(dppf)Cl]PF_6$, Journal of J. Organomet. Chem, 556 (1998) 151–158.

[4] R. C. Haddon, S. Sarkar, S. Niyogi, E. Bekyarova, M. E. Itkis, X. Tian and F. Wang, US. Pat., 0202515, 2013.

[5] S. Sarkar, H. Zhang, J-W. Huang, F. Wang , E. Bekyarova , Ch. N. Lau and R.C. Haddon. Organometallic hexahapto functionalization of single layer graphene as a route to high mobility graphene, Adv. Mater., Adv. Mater., 25 (2012) 1131–1136.

[6] D. González–Quijano, W. J. Pech–Rodríguez, J. I. Escalante–García, G. Vargas–Gutiérrez and F. J. Rodríguez-Varela. Electrocatalysts for ethanol and ethylene glicol oxidation reactions. Part I: Effects of the polyol synthesis conditions on the characteristics and catalytic activity of Pt-Sn/C anodes, Int. J. Hydrogen Energy, 39 (2014) 16676–16685.

[7] D. González–Quijano, W. J. Pech–Rodríguez, J. A. González–Quijano, J. I. Escalante–García, G. Vargas–Gutiérrez, I. Alonso-Lemus and F. J. Rodríguez-Varela. Electrocatalysts for ethanol and ethylene glicol oxidation reactions. Part II: Effects of the polyol synthesis conditions on the characteristics and catalytic activity of Pt-Ru/C anodes, Int. J. Hydrogen Energy, 40 (2015) 17291–17299.

[8] A. Kaniyoor, S. Ramaprabhu. A Raman spectroscopic investigation of graphite oxide derived graphene, AIP Adv. 2 (2012) 032183 1–13.

[9] G. Liu, H. Zhang and J. Hu. Novel synthesis of a highly active carbon-supported $Ru_{85}Se_{15}$ chalcogenide catalyst for the oxygen reduction reaction, Electrochem. Commun. 9 (2007) 2643-2648.

[10] V. Radmilovic, H. A. Gasteiger and P. N. Ross. Structure and chemical composition of a supported Pt-Ru electrocatalyst for methanol oxidation, J. Catal. 154 (1995) 98–106.

[11] G. S. Chai, S. B. Yoon, J-S. Yu, J-H. Choi and Y-E. Sung. Ordered Porous Carbons with Tunable Pore Sizes as Catalyst Supports in Direct Methanol Fuel Cell, J. Phys. Chem. B 108 (2004) 7074-7079.

[12] J.W. Guo, T. S. Zhao, J. Prabhuram, R. Chen and C. W. Wong. Preparation and characterization of a PtRu/C nanocatalyst for direct methanol fuel cells, Electrochim. Acta 51 (2005) 754–763.

[13] http://www.qro.cinvestav.mx/~aanalyzer/arxpsAnalysisSharpIntefaces.pdf.

[14] L. Calvo-Barrio and G. Vargas. Photoelectron spectroscopy for surface analysis: x-ray and uv excitation. (2012) Universitat de Barcelona Spain.

[15] S. H. Kim, S-Y Kwak, B-H. Sohn, T. H. Park. Design of TiO_2 nanoparticle self-assembled aromatic polyamide thin-film-composite (TFC) membrane as an approach to solve biofouling problem. J. Membrane Sci. 211 (2003) 157–165.

[16] J. Chaistain, J. F. Moulder, W. F. Stickle, P. E. Sobol and K. D. Bomben. Handbook of x-ray photoelectron spectroscopy. (1992) Perkin-Elmer Corporation California USA.

[17] W. J. Pech–Rodríguez, D. González–Quijano, G. Vargas–Gutiérrez, C. Morais, T.W. Napporn and F. J. Rodríguez–Varela. Electrochemical and in situ FTIR study of the ethanol oxidation reaction on PtMo/C nanomaterials in alkaline media. Appl. Catal B 203 (2017) 654–662.

Chapter V

5. Physicochemical characterization of Ru organometallic compounds

Arene Ruthenium (II) complexes have been subject of intense research in recent years due to their potential applications in several areas. Binuclear chloro−bridged compounds of the type [[η^6− (arene)$RuCl_2$] are useful precursors for the formation of a wide range of neutral or cationic half−sandwich Ru organometallic compounds. The most used method to synthesize this class of compounds it is through the dehydrogenation 1,3 or 1,4−cyclohexadienes using ethanolic $RuCl_3 \cdot XH_2O$ [1−3].

In this work the binuclear compounds were synthetized, the [(η^6-$C_6H_5OCH_2CH_2OH$)$RuCl_2$]$_2$ (*Ru−dim*) and [(η^6-$C_6H_4(CHMe_2)Me$)$RuCl_2$]$_2$ (*Ru−cym*), where the first one has a functionalized arene with polar group while the second has a p−cymene ligand. *Ru−dim* was obtained as orange/brown powder (59.26% yield). following the methodology reported in [4], with slight modifications displayed in Figure 5.1

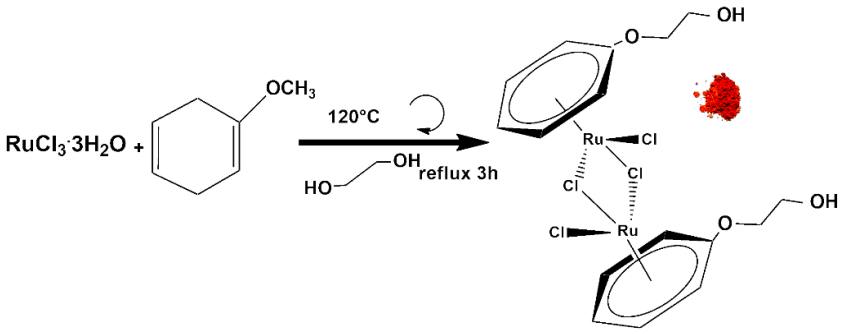

Figure 5.1 Parameters of the reaction for synthesis of *Ru−dim*, (orange/brown powder).

The *Ru−cym* compound was obtained following the methodology reported in [5], with modifications from ethanolic solution of $RuCl_3 \cdot XH_2O$ and 1−isopropyl−4-methylcyclohexa−1,3−diene (see Figure 5.2). *Ru−cym* was obtained as orange/reddish powder (71.52 % yield).

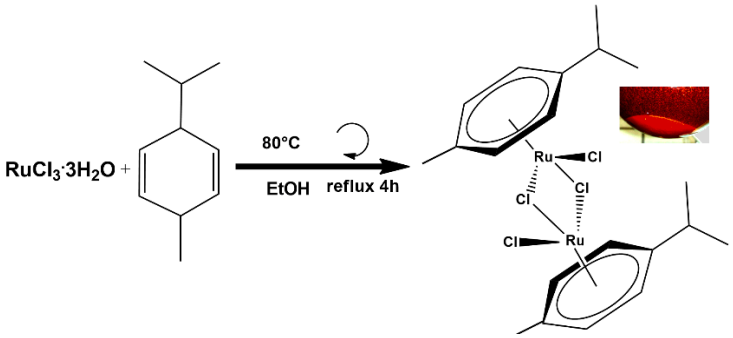

Figure 5.2 Parameters of the reaction for synthesis of *Ru−cym*, (orange/reddish powder in solution).

The physicochemical characterization of (*Ru−dim*) and (*Ru−cym)* was carried out by ^{1}H−NMR, IR spectroscopy and SEM-EDS techniques.

3.1 NMR

The ^{1}H−NMR spectrum in Figure 5.3 of *Ru−dim* compound demonstrated evidence of the functionalization of the arene ligand through the chemical shifts for the proton **a** and **b**, which appeared at *δ* 3.94 and 4.32 ppm, as well as the corresponding aromatic protons *orto* ***o***, *meta* ***m*** and *para* ***p*** at 5.52, 5.54 and 6.07 ppm, respectively. The central π bonded also known as hapto-coordination of aromatic ring with ruthenium atom are reported in 5.2−6.5 ppm [6].

Figure 5.4 illustrates the ^{1}H-NMR spectrum of *Ru−cym* compound. The signals showed at 1.25, 2.13 and 2.80 ppm, assigned to methyl and isopropyl groups of the arene ligand coordinated to ruthenium atom. Protons corresponding to *orto* ***o*** and *meta* ***m*** were observed as double signal at 5.32 and 5.45 ppm, respectively [5].

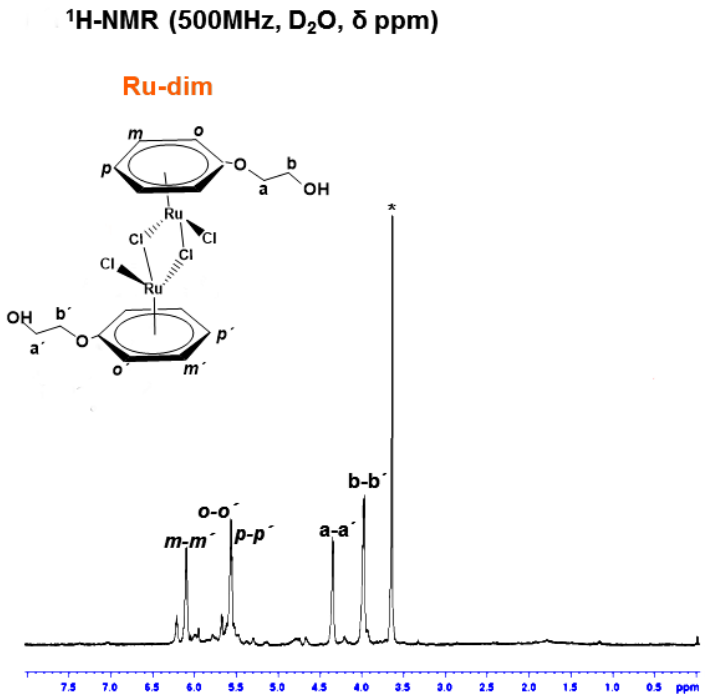

Figure 5.3 ^{1}H-NMR (500MHz, D_2O) spectrum of $[(\eta^6\text{-}C_6H_5OCH_2CH_2OH)RuCl_2]_2$ (*Ru−dim*).

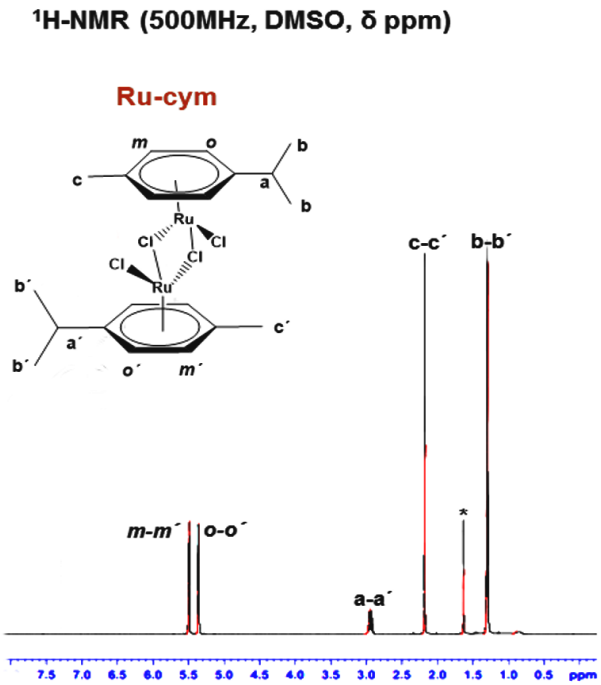

Figure 5.4 ^{1}H-NMR (500MHz, DMSO) spectrum of $[(\eta^6\text{-}C_6H_4(CHMe_2)Me)RuCl_2]_2$ (*Ru−cym*).

5. 2 FT–IR

Figure 5.5 displays the FT−IR spectra of Ru organometallic complexes. *Ru−dim* shows the absorption signals of C=C and C−H bonds in the1523-640 cm^{-1} and 3073-2900 cm^{-1} intervals, respectively attributed to vibrations of arene ring [3, 6]. The functional group as oxy−hydroxyl ethylene (−O−CH_2−CH_2−OH) in the arene structure shows the absorption bands corresponding to −OH, C−O−H and C−O groups at 3417, 1264 and 1091 cm^{-1}, respectively [7,8]. On the other hand, *ν*(Ru−Cl) can be found in the far−IR region since it has an absorption band at 303 cm^{-1} [9]. Moreover, the *Ru−dim* spectrum shows three high−intensity bands assigned to C=C bonds in 1523, 1444 and 640 cm^{-1} corresponding to vibrations in the arene ring.

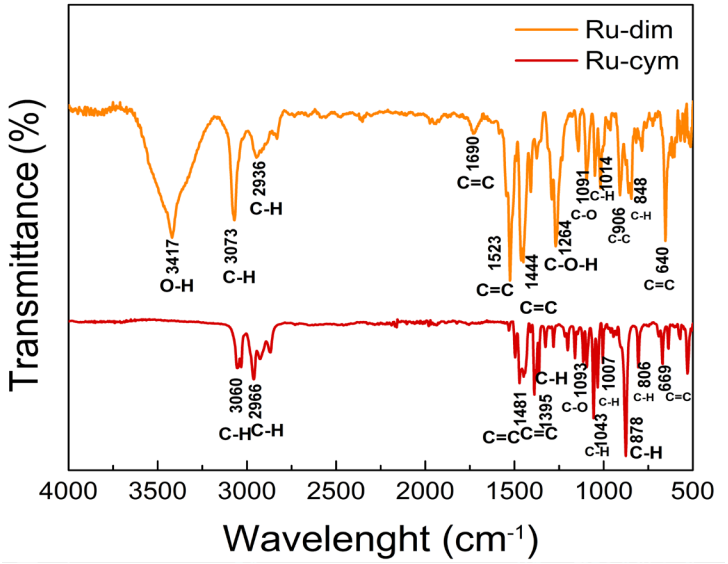

Figure 5.5 FT−IR spectra of organometallic compounds *Ru−dim* and *Ru−cym*.

Meanwhile, the FT−IR spectrum of *Ru−cym* displays absorption bands due to C=C and C−H bonds of the p−cymene aromatic ligand, with comparable wavelength positions as those aromatic rings of arene ligand in *Ru−dim*. However, in the case of the p−cymene ligand, the aromatic ring has methyl and isopropyl chemical fragments, whose signals overlap with those of weak absorption frequencies from the arene ring and the bands assigned to C−H bonds from alkyl fragments (vibrations in 1000−1300 cm^{-1}) [10].

3.3 SEM–EDS

Figure 5.6 shows the SEM images of a) *Ru−dim* and b) *Ru−cym*. Both materials have large irregularly−shaped crystals. The Ru−cym seems to be prism−shaped, similar to previously reported to Ru−dim compound [11].

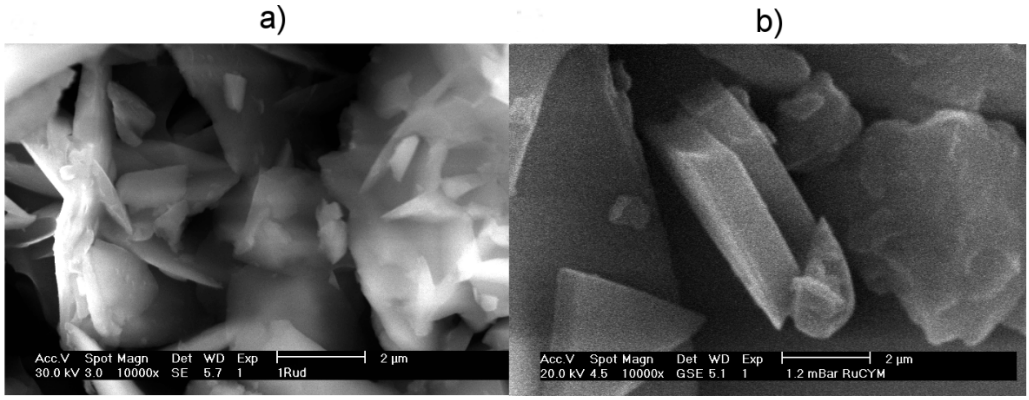

Figure 5.6 SEM micrographs of: a) *Ru−dim* and b) *Ru−cym*.

Table 5.1 Chemical composition of *Ru−dim* and *Ru−cym*.

Organometallic complex	**C**	**Ru**	**O**	**Cl**
		(% wt.)		
Ru-dim	42.00	27.82	7.29	22.89
Ru-cym	51.42	27.03	-	21.55

The chemical composition of *Ru−dim* and *Ru−cym* is displayed in Table 5.1. It is interesting to note that the Ru concentrations is ~27 wt. % in both cases. The carbon concentrations in *Ru−cym* is 51.42 wt. % higher than that of *Ru−dim* (42 wt. %). This outcome is expected since the p−cymene ligand in *Ru−cym* contains methyl and isopropyl chemical fragments contributing to the presence of C. Meanwhile, only *Ru−dim* has the presence of oxygen (7.29 %), attributed to (−O−CH_2−CH_2−OH) groups linked to its arene ring. Chloride concentration is 22.89 and 21.55 wt. % for *Ru−dim* and *Ru−cym*, respectively. Overall, it can be concluded that the chemical composition of the Ru compounds is similar and can be a consequence of the similitude in their structures.

Conclusions

Chapter V

The ruthenium organometallic compounds were synthesized under inert conditions employing Schlenk technique, obtaining finally stable compounds in air conditions.

- The ^{1}H–RMN results confirm the formation of coordinate interaction arene–ruthenium of organometallic compounds $[(\eta^6\text{–}C_6H_5OCH_2CH_2OH)RuCl_2]_2$ (*Ru–dim*) and $[(\eta^6\text{–}C_6H_4(CHMe_2)Me)RuCl_2]_2$ (*Ru–cym*).

- FT–IR analysis determinate the presence of C=C bond from arene ligand and the signals attributed to functional groups bonded to aromatic rings functional group oxy hydroxyl ethylene (−O−CH_2−CH_2−OH) in the arene structure of *Ru–dim* and (isopropyl, $CHMe_2$), (methyl, Me) from *Ru–cym*.

- SEM−EDS Analysis determinate the irregular polygonal structure to organometallic compounds and the ruthenium ~27 wt. % in both cases, an important parameter of high concentration of Ru available.

- Thermal stability at temperature > 130ºC of *Ru–dim* (m p. 150ºC) and *Ru–cym* (m. p. 247º C) and dimeric structure conferring stability (36 electrons), characteristics that contributes to avoid degradation of organometallic compounds during functionalization process and posterior polyol synthesis.

- The arene and p-cymene ligands from *Ru–dim* and *Ru–cym*, respectively, possess high similitude to aromatic rings that conforms graphitic carbon structures, converting them in excellent materials for the functionalization of graphitic carbon supports such as Vulcan and RGO.

References

Chapter V

[1] P. Pertici, P. Salvadori, A. Biasci, G. Vitulli, M. A. Bennett, L. A. P. Kane-Maguire, Synthesis of the Arene Complex [{RuCl2(η^6–o–$MeC_6H_4CO_2Me$)}$_2$] and Separation of its Diastereomeric (–)(S) –1–Phenylethylamine Adducts, J. Chem. Soc., Dalton Trans. 7 (1988), 315−320.

[2] M. A. Bennett, A. K. J. Smith, Arene Ruthenium(II) Complexes formed by Dehydrogenation of Cyclohexadienes with Ruthenium (III) Trichloride, Chem. Soc., Dalton Trans. 3 (1974), 233−241.

[3] R. A. Zelonka, M. C. Baird, Benzene Complexes of Ruthenium (II), Can. J. Chem. 50 (1972) 3063–3072.

[4] J. Soleimannejad, C. White, A Convenient One-Pot Synthesis of a Functionalized-Arene Ruthenium Half-Sandwich Compound [$RuCl_2(\eta^6$-$C_6H_5OCH_2CH_2OH)]_2$, Organometallics. 24 (2005) 2538−2541.

[5] S. B. Jensen, S. J. Rodger and M. D. Spicer, Facile preparation of η^6-*p*-cymene ruthenium diphosphine complexes. Crystal structure of [(η^6-*p*-cymene)Ru(dppf)Cl]PF_6, J. Organomet. Chem. 556 (1998) 151–158.

[6] K. Nakamoto Ed. Infrared Spectra of Inorganic and Coordination Compounds, 4th ed. John Wiley & Sons Inc. New York, 1986.

[7] F. Adama, K. M. Hello, S-J. Chai, The heterogenization of l-phenylalanine–Ru(III) complex and its application as catalyst in esterification of ethyl alcohol with acetic acid, Chem. Eng. Res. Des, 90 (2012) 633–642.

[8] R.M. Silverstein, F.X. Webster, D.J. Kiemle Eds. Spectrometric Identification of Organic Compounds. 7th ed. John Wiley & Sons Inc, Hoboken, 2005.

[9] H. Noei, O. Kozachuk, S. Amirjalayer, S. Bureekaew, M. Kauer, R. Schmid, B. Marler, M. Muhler, R. A. Fischer, Y. Wang, CO adsorption on mixed–valence ruthenium metal–organic framework studied by UHV–FTIR spectroscopy and DFT calculation, J. Phys. Chem. C 117 (2013) 5658−5666

[10] J. G. Małecki, Half-sandwich ruthenium(II) complexes with N- and N, (N,O)-donor ligands: Molecular, electronic structures, and computational study, Struct. Chem. 23 (2012) 461−472.

[11] A. A. Siller-Ceniceros, M. E. Sánchez-Castro, D. Morales-Acosta, J. R. Torres Lubian, E. Martínez G, F. J. Rodríguez Varela, Innovative functionalization of Vulcan XC-72 with Ru organometallic complex: Significant enhancement in catalytic activity of Pt/C electrocatalyst for the methanol oxidation reaction (MOR), Appl. Catal., B. 209 (2017) 455−467.

Chaper VI

6. Development of high performance Pt/C electrocatalysts for Methanol Oxidation Reaction (MOR) based on Vulcan functionalized with Ru–compounds

This section is covering all results obtained from physicochemical characterization of supports $C_{Ru\text{-}dim}$, $C_{Ru\text{-}com}$ and *C* (non-functionalized Vulcan). Additionally, is reported the physicochemical and electrochemical characterization of *Pt/C*, $Pt/C_{Ru\text{-}dim}$ and $Pt/C_{Ru\text{-}com}$ electrocatalysts.

6.1 Physicochemical characterization of $C_{Ru\text{-}dim}$, $C_{Ru\text{-}com}$ and C

6.1.2 FT–IR

Figure 6.1 shows the FT–IR spectra of $C_{Ru\text{-}dim}$, $C_{Ru\text{-}com}$ and non-functionalized Vulcan (*C*). The latter displays weak bands in the 600-1690 cm^{-1} range, attributed to the C–C, C–H and C–O vibrations of carbon [1, 2]. On the other hand, the positive effect of functionalization is shown for $C_{Ru\text{-}dim}$ *and* $C_{Ru\text{-}com}$. The intense absorption bands in the 3077–2854 and 1690–1477 cm^{-1} intervals are attributed to C–H and C=C vibrations, respectively. It is worth noticing that $C_{Ru\text{-}dim}$ displays a C=C band at 1520 cm^{-1} not observed for $C_{Ru\text{-}com}$. Moreover, C–O–H, C–O and C–H signals are also observed [3, 4]. At ca. 780 cm^{-1}, $C_{Ru\text{-}com}$ shows a high-intensity band corresponding to C–Cl stretchings ascribed to the interactions of Vulcan and ruthenium chloride [5]. Thus, it is concluded that *Ru–dim* and *Ru–com* modify the surface characteristics of Vulcan, developing functional groups that promote the anchorage of Pt nanoparticles.

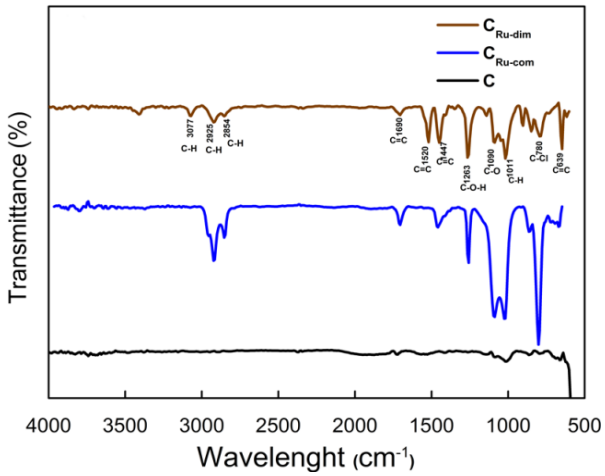

Figure 6.1 FT-IR spectra of $C_{Ru\text{-}dim}$, $C_{Ru\text{-}com}$ and C.

6.1.3 Raman

Figure 6.2 displays the Raman spectra of $C_{Ru\text{-}dim}$, $C_{Ru\text{-}com}$ and *C*. All the supports display the expected signals for carbon materials: i) the D band at ca. 1350 cm^{-1} related to lattice disorder, attributed to the C–C vibrations of the sp^3 defect sites; and ii) the G signal at ca. 1580 cm^{-1} corresponding to sp^2 hybridization from C=C bonds (graphitized lattice), due to π interactions [6, 7]. Additionally, two peaks at 604 and 466 cm^{-1} assigned to ruthenium-carbon interphases, can be observed at $C_{Ru\text{-}dim}$ and $C_{Ru\text{-}com}$, feature that correlates well with the reaction of ruthenium oxides and ruthenium crystals with organic molecules reported elsewhere [8, 9].

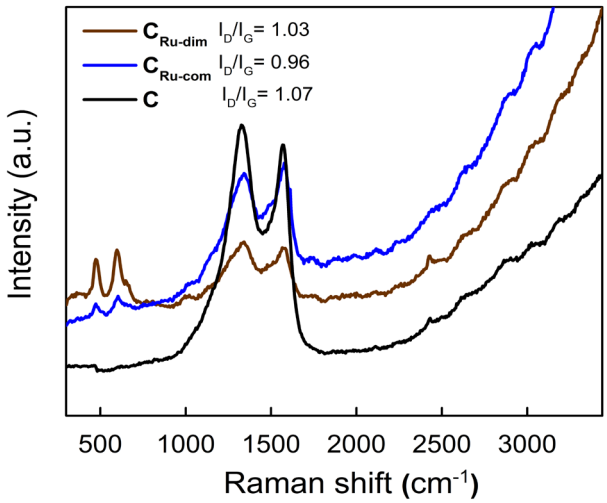

Figure 6.2 Raman spectra of $C_{Ru\text{-}dim}$, $C_{Ru\text{-}com}$ and *C*.

The degree of hybridization due to a shift from sp^2 to sp^3 orbitals can be determined from the ratio of the intensities of the D and G bands, I_D/I_G [10-13]. The ratios decrease from 1.07 for non–functionalized Vulcan, to 1.03 and 0.96 for $C_{Ru\text{-}dim}$ and $C_{Ru\text{-}com}$, respectively. Based on this behavior, it can be concluded that the graphitized lattice of Vulcan is not distorted during the formulation of $C_{Ru\text{-}dim}$ and $C_{Ru\text{-}com}$. To the best of our knowledge, organometallic surface modification of Vulcan has not been reported previously. However, the surface functionalization of carbon nanotubes and graphene with $[(\eta^6\text{–}C_6H_6)_2Cr]$ showed that bis-hexahapto-metal bonds are formed, preserving their graphitic band structure as reported elsewhere [14]. A similar reaction can be proposed for Vulcan based on the Raman spectra shown here, in what seems to be a constructive rehybridization [14].

6.1.4 SEM–EDS

SEM images in Figure 6.3 show the morphology of a) Vulcan, with typical semi–spherical particles; b) *Ru–dim*, having large irregularly-shaped crystals; c) $C_{Ru\text{-}dim}$, which shows mixed features of Vulcan and *Ru–dim*; and d) $C_{Ru\text{-}com}$, also with semi-spherical particles larger than those of Vulcan, attributed to the treatment with *Ru–com*.

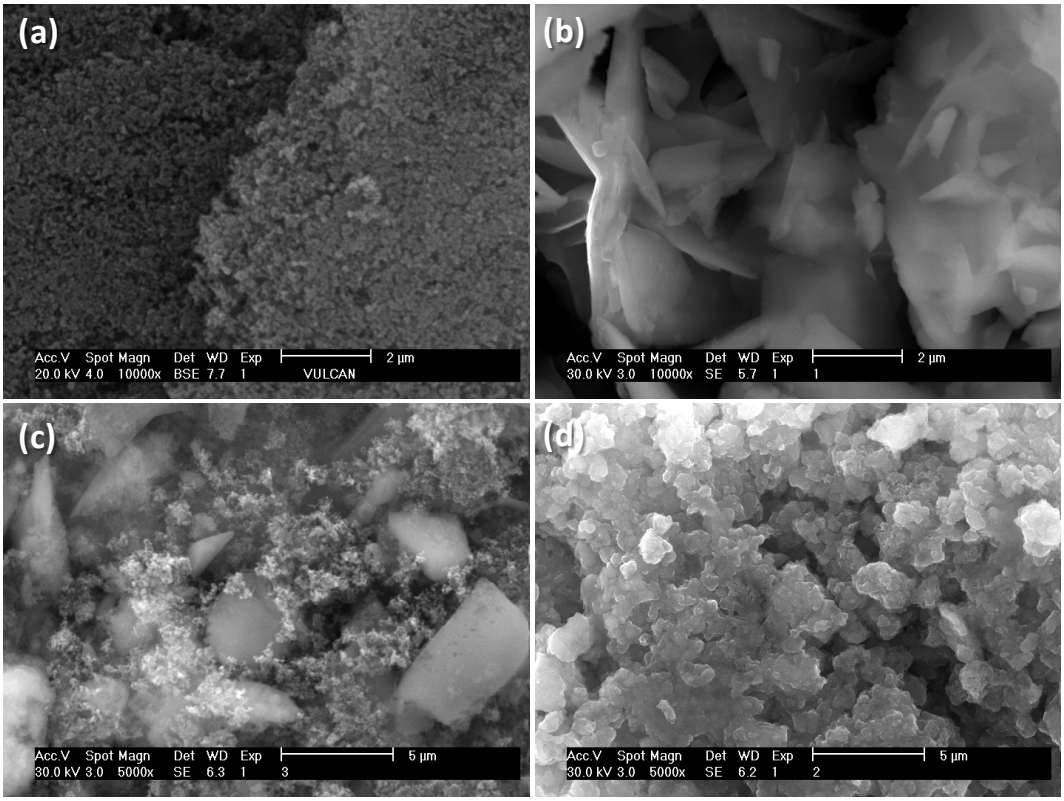

Figure 6.3 SEM micrographs of: a) C, b) *Ru-dim*, c) $C_{Ru\text{-}dim}$ and d) $C_{Ru\text{-}com}$.

The chemical composition of the functionalized supports obtained from EDS analysis is shown in Table 6.1 Paying attention on Ru, both have considerably large contents, higher in the case of $C_{Ru\text{-}dim}$ than $C_{Ru\text{-}com}$ (17.24 and 10.04 wt. %, respectively). It is interesting to mention that such high amounts of Ru confirm the chemical stability of the *Ru–dim* organometallic compound, since it remains on the surface of the carbon material after functionalization (seen also in Figure 6.3 c). Also, it is hypothesized that ruthenium atoms may be coordinated with carbon atoms on the graphitized segments of the lattice, although this should be confirmed with more studies of $C_{Ru\text{-}dim}$. Evidently, the carbon content has

decreased as a result of the surface modification of Vulcan with *Ru–dim* and *Ru–com*. The presence of O and Cl from the Ru chemical precursors is also reported in Table 6.1

Table 6.1 Chemical composition of $C_{Ru\text{-}dim}$ and $C_{Ru\text{-}com}$, from EDS analysis.

Support	C	Ru	O	Cl
	(wt. %)			
$C_{Ru\text{-}dim}$	65.72	17.24	4.63	12.40
$C_{Ru\text{-}com}$	71.90	10.04	7.96	9.82

6.2 Physicochemical characterization of the Pt/$C_{Ru\text{-}dim}$, Pt/$C_{Ru\text{-}com}$ and Pt/C electrocatalysts

6.2.1 XRD and EDS

The XRD pattern of Pt/C in Figure 6.4 a) shows the (111), (200), (220) and (311) reflections at 39.74°, 46.25°, 67.45° and 81.29° respectively (in 2θ scale), corresponding to fcc platinum (JCPDS 04-0802). A reflection at 24.92°, attributed to the (002) plane of carbon, is also observed. *Pt/$C_{Ru\text{-}com}$* has the same Pt features, while *Pt/$C_{Ru\text{-}dim}$* shows only the (111) and (311) Pt reflections. Two features attributed to the presence of Ru on the surface of the supports are observed for the patterns of *Pt/$C_{Ru\text{-}dim}$* and *Pt/$C_{Ru\text{-}com}$*: i) the peak due to carbon is not evident; and ii) a peak at about 9° can be clearly seen. Figure 4.4b) shows the deconvolution of the diffraction peak at low angles observed for *Pt/$C_{Ru\text{-}dim}$* and *Pt/$C_{Ru\text{-}com}$*. Three overlapped signals attributed to the (110), (101) and (102) ruthenium crystal planes (in 2θ positions of 7.6, 9.2 and 11.2, respectively) have been determined. This finding confirms that the reflection can be ascribed to Ru, in good agreement with the literature [15,16].

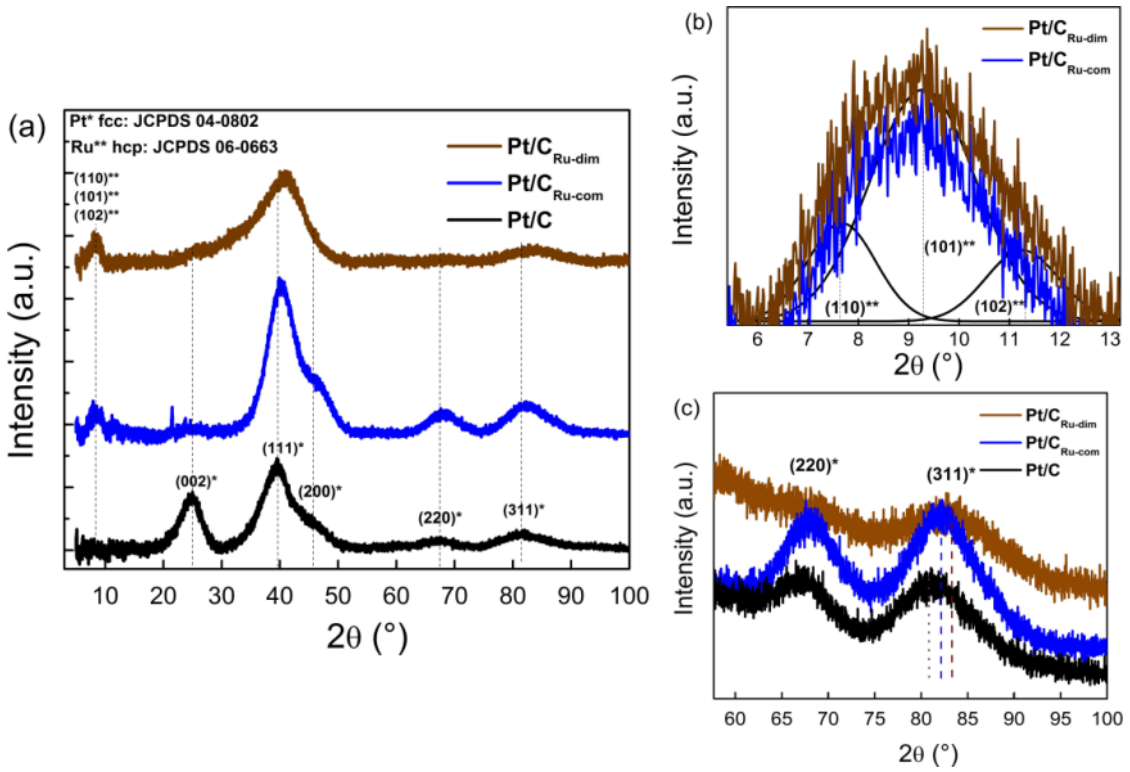

Figure 6.4 (a) XRD patterns of *Pt/C*$_{Ru\text{-}dim}$, *Pt/C*$_{Ru\text{-}com}$ and *Pt/C*. (b) Zooming of the 5-13° (2θ) range. (c) Zooming of the (220) and (311) Pt reflections.

Figure 6.4 c) shows the shift towards higher angles of the Pt (311) plane at *Pt/C*$_{Ru\text{-}dim}$ and *Pt/C*$_{Ru\text{-}com}$ relative to Pt/C. It is to be noticed that the displacement is almost 2° in the 2θ scale for *Pt/C*$_{Ru\text{-}dim}$ (Table 6.2), larger than those reported for Pt–Ru alloys synthesized by the polyol and other methods [17-20]. This is evidence that Pt nanoparticles and Ru atoms from the organometallic compound form Pt–Ru alloyed phases at *Pt/C*$_{Ru\text{-}dim}$. The same can be argued for *Pt/C*$_{Ru\text{-}com}$ since it also shows a shift in the (311) plane (Table 6.2).

Table 6.2. Structural parameters of the electrocatalysts from the (311) Pt reflection.

Electrocatalyst	**Peak position (°)**	**a_{fcc} (nm)**	**X_{Ru} (%)**	**d, XRD (nm)**	**d, TEM (nm)**
Pt/C	81.22	0.398	-	2.05	1.91
Pt/C$_{Ru\text{-}com}$	82.37	0.331	0.489	1.89	1.87
Pt/C$_{Ru\text{-}dim}$	83.13	0.283	0.509	1.49	2.59

To confirm this claim, the degree of alloying has been analyzed from the data of reflection (311). The lattice parameter (a_{fcc}) of *Pt/C*$_{Ru\text{-}dim}$, *Pt/C*$_{Ru\text{-}com}$ and *Pt/C* is determined according to the well-known equation (6.1), as reported elsewhere [21]:

Equation 6.1: $$a_{fcc}=\frac{\sqrt{2}\,\lambda_{\alpha_1}}{\sin\theta_{max}}$$

Where $\lambda_{\alpha 1}$ is the X-ray wavelength (1.54056 Å) and θ_{max} is the peak angle. Using Vegard's law [22], the atomic fraction of Ru alloyed (X_{Ru}) is calculated with Equation (6.2) [23]:

Equation 6.2: $$a_{fcc}= l_{oc}- k\,X_{Ru}$$

Where l_{oc} = 3.9155 Å is the lattice parameter for pure platinum supported on carbon and k = 0.124 Å is a constant. The values of a_{fcc} and X_{Ru} are given in Table 6.2. *Pt/C*$_{Ru\text{-}dim}$ and *Pt/C*$_{Ru\text{-}com}$ have a significant lattice contraction relative to Pt/C. Particularly, *Pt/C*$_{Ru\text{-}dim}$ shows the strongest reduction resulting in a_{fcc} = 0.283 nm, which is smaller than the value reported for bulk Pt–Ru alloys [21]. Additionally, the atomic fraction of Ru alloyed on *Pt/C*$_{Ru\text{-}dim}$ and *Pt/C*$_{Ru\text{-}com}$ is approximately 50 %, higher than values reported for Pt–Ru/C alloys synthesized by some workers [20,23,24] and similar to a commercial Pt–Ru black [19]. Therefore, the experimental procedure is highly efficient to alloy Ru with Pt, reaching an important value starting from the *Ru-dim*: Vulcan molar ratio of 1:10 proposed here.

The crystallite size of the electrocatalysts (d) is calculated from the (311) diffraction peak using the Scherrer's equation [25]:

Equation 6.3: $$d=\frac{0.9\times\lambda_{\alpha 1}}{\beta_{2\theta}\times\cos\theta_{max}}$$

Where $\lambda_{\alpha 1}$ and θ_{max} have the same meaning as in equation (6.1) and $\beta_{2\theta}$ is the full width at half maximum (FWHM) of the peak. The d values are given in Table 6.2. All the electrocatatalysts show nanostructured characteristics, nevertheless, the smallest value is that of Pt/C$_{Ru\text{-}dim}$ (1.49 nm).

Table 6.3. Chemical composition from EDS analysis and ECSA values of the electrocatalyts.

Electrocatalyst	C	Pt	Ru	Cl	O	ECSA
	(wt. %)					($m^2\ g_{Pt}^{-1}$)
Pt/C	81.93	18.07	–	–	–	47.75
$Pt/C_{Ru\text{-}com}$	57.56	23.68	7.68	0.54	10.54	41.90
$Pt/C_{Ru\text{-}dim}$	42.64	26.82	20.74	1.17	8.62	47.27

The chemical composition of the electrocatalysts (from EDS) is given in Table 6.3. *Pt/C* shows metal and carbon contents (18.07 and 81.93 wt. %, respectively) close to the nominal value of 20:80 (wt. %). On the other hand, $Pt/C_{Ru\text{-}com}$ and $Pt/C_{Ru\text{-}dim}$ have higher Pt content (23.68 and 26.82 wt. %, respectively). Interestingly, these two anodes have a significant amount of Ru, which in the case of $Pt/C_{Ru\text{-}dim}$ is three times higher (20.74 wt. %). Their carbon content has decreased significantly since Ru must be anchored on the surface of Vulcan, somehow hindering the support. The chemical composition analysis explains in part the fact that the C (002) peak is missing in the XRD profiles of $Pt/C_{Ru\text{-}dim}$ and $Pt/C_{Ru\text{-}com}$. Cl and O have also been detected for $Pt/C_{Ru\text{-}dim}$ and $Pt/C_{Ru\text{-}com}$. Both in Table 6.1 and 6.3, the Cl content is higher in the presence of *Ru-dim*, which can be attributed to the larger Cl–Ru bonds at the organometallic structure, relative to *Ru–com*.

6.2.2 HR–TEM

The image in Figure 6.5a) shows the morphology of *Pt/C*, with platinum nanoparticles homogeneously dispersed over Vulcan. The histogram in Figure 6.5b) indicates that the average particle size (d) of Pt nanoparticles is 1.91 nm, in good agreement with the value determined from XRD analysis (Table 6.2). The nanostructured characteristic of *Pt/C* is observed more clearly in the HR-TEM micrograph of Figure 6.5c), where the inset is a Selected Area Electron Diffraction (SAED) pattern with a distance between lattice fringes of 0.23 nm, attributed to Pt (111). On the other hand, the micrograph of $Pt/C_{Ru\text{-}com}$ in Figure 6.5d) shows that Pt nanoparticles are homogeneously dispersed over the entire surface of $C_{Ru\text{-}com}$. The d value from the histogram in Figure 6.5e) is 1.87 nm, basically the same as that from XRD (Table 6.2). Figure 6.5f) is a HR–TEM image of $Pt/C_{Ru\text{-}com}$. From the SAED pattern in the inset, distances between lattice fringes of 0.23 and 0.20 nm have been obtained and ascribed to Pt (111) and Ru (101), respectively [26–29].

Figure 6.6a) is a TEM micrograph of $Pt/C_{Ru\text{-}dim}$, showing that the support is more densely covered by metallic nanoparticles than in the case of *Pt/C* and $Pt/C_{Ru\text{-}com}$. Figure 6.6b) is the corresponding histogram indicating that d= 2.29 nm (Table 6.2). The larger value compared to that determined from XRD can be in part due to the fact that the nanoparticles actually

touch each other, avoiding a clear delimitation of the boundaries. Even though, such d value confirms the nanostructured nature of the Pt metallic nanoparticles anchored over $C_{Ru\text{-}dim}$. The elemental mapping in STEM mode (Figure 6.6c) confirms the presence of Pt and Ru, and demonstrates that both metals are homogeneously dispersed over the support. Figure 6.6d) is a HR–TEM image of $Pt/C_{Ru\text{-}dim}$, where the SAED pattern allows the determination of distances between lattice fringes of 0.23 and 0.20 nm, attributed also to Pt (111) and Ru (101) respectively [26–29].

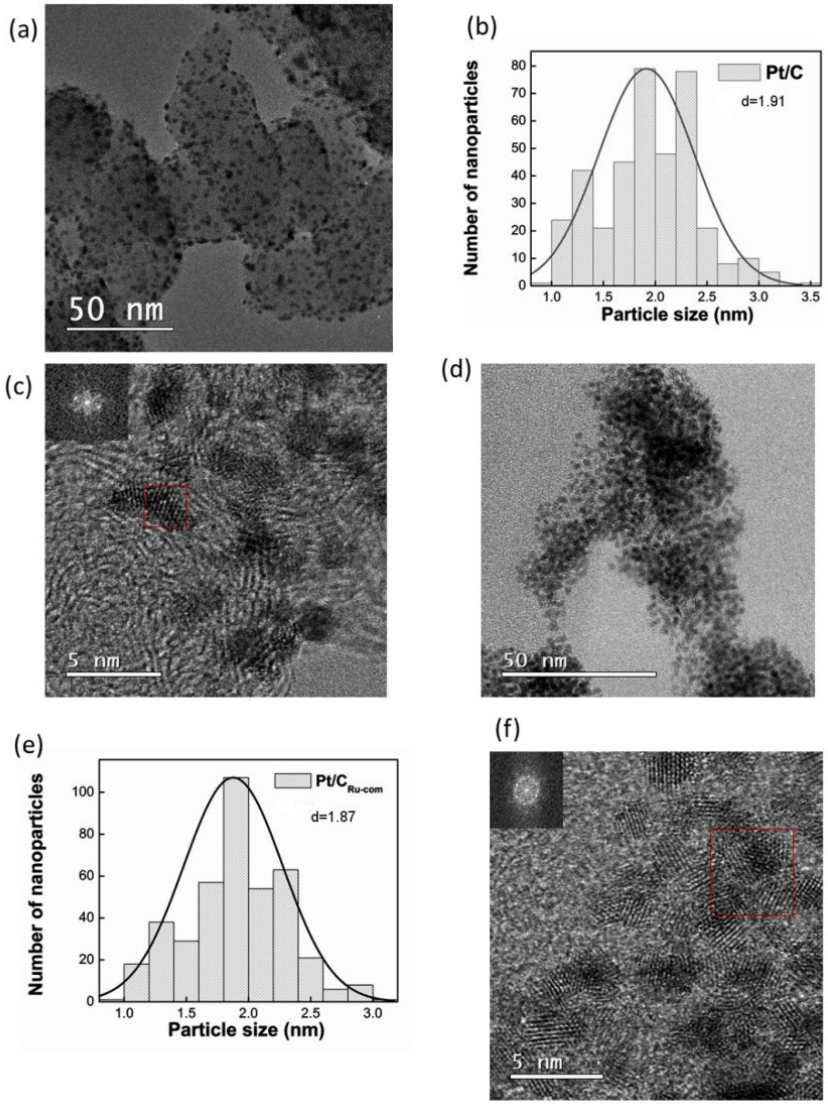

Figure 6.5 TEM micrograph, histogram and HR–TEM image of *Pt/C* (a–c) and $Pt/C_{Ru\text{-}com}$ (d–f). SAED patterns from the regions in the red squares are shown in the insets.

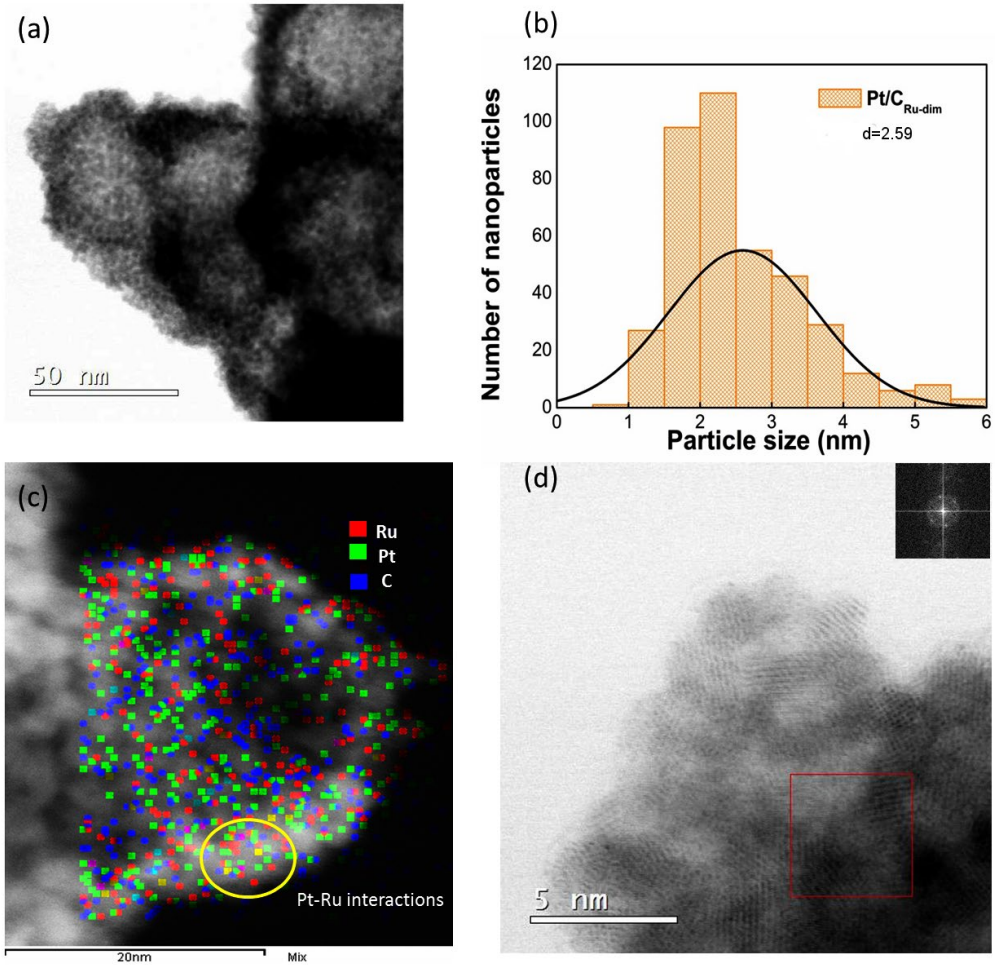

Figure 6.6 Analysis of *Pt/C*$_{Ru\text{-}dim}$: (a) TEM micrograph, (b) Histogram of particle distribution, (c) Elemental mapping and (d) HR–TEM image. SAED pattern from the region in the red square is shown in the inset.

6.2.3 XPS

Figure 6.7a) shows the C1s spectrum of *Pt/C*, where the most intense signal is that of carbon sp^2 hybridization at a binding energy (BE) of 284.1 eV. The smaller C sp^3 peak emerges at higher BE.

As previously reported in the literature for Carbon Nanotubes and Graphene [14], Ru atoms may bond with graphitic carbon via hexa–hapto coordination of the (η^6–C_6H_6–M) type, preserving the sp^2 hybridization. Figure 6.7b) and c) are the C1s and Ru3d spectra for *Pt/C*$_{Ru\text{-}dim}$ and *Pt/C*$_{Ru\text{-}com}$, respectively, showing significant differences compared to *Pt/C*. The C1s BE overlaps with the Ru3d region, as seen by the presence of Ru $3d_{5/2}$ and Ru $3d_{3/2}$ doublets of metallic Ru and RuO_2, Ru^0 and Ru^{IV}, respectively. *Pt/C*$_{Ru\text{-}dim}$ shows a decrease in the

relative intensities of C sp^2 and sp^3 (compared to *Pt/C*) and higher peaks attributed to the Ru^0 doublet. Its Ru^{IV} doublet is less intense if compared with the metallic contribution. On the other hand, the highest peak for $Pt/C_{Ru\text{-}com}$ is that of C sp^2, with the Ru^0 and Ru^{IV} doublets as well as C sp^3 showing lower relative intensities. Even more, Figure 6.7d) and e) show the doublets due to Ru and RuO_2 in the Ru3p BE region. $Pt/C_{Ru\text{-}dim}$ has higher relative intensities of the Ru $3p_{3/2}$ and Ru $3p_{1/2}$ peaks compared to $Pt/C_{Ru\text{-}com}$, indicating a larger ruthenium concentration.

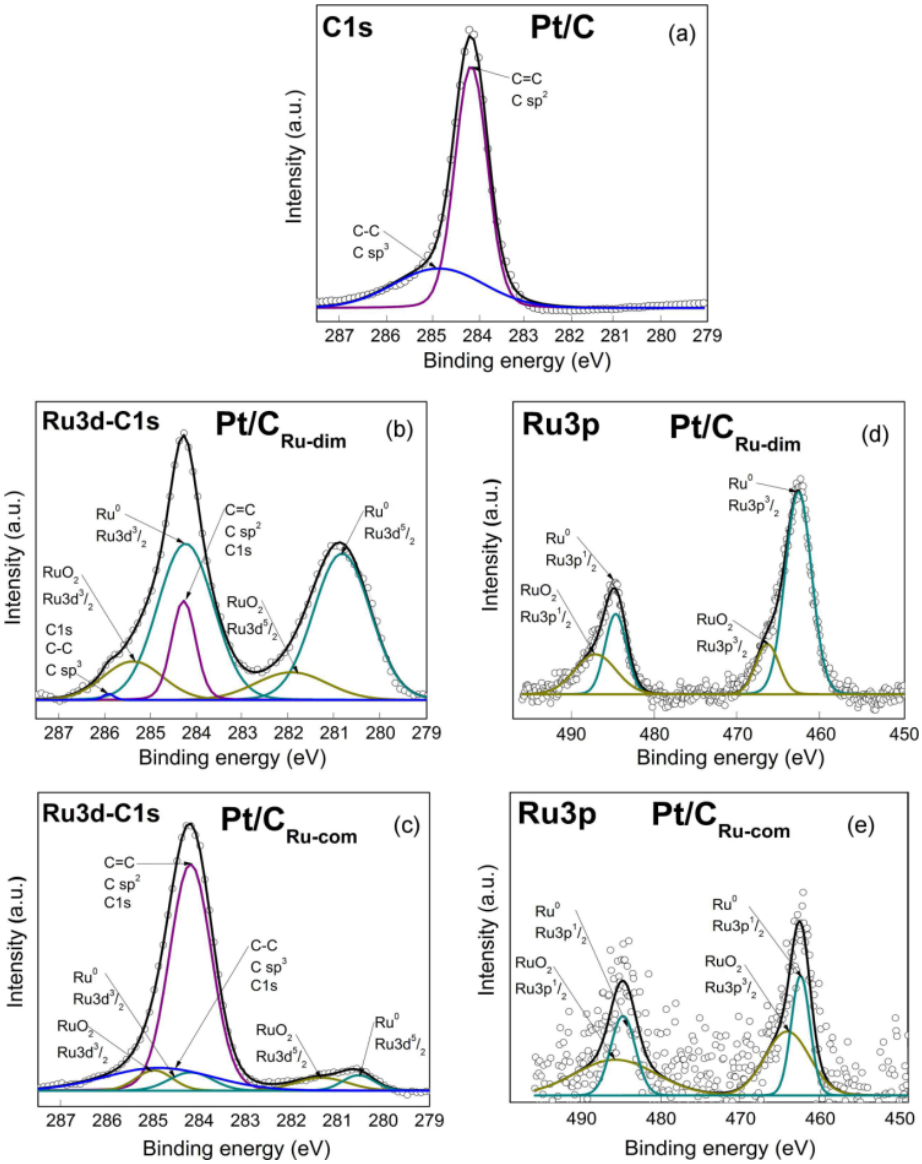

Figure 6.7 XPS spectra of the electrocatalysts: a) C1s region of *Pt/C*, b–c) Overlapped Ru3d–C1s regions of $Pt/C_{Ru\text{-}dim}$ and $Pt/C_{Ru\text{-}com}$, d–e) Ru3p region of $Pt/C_{Ru\text{-}dim}$ and $Pt/C_{Ru\text{-}com}$.

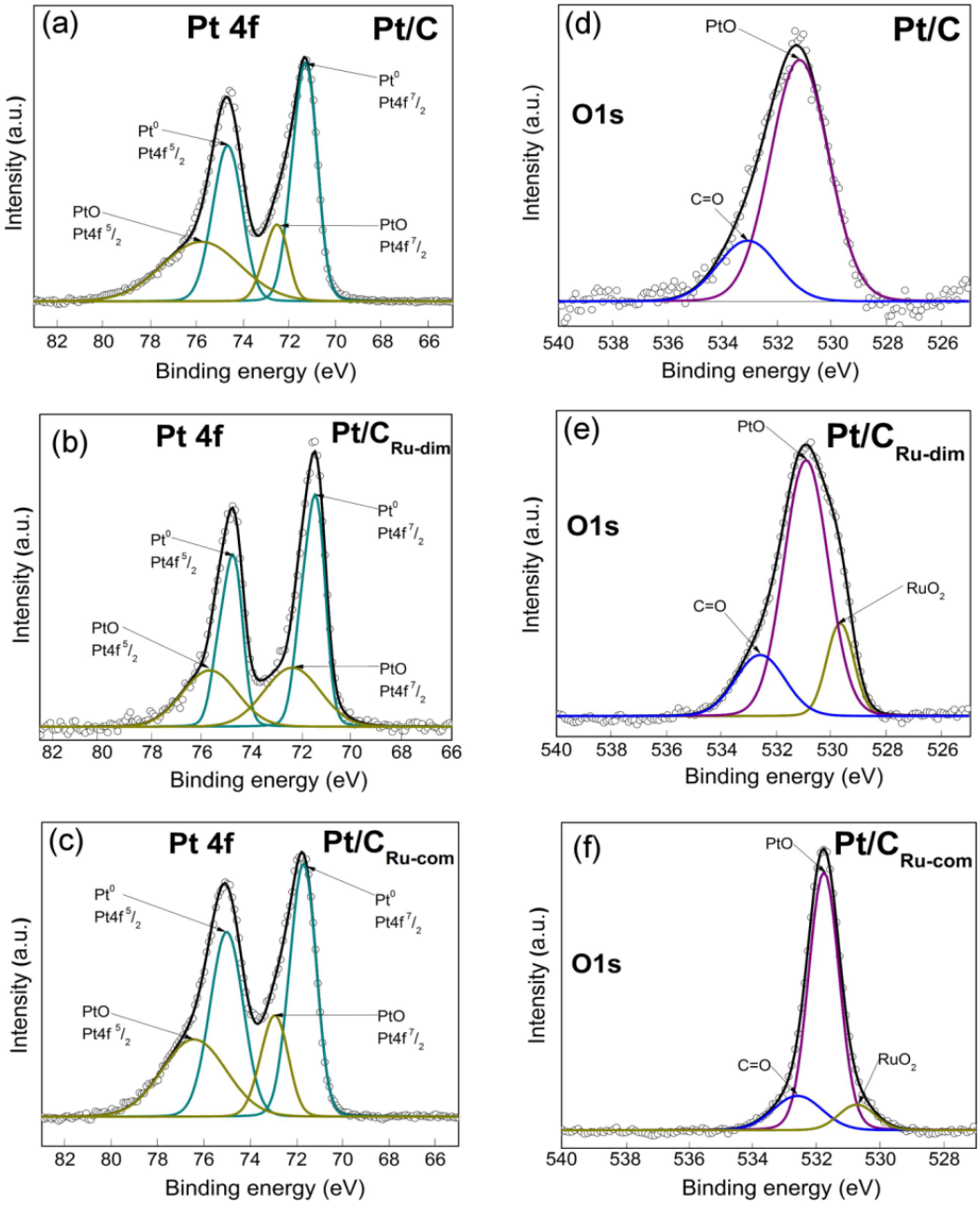

Figure 6.8 XPS spectra of *Pt/C*, *Pt/C*$_{Ru\text{-}dim}$ and *Pt/C*$_{Ru\text{-}com}$: a–c) Pt 4f region, d–f) O1s region.

Figure 6.8 a–c) shows the Pt 4f BE region for the electrocatalysts, with doublets from the spin-orbit splitting of the $4f_{7/2}$ and $4f_{5/2}$ states due to metallic Pt and PtO (Pt^0 and Pt^{II}, respectively). The Pt spin-orbit splitting are the largest on *Pt/C*$_{Ru\text{-}dim}$ (3.40 and 3.45 eV), followed by *Pt/C*$_{Ru\text{-}com}$ (3.28 and 3.31 eV) and *Pt/C* (3.26 and 3.24 eV), as given in Table 4.4.

Also, the BE of Pt^0 in the $4f_{7/2}$ state is shifted from 71.31 eV in the case of Pt/C, to 71.63 and 71.50 eV for *Pt/C*$_{Ru\text{-}dim}$ (0.32 eV displacement) and *Pt/C*$_{Ru\text{-}com}$ (0.19 eV displacement), respectively. The electronic modification of *Pt/C*$_{Ru\text{-}dim}$ and *Pt/C*$_{Ru\text{-}com}$ corresponds to a change of the *d*-valence band of Pt, attributed to an electron transfer from Ru to Pt atoms, and clearly suggests the formation of Pt–Ru alloyed phases. A similar behavior is pointed out by Watanabe *et al.* [30] where the core level of Pt $4f_{7/2}$ associated to a Pt–Ru alloy has been observed to shift 0.39 eV to higher BE with respect to that for pure Pt, due to differences in their work functions. Therefore, shift in BE of Pt/C$_{Ru\text{-}dim}$ is close to the one reported in [30].

Moreover, the spin-orbit splitting of Ru $3p_{3/2}$ and Ru $3p_{1/2}$ are also given in Table 6.4. The values are larger for *Pt/C*$_{Ru\text{-}com}$ compared to *Pt/C*$_{Ru\text{-}dim}$. On the other hand, the analysis of the O1s core level region in Figure 6.8d–f) corroborates the existence of PtO and C=O bonds on Pt/C. Besides that, RuO_2 bonds are observed for *Pt/C*$_{Ru\text{-}dim}$ and *Pt/C*$_{Ru\text{-}com}$.

Table 6.4. XPS parameters of the electrocatalysts.

Electrocatalyst	Species	State	BE (eV)	Doublet splitting (eV)	Composition (at. %)
Pt/C	Pt^0	Pt $4f_{7/2}$	71.31	3.26	3.53
		Pt $4f_{5/2}$	74.57		3.76
	PtO	Pt $4f_{7/2}$	72.57	3.24	2.74
		Pt $4f_{5/2}$	75.81		1.50
		O1s	531.23		7.65
	C sp^2	C1s	284.15		78.82
		O1s	532.70		1.97
Pt/C$_{Ru\text{-}dim}$	Pt^0	Pt $4f_{7/2}$	71.63	3.40	4.64
		Pt $4f_{5/2}$	75.03		5.86
	PtO	Pt $4f_{7/2}$	72.94	3.45	1.94
		Pt $4f_{5/2}$	76.39		4.73
		O1s	530.95		31.04
	Ru^0	Ru3p $_{3/2}$	466.45	20.82	10.93
		Ru3p $_{1/2}$	487.27		7.04
	RuO_2	Ru3p $_{3/2}$	462.78	21.89	2.39
		Ru3p $_{1/2}$	484.67		6.79
		O1s	529.72		6.96
	C sp^2	C1s	284.29		9.39
		O1s	532.62		8.24

$Pt/C_{Ru\text{-}com}$	Pt^0	Pt 4f $_{7/2}$	71.50	3.28	6.34
		Pt 4f $_{5/2}$	74.78		6.74
	PtO	Pt 4f $_{7/2}$	72.38	3.31	4.93
		Pt 4f $_{5/2}$	75.69		2.69
		O1s	531.78		28.41
	Ru^0	Ru3p $_{3/2}$	464.14	21.85	0.93
		Ru3p $_{1/2}$	485.99		1.64
	RuO_2	Ru3p $_{3/2}$	462.50	22.35	1.19
		Ru3p $_{1/2}$	484.85		2.44
		O1s	530.72		3.31
	C sp^2	C1s	284.19		35.40
		O1s	532.59		5.94

The chemical composition of the electrocatalysts calculated by XPS results is presented in Table 6.4. The C sp^2 content is 78.82, 9.39 and 35.4 (at. %) for *Pt/C*, $Pt/C_{Ru\text{-}dim}$ and $Pt/C_{Ru\text{-}com}$, respectively. This result showing a lower C content at $Pt/C_{Ru\text{-}dim}$ and $Pt/C_{Ru\text{-}com}$ can be related to the significant presence of Ru after functionalization of Vulcan (Table 6.3). In the case of the Pt^0 and Pt^{II} species, $Pt/C_{Ru\text{-}com}$ shows the larger concentration, followed by $Pt/C_{Ru\text{-}dim}$. Nevertheless, it should be pointed out that $Pt/C_{Ru\text{-}dim}$ has higher Ru^0 and RuO_2 content than $Pt/C_{Ru\text{-}com}$. The relevant role of RuO_2 on the catalytic activity of Pt–Ru/C alloys for the Ethanol Oxidation Reaction has been determined elsewhere [31], at which an increased performance compared to *Pt/C* was attributed to an easier oxygen transfer at more negative potentials. The RuO_2 species may also be important in the catalytic activity for the MOR, as discussed later in this work.

6.3 Electrochemical characterization of the Pt/C electrocatalysts

6.3.1 Catalytic activity of Pt/ $C_{Ru\text{-}dim}$, $Pt/C_{Ru\text{-}com}$ and Pt/C for the MOR

The CVs of the electrocatalysts in Figure 6.9 show the characteristic regions of platinum materials: i) hydrogen adsorption and desorption ($H_{ads/des}$) in the potential range of 50–250 mV vs. SHE; ii) double layer (250–700 mV vs. SHE); iii) Pt–oxides formation/reduction (700–1200 mV vs. SHE). The shape of Pt/C is that of a monometallic supported electrocatalysts [32,33], with 3 H_{des} peaks identified. It also has a relatively thin double layer with the current density in the positive scan parallel to the zero-current line. Moreover, the onset potential of the Pt–oxides formation and the peak current density due to their reduction are distinguishable.

Pt/C$_{Ru\text{-}dim}$ and *Pt/C*$_{Ru\text{-}com}$ show some differences relative to *Pt/C*. The hydrogen peaks are hindered, and the double layer region is wider, exposing a current density slope up to the Pt–oxides region. Due to this feature, the onset potential of the oxides formation is not detected. Similar characteristics are attributed to the presence of Ru and the formation of RuOH species on Pt–Ru/C alloys [33] and suggest the formation of alloyed Pt–Ru at *Pt/C*$_{Ru\text{-}dim}$ and *Pt/C*$_{Ru\text{-}com}$ in accordance with their XRD, TEM and XPS characterization.

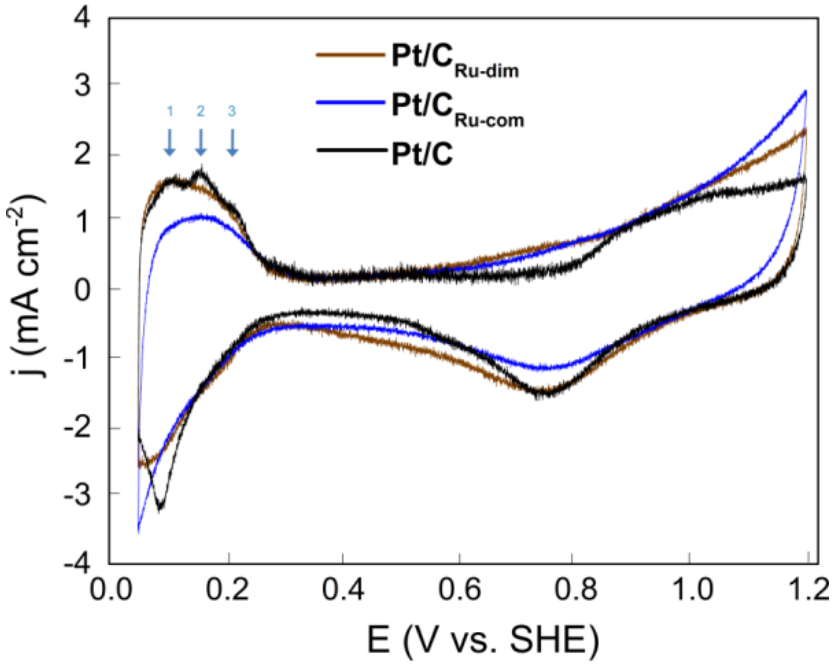

Figure 6.9 CVs of *Pt/C*, *Pt/C*$_{Ru\text{-}dim}$ and *Pt/C*$_{Ru\text{-}com}$ in Ar–saturated 0.5 M H_2SO_4. Scan rate: 20 mV s^{-1}.

The electrochemically active surface area (ECSA, in m^2 g_{Pt}^{-1}) is calculated from the H_{des} region of the CVs in Figure 6.9 (after correction the corresponding area related to the double layer) with equation (6.4):

Equation 6.4: $$ECSA = \frac{Q}{Q_{H_{des}} x\, L_{Pt}}$$

Where Q is the charge under the curve (μC), Q_{Hdes} is the theoretical charge due to the adsorption of hydrogen on Pt (210 μC cm^{-2}) and L_{Pt} (μg) is the amount of Pt on the electrodes obtained from the chemical composition. The ECSA value of *Pt/C*$_{Ru\text{-}dim}$ is similar to that of

Pt/C (47.75 and 47.27 $m^2\ g_{Pt}^{-1}$, respectively) and higher than the 41.90 $m^2\ g_{Pt}^{-1}$ determined for *Pt/C*$_{Ru\text{-}com}$ (Table 6.3).

The catalytic activity of the electrocatalysts for the MOR is shown in the polarization curves of Figure 6.10. *Pt/C*$_{Ru\text{-}dim}$ delivers a current density (j) of 45.0 mA cm^{-2}, an almost two–fold increase compared to Pt/C$_{Ru\text{-}com}$ and Pt/C (Table 6.5). The onset potential of the MOR (E_{onset}) at *Pt/C*$_{Ru\text{-}dim}$ is 0.25 V, significantly more negative than the values determined for Pt/C$_{Ru\text{-}com}$ and *Pt/C* (0.35 and 0.39 V, respectively). Moreover, the current density ratios in the forward and the backward scan (j_f/j_b), are 1.3, 1.3 and 0.8 for *Pt/C*$_{Ru\text{-}dim}$, *Pt/C*$_{Ru\text{-}com}$ and *Pt/C*, respectively. Therefore, the Ru–containing electrocatalysts are more efficient for the oxidation of methanol with low formation of intermediates. The electrochemical parameters given in Table 6.5, demonstrate the enhanced catalytic activity of *Pt/C*$_{Ru\text{-}dim}$ for the MOR compared to the two other anodes. Overall, the catalytic activity decreases in the order *Pt/C*$_{Ru\text{-}dim}$ > *Pt/C*$_{Ru\text{-}com}$ > *Pt/C*.

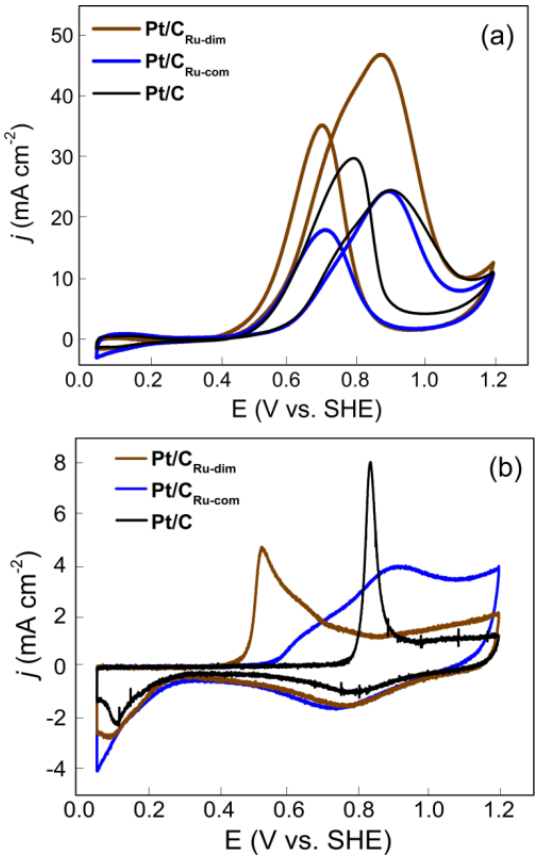

Figure 6.10 a) CVs of the ROM at *Pt/C*$_{Ru\text{-}dim}$, *Pt/C*$_{Ru\text{-}com}$ and *Pt/C*. Electrolyte: Ar–saturated 0.5 M H_2SO_4 + 0.5 M CH_3OH. Scan rate: 20 mV s^{-1}. b) CO–stripping curves for the electrocatalysts in 0.5 M H_2SO_4 at the same scan rate.

It is well–known that CO_{ads} is produced as intermediate species during the MOR, poisoning and limiting the catalytic activity of Pt-alone nanomaterials [34,35]. Therefore, anode electrocatalysts for DMFCs must fulfill the requirement of high tolerance to such species. Pt–Ru/C alloys are highly active for the MOR in part because of the bifunctional mechanism, since the formation of $(OH)_{ads}$ species starts earlier on Ru than on Pt [36].

Figure 6.10b) depicts the electrochemical response of *Pt/C*$_{Ru\text{-}dim}$, *Pt/C*$_{Ru\text{-}com}$ and *Pt/C* during CO–stripping measurements. The latter shows a narrow CO oxidation peak with E_{onset} = 0.76 V, j = 8.0 mA cm^{-2} and a maximum j value at E_{max} = 0.83 V (Table 6.5). Meanwhile, on the *Pt/C*$_{Ru\text{-}com}$ and *Pt/C*$_{Ru\text{-}dim}$ electrocatalysts the CO oxidation proceeds in a different fashion, with remarkably broad peaks. It is interesting to observe the formation of two peaks (at ca. 0.65 and 0.90 V) on *Pt/C*$_{Ru\text{-}com}$, indicating the oxidation of two CO–like species adsorbed on Pt sites at different energies. This electrocatalyst oxidizes CO with E_{onset} = 0.53 V, a value more negative than that of Pt/C.

On the other hand, it is worth noting the behavior to *Pt/C*$_{Ru\text{-}dim}$, at which the CO oxidation reaction starts at E_{onset} = 0.43 V, i.e., 320 mV more negative than Pt/C. Moreover, j = 4.7 mA cm^{-2} and E_{max} = 0.52 V at this electrocatalyst (Table 6.5). A peak at ca. 0.65 V is also observed, similar to the CO–like species indicated for *Pt/C*$_{Ru\text{-}com}$ at the same potential. This result indicates that CO_{ads} is more weakly adsorbed on *Pt/C*$_{Ru\text{-}dim}$ and therefore can be oxidized at lower potentials relative to *Pt/C*$_{Ru\text{-}com}$ and *Pt/C*.

Table 6.5 Electrochemical parameters for *Pt/C*$_{Ru\text{-}dim}$, *Pt/C*$_{Ru\text{-}com}$ and *Pt/C* during the MOR and the CO–stripping evaluation.

Electrocatalyst	**MOR**				**CO-stripping**		
	j_{geo} (mA cm^{-2})	**j_{mass} (mA mg$^{-1}_{Pt}$)**	**E_{onset} (V)**	**j_f/j_b ratio**	**j (mA cm^{-2})**	**E_{onset} (V)**	**E_{max} (V)**
Pt/C	24.6	269.7	0.39	0.8	8.0	0.76	0.83
Pt/C$_{Ru\text{-}com}$	24.5	203.8	0.35	1.3	-	0.53	-
Pt/C$_{Ru\text{-}dim}$	45.0	344.2	0.25	1.3	4.7	0.43	0.52

Here, it is proposed that the bi-functional mechanism proceeds on *Pt/C*$_{Ru\text{-}dim}$ during the MOR, i.e., $(OH)_{ads}$ species are formed on the Ru sites generated from the organometallic compound at low potentials and transferred to the Pt atoms. Consequently, the oxidation of CO_{ads} is highly improved, thus enhancing its catalytic activity for the MOR. Also, the catalytic behavior of *Pt/C*$_{Ru\text{-}dim}$ for the MOR can be attributed to the ligand effect. The shift in BE due to the electronic effect of Ru on Pt observed from XPS analysis indicates a weaker adsorption

of CO–like species at the electrocatalysts [31], i.e., it can be oxidized at lower potentials, in agreement with the results in Figure 6.10b). Even more, the high RuO_2 content at *Pt/C*$_{Ru\text{-}dim}$ may have played a beneficial role on its high performance for the MOR.

Conclusions

Chapter VI

Vulcan was functionalized with the $[(\eta^6\text{–}C_6H_5OCH_2CH_2OH)RuCl_2]_2$ organometallic compound to produce *C*$_{Ru\text{-}dim}$, having several functional groups as identified by FT–IR. Raman analysis revealed an apparent chemical interaction between ruthenium and the graphitic phase of Vulcan, maintaining the sp^2 hybridization typical of ordered carbon.

Pt/C$_{Ru\text{-}dim}$ showed physicochemical characteristics that strongly suggest the formation of alloyed Pt-Ru phases.

- From XRD: shift in diffraction peaks, presence of reflections attributed to Ru, contraction of a_{fcc} and nearly 50% X_{Ru}.

- From TEM: chemical mapping showing the homogeneous dispersion of Pt and Ru nanoparticles, and identification of distances between lattice fringes ascribed to Pt and Ru.

- From XPS: The identification of Ru^0 and RuO_2 bonds, besides those of Pt^0 and PtO. A shift to higher BE of Pt^0 in the $4f_{7/2}$ state.

$Pt/C_{Ru\text{-}dim}$ showed a higher catalytic activity for the MOR considering the j, E_{onset} and j_f/j_b values. It also demonstrated a significant increased tolerance to CO_{ads} relative to $Pt/C_{Ru\text{-}com}$ and Pt/C. The electrocatalytic behavior of $Pt/C_{Ru\text{-}dim}$ was attributed to the bifunctional mechanism, the ligand effect and the presence of RuO_2.

The physicochemical characteristics and excellent electrochemical response of *Pt/C*$_{Ru\text{-}dim}$ opens the opportunity for the design of electrocatalysts for specific fuel cell reactions, employing organometallic compounds as agents for functionalization. For example: Pt/C_{Sn} for the ethanol oxidation reaction or Pt/C_M (where M=Co, Fe, Ni, etc.) for the Oxygen Reduction Reaction. The potential application is also there for other carbonaceous supports, such as Graphene, Carbon Nanotubes and Ordered Mesoporous Carbon, instead of Vulcan.

References

Chapter VI

[1] V. Tucureanu, A. Matei, A. M. Avram, Crit. Rev. Anal. Chem. 2016, 0, DOI: 10.1080/10408347.2016.1157013

[2] F. Rositani, P. L. Antonucci, M. Minutoli, N. Giordano, Infrared analysis of carbon blacks, Carbon 25 (1987) 325–332.

[3] S. Wang, D. Yu, L. Dai, D.W. Chang, J.-B. Baek, Polyelectrolyte-functionalized graphene as metal-free electrocatalysts for oxygen reduction, ACS Nano 5 (2011) 6202–6209.

[4] G. Selvarani, A. K. Sahu, N.A. Choudhury, P. Sridhar, S. Pitchumani, A.K. Shukla, A phenyl-sulfonic acid anchored carbon-supported platinum catalyst for polymer electrolyte fuel cell electrodes, Electrochim. Acta 52 (2007) 4871–4877.

[5] R. M. Silverstein, F. X. Webster, D. J. Kiemle, in Spectrometric identification of organic compounds, John Wiley & Sons Inc., 7th ed., Hoboken, NJ, USA 2005.

[6] M. S. Dresselhaus, A. Jorio, A. G. Souza-Filho, R. Saito, Defect characterization in graphene and carbon nanotubes using Raman spectroscopy, Phil. Trans. R. Soc. A 368 (2010) 5355–5377.

[7] A. C. Ferrari, Raman spectroscopy of graphene and graphite: Disorder, electron–phonon coupling, doping and nonadiabatic effects, Solid State Commun. 143 (2007) 47–57.

[8] A-X. Yin, W-Ch. Liu, J. Ke, W. Zhu, J. Gu, Y-W. Zhang, Ch-H. Yan, Ru nanocrystals with shape-dependent surface-enhanced raman spectra and catalytic properties: controlled synthesis and DFT calculations, J. Am. Chem. Soc. 134 (2012) 20479–20489.

[9] H. Kim, B. N. Popov, Characterization of hydrous ruthenium oxide/carbon nanocomposite supercapacitors prepared by a colloidal method, J. Power Sources 104 (2002) 52–61.

[10] D. Akbar, Ü. E. Güngör, Determination of the incorporation rate of PTFE particles in Au-Co-PTFE composite coatings by InfraRed Reflection Absorption Spectroscopy, Surf. Coat. Technol. 240 (2014) 233–241.

[11] M. A. Pimenta, G. Dresselhaus, M. S. Dresselhaus, L. G. Cancado, A. Jorio, R. Saito, Studying disorder in graphite-based systems by Raman spectroscopy, Phys. Chem. Chem. Phys. 9 (2007) 1276–1290.

[12] S. Sarkar, H. Zhang, J-W. Huang, F. Wang, E. Bekyarova, C. N. Lau, R. C. Haddon, Organometallic hexahapto functionalization of single layer graphene as a route to high mobility graphene devices, Adv. Mater. 25 (2012) 1131–1136.

[13] Z. Tang, L. Zhang, Ch. Zeng, T. Lin, B. Guo, General route to graphene with liquid-like behavior by non-covalent modification, Soft Matter. 8 (2012) 9214–9220.

[14] E. Bekyarova, S. Sarkar, F. Wang, M. E. Itkis, I. Kalinina, X. Tian, R. C. Haddon, Effect of covalent chemistry on the electronic structure and properties of carbon nanotubes and graphene, Acc. Chem. Res. 46 (2013) 65–76.

[15] Y-C. Hsieh, Y. Zhang, D. Su, V. Volkov, R. Si, L. Wu, Y. Zhu, W. An, P. Liu, P. He, S. Ye, R. R. Adzic, J. X. Wang, Ordered bilayer ruthenium–platinum core-shell nanoparticles as carbon monoxide-tolerant fuel cell catalysts, Nat. Commun. 4 (2013) article number: 2466.

[16] Y. Yang, Ch. Sun, Y. Ren, S. Hao, D. Jiang, New route toward building active ruthenium nanoparticles on ordered mesoporous carbons with extremely high stability, Sci. Rep. 4 (2013) article number: 4540.

[17] J. Guo, G. Sun, S. Sun, S. Yan, W. Yang, J. Qi, Y. Yan, Q. Xin, Polyol-synthesized PtRu/C and PtRu black for direct methanol fuel cells, J. Power Sources 168 (2007) 299–306.

[18] Z. Liu, X. Y. Ling, X. Su, J. Y. Lee, L. M. Gan, Preparation and characterization of Pt/C and Ptsingle bondRu/C electrocatalysts for direct ethanol fuel cells, J. Power Sources 149 (2005) 1–7.

[19] L. Jiang, G. Sun, X. Zhao, Z. Zhou, S. Yan, S. Tang, G. Wang, B. Zhou, Q. Xin, Preparation of supported PtRu/C electrocatalyst for direct methanol fuel cells, Electrochim. Acta 50 (2005) 2371–2376.

[20] Y. Chen, Y. Zhou, Y. Tang, T. Lu, Electrocatalytic properties of carbon-supported Pt-Ru catalysts with the high alloying degree for formic acid electrooxidation, J. Power Sources 195 (2010) 4129–4134.

[21] V. Radmilovic, H. A. Gasteiger, P. N. Ross, Structure and chemical composition of a supported Pt-Ru electrocatalyst for methanol oxidation, J. Catal. 154 (1995) 98–106.

[22] G. S. Chai, S. B. Yoon, J-S. Yu, J-H. Choi, Y-E. Sung, Ordered porous carbons with tunable pore sizes as catalyst supports in direct methanol fuel cell, J. Phys. Chem. B 108 (2004) 7074–7079.

[23] J.W. Guo, T. S. Zhao, J. Prabhuram, R. Chen, C. W. Wong, Preparation and characterization of a PtRu/C nanocatalyst for direct methanol fuel cells, Electrochim. Acta 51 (2005) 754–763.

[24] J.R.C. Salgado, R.G. Duarte, L. M. Ilharco, A. M. Botelho do Rego, A. M. Ferraria, M. G. S. Ferreira, Effect of functionalized carbon as Pt electrocatalyst support on the methanol oxidation reaction, Appl. Catal. B: Environ. 102 (2011) 496–504.

[25] G. Liu, H. Zhang, J. Hu, Novel synthesis of a highly active carbon-supported $Ru_{85}Se_{15}$ chalcogenide catalyst for the oxygen reduction reaction, Electrochem. Commun. 9 (2007) 2643–2648.

[26] N.M. Sánchez-Padilla, S.M. Montemayor, L.A. Torres, F.J. Rodríguez-Varela, Fast synthesis and electrocatalytic activity of M@Pt (M=Ru, Fe_3O_4, Pd) core-shell nanostructures for the oxidation of ethanol and methanol, Int. J. Hydrogen Energy 38 (2013) 12681–12688.

[27] N.M. Sánchez-Padilla, D. Morales-Acosta, M.D. Morales-Acosta, S.M. Montemayor, F.J. Rodríguez-Varela, Catalytic activity and selectivity for the ORR of rapidly synthesized M@Pt (M= Pd, Fe_3O_4, Ru) core-shell nanostructures, Int. J. Hydrogen Energy 39 (2014) 16706–16714.

[28] S. Agarwal, J. N. Ganguli, Hydrogenation by nanoscale ruthenium embedded into the nanopores of K-10 clay, RSC Adv. 4 (2014) 11893–11898.

[29] W. Chen, D. Ghosh, J. Sun, M. C. Tong, F. Deng, S. Chen, Dithiocarbamate-protected ruthenium nanoparticles: Synthesis, spectroscopy, electrochemistry and STM studies, Electrochim. Acta 53 (2007) 1150–1156.

[30] M. Wakisaka, S. Mitsui, Y. Hirose, K. Kawashima, H. Uchida, M. Watanabe, Electronic structures of Pt−Co and Pt−Ru alloys for CO-tolerant anode catalysts in polymer electrolyte fuel cells studied by EC−XPS, J. Phys. Chem. B 110 (2006), 110, 23489–23496.

[31] J. Datta, S. Sen Gupta, S. Singh, S. Mukherjee, M. Mukherjee, Significant Role of Ru-Oxide Present in the Pt-Ru Alloy Catalyst for Ethanol Electro-Oxidation in Acid Medium, Mater. Manuf. Processes 26 (2011) 261–271.

[32] F. J. Rodríguez Varela, O. Savadogo, Catalytic activity of carbon-supported electrocatalysts for direct ethanol fuel cell applications, J. Electrochem. Soc. 155 (2008) 155, B618–B624.

[33] D. C. Azevedo, W. H. Lizcano-Valbuena, E. R. Gonzalez, An impedance study of the rate determining step for methanol oxidation on platinum and platinum-ruthenium supported on high surface area carbon, J. New. Mat. Electrochem. Systems 7 (2004) 191–196.

[34] H. R. Corti, E. R. Gonzalez, in Direct alcohol fuel cells materials performance, Durability and Applications, Springer Science, New York, USA 2014.

[35] E. R. Gonzalez, A. Mota-Lima, in Direct alcohol fuel cells materials performance, Durability and Applications (Eds: H.R. Corti, E.R. Gonzalez), Springer Science, New York, USA 2014, 33.

[36] E. Ticanelli, J.G. Beery, M.T. Paffett, S. Gottesfeld, An electrochemical, ellipsometric, and surface science investigation of the PtRu bulk alloy surface, J. Electroanal. Chem. Interfacial Electrochem. 258 (1989) 61–77.

Chapter VII

7. Development of high performance Pt/C electrocatalysts for Methanol Oxidation Reaction (MOR) based on RGO functionalization with Ru–compounds

7.1 Physicochemical characterization of $RGO_{Ru\text{-}dim}$, RGO_{Rucym}, $RGO_{Ru\text{-}com}$ and RGO.

7.1.2 FT–IR

Figure 7.1 shows the FT–IR spectra of non–functionalized *RGO* and functionalized supports with the different Ru compounds. *RGO* displays absorption bands at 1450 cm^{-1} corresponding to C=C bonds vibrations commonly expected from graphitic lattices. It also shows absorption bands assigned to C–O and C–OH bonds with vibrational frequencies at 1091 and 1023 cm^{-1}, respectively [1]. The weak C=O absorption bands (1740–1720 cm^{-1}), and those of the O–O and H–H functional groups (4000–3000 cm^{-1}), as well as the absence of a strong vibrations due to the –OH groups, may be attributed to the inherent deoxygenation of the nanostructured RGO material [2, 3].

From the FT–IR spectra of $RGO_{Ru\text{-}dim}$, the absorption band at 1267 cm^{-1} assigned to C–O–H bonds is observed, evidencing the presence of hydroxy–ethoxy ($HOCH_2CH_2O$–) fragments from the arene ring characteristic of the chemical structure of the Ru compounds. Moreover, increased intensity of the absorption band attributed to C=C bonds (1450 cm^{-1}) suggests the inclusion of the arene ligands into the RGO lattice preserving the sp^2 hybridization with π-stacking interactions intrinsic of graphitic structures [4]. Additionally, the spectra of $RGO_{Ru\text{-}dim}$ exhibits absorption bands of C-Cl bond at 793 cm^{-1}, yet demonstrating the presence of Cl ligands in this support.

On the other hand, $RGO_{Ru\text{-}cym}$ depicts weak signals due to C–H absorption bonds in the 1426–1291cm^{-1} range, attributed to energy vibrations of the (–$CHMe_2$) and (–Me) alkyl groups with presence in the cymene ligand [5]. It is worth noticing that the absorption energy of the C–Cl bond is relatively higher in the case of $RGO_{Ru\text{-}cym}$ compared to $RGO_{Ru\text{-}dim}$. Such characteristic may be due to the formation of C–Cl intermediates at $RGO_{Ru\text{-}cym}$ during the functionalization, suggesting the promotion of Ru–C bonds in its graphitic lattice. Meanwhile, the $RGO_{Ru\text{-}com}$ spectrum recorded has signals similar to those of non-functionalized *RGO*. Finally, it should be mentioned that all nanostructured carbon supports show at least one signal in the 3400–2800 cm^{-1} interval, due to the absorption energy of C=C and C–H bonds of the graphitic structure and lattice defects, of pristine *RGO* [2,6].

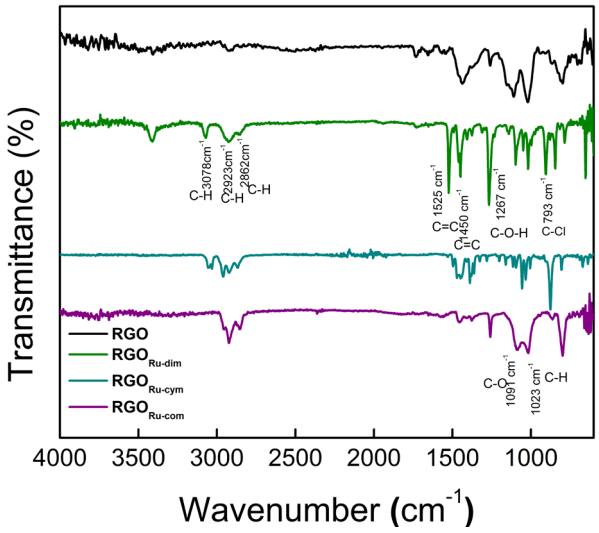

Figure 7.1 FT–IR spectra of non-functionalized *RGO*, $RGO_{Ru\text{-}dim}$, $RGO_{Ru\text{-}cym}$ and $RGO_{Ru\text{-}com}$.

7.1.3 Raman

The Figure 7.2 a) is the Raman spectrum and the corresponding deconvolution of *RGO* with the signal at 1347.36 cm^{-1} assigned to the D-band, attributed to defects in the graphitic edges due to sp^3 (C–O) and sp^2 (C=O) hybridization [7]. The D*, D´and D´´ signals in the 800 to 1750 cm^{-1} interval are attributed to the inherent oxygen contained in the graphitic lattice of RGO [8–10]. The G–band in 1580.52 cm^{-1} is attributed to sp^2 hybridization of carbon rings (ν C=C) in RGO. The presence of the D+D´ and D+G signals in the 2400–2750 cm^{-1} range is assigned to sp^2 hybridization provoked by C=O electronic interactions, creating lattice disorder. The wide 2D signals at 2675 cm^{-1} suggests that the RGO nanostructure is integrated by only few layers [7, 9]. The I_D/I_G ratio of RGO is 1.17, indicating disorder in nanostructured carbon.

Figure 7.2 b) is recorded the deconvolution of the Raman spectrum of $RGO_{Ru\text{-}dim}$, is important to notice the presence of D–signals with different shape and shifted to higher frequencies relative to *RGO*, an indication that oxygen defects may have been substituted by *Ru–dim* during functionalization process. $RGO_{Ru\text{-}dim}$, shows similar characteristics as those of RGO but with an increase relative intensity of the G–band therefore generating an I_D/I_G ratio of 0.79. This behavior suggests rearrangements in the structure of the carbon due to constructive rehybridization, preserving the sp^2 graphitized lattice, an effect attributed to the functionalization with the Ru compound, in agreement with the observations reported previously for Vulcan [11]. Furthermore, Figure 7.2 c) exhibit the deconvolution of the Raman spectrum of $RGO_{Ru\text{-}cym}$ similar to $RGO_{Ru\text{-}dim}$ support, the D–signals show the same behavior in the change of shape and shifting, suggesting the effect of substitution of *Ru–cym* to oxygenated species during functionalization. In the case of $RGO_{Ru\text{-}cym}$, there is an increase

in the relative intensity of its G–band and then I_D/I_G= 1.08. As in the case of *RGO*$_{Ru–dim}$, the surface modification with the organometallic preserves the graphitic hybridization.

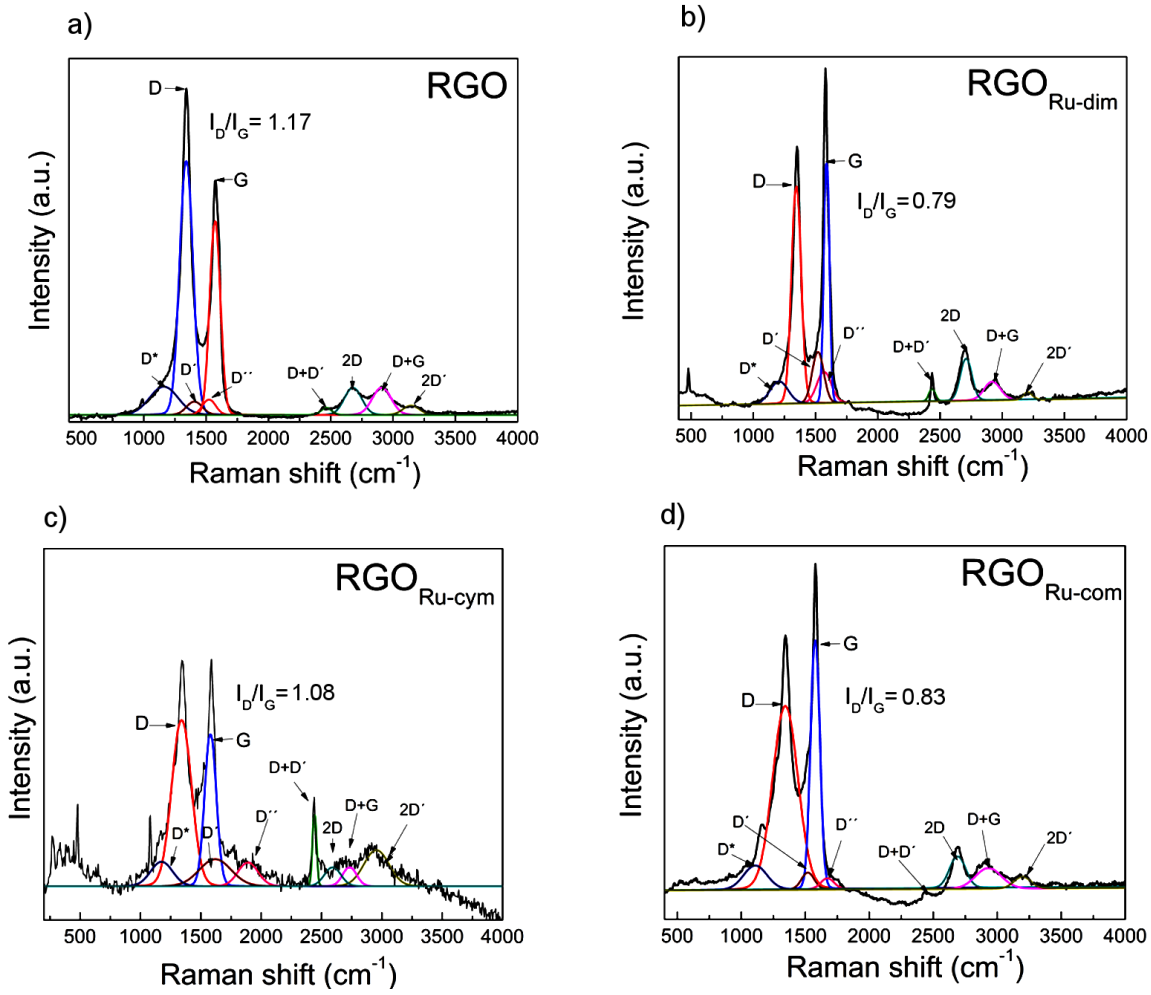

Figure 7.2 Raman spectra of nanostructured carbon supports: a) *RGO*, b) *RGO*$_{Ru-dim}$, c) *RGO*$_{Ru-cym}$ and d) *RGO*$_{Ru-com}$.

Meanwhile, in Figure 7.2 d) is displayed the spectrum of deconvolution signals to *RGO*$_{Ru-com}$, shows similitude to functionalized supports; D–signals with different shape and shifted to higher frequencies relative, a wide D–band at ~1347 cm^{-1} and a high-intensity G–band, reaching an I_D/I_G ratio of 0.83. Therefore, functionalization with the commercial Ru compound also results on the preservation of the sp^2 graphitized lattice, as in the case of the organometallic complexes [10].

7.1.4 SEM –EDS

Figure 7.3 exhibits the morphology of a) non–functionalized *RGO*, with multiple layers similar to those reported in the literature [12], b) *Ru–dim* and c) *Ru–cym* both showing large irregular–shaped crystals in their morphology. Figure 7.4 displays SEM images of: a) $RGO_{Ru\text{-}dim}$, b) $RGO_{Ru\text{-}cym}$, and c) $RGO_{Ru\text{-}com}$. It can be observed that all of functionalized supports have mixed morphology of *RGO* layers along with crystals (*Ru–dim* and *Ru–cym*) or particles (in the case of *Ru–com*).

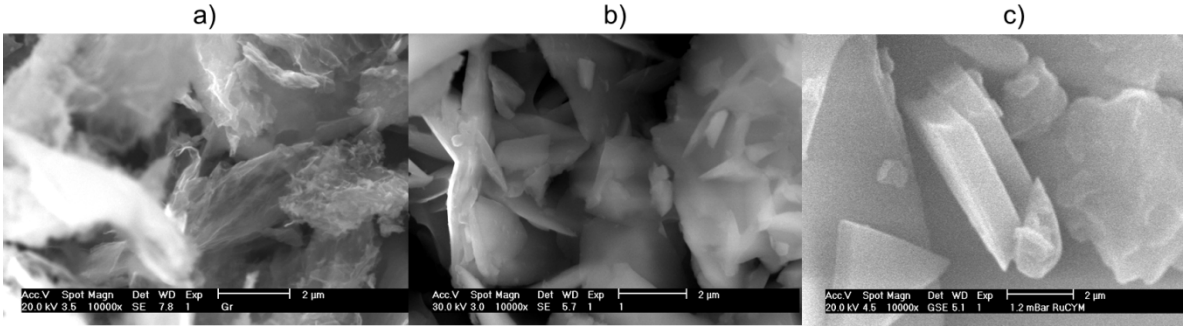

Figure 7.3 SEM micrographs of a) *RGO*, b) *Ru-dim* and b) *Ru-cym*.

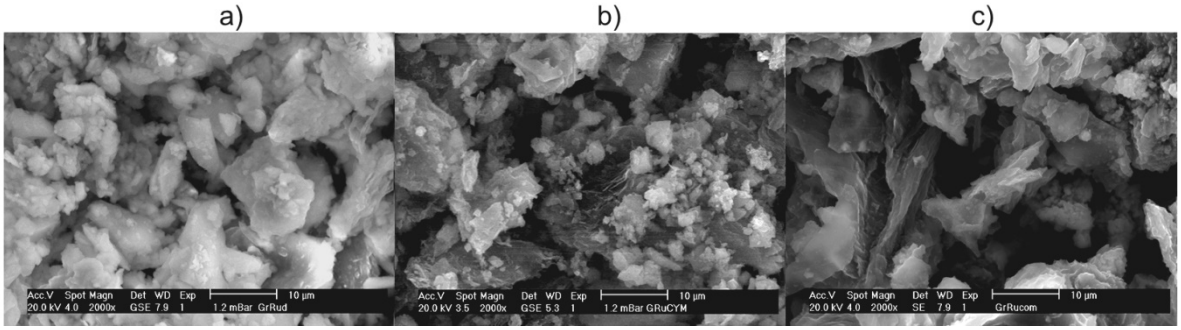

Figure 7.4 SEM micrographs of a) $RGO_{Ru\text{-}dim}$, b) $RGO_{Ru\text{-}cym}$ and c) $RGO_{Ru\text{-}com}$.

The chemical composition by EDS of $RGO_{Ru\text{-}dim}$, $RGO_{Ru\text{-}cym}$ and $RGO_{Ru\text{-}com}$ is reported in Table 7.1. Focusing on the Ru content, *Ru–dim* and *Ru-cym* show a concentration of 21.47 and 20.64 wt. %, respectively. The Ru content at $RGO_{Ru\text{-}dim}$ is ~4% higher than that reported previously in the case of Vulcan functionalized with the same compound under similar conditions ($C_{Ru\text{-}dim}$, with 17.24 wt. %) [11], suggesting an increase of ruthenium atoms

coordinated with the graphitic structure of RGO, which may be related to its higher surface area. Meanwhile, the Ru content at $RGO_{Ru\text{-}com}$ is significantly less compared to the two other samples in Table 7.1. This outcome is similar to that observed for Vulcan functionalized with *Ru-com* ($C_{Ru\text{-}com}$, also in [11]) at which the Ru content is less than in the case of *Ru-dim*.

Table 7.1. Chemical composition of $RGO_{Ru\text{-}dim}$, $RGO_{Ru\text{-}cym}$ and $RGO_{Ru\text{-}com}$, from EDS analysis.

Support	C	Ru	O	Cl
		(wt. %)		
$RGO_{Ru\text{-}dim}$	53.54	21.47	7.83	17.61
$RGO_{Ru\text{-}cym}$	58.86	20.64	5.04	15.47
$RGO_{Ru\text{-}com}$	71.29	6.62	10.53	11.56

Therefore, these results suggest that the organometallic compounds coordinate more efficiently than the commercial salt with the graphitic structure of RGO (and Vulcan), giving as a result a higher Ru content. The carbon content has decreased due to the surface modification, being higher for $RGO_{Ru\text{-}com}$ (71.29 wt. %) compared to $RGO_{Ru\text{-}dim}$ and $RGO_{Ru\text{-}cym}$ (53.54 and 58.86 wt. % respectively). Moreover, the O and Cl content of each functionalized carbon nanostructure is shown in Table 7.1.

7.2 Physicochemical characterization of the Pt/RGO, $Pt/RGO_{Ru\text{-}dim}$, $Pt/RGO_{Ru\text{-}cym}$ and $Pt/RGO_{Ru\text{-}com}$ electrocatalysts

7.2.1 XRD and EDS

Figure 7.5 a) shows the XRD patterns of *RGO*, *Pt/RGO, $Pt/RGO_{Ru\text{-}dim}$, $Pt/RGO_{Ru\text{-}cym}$ and $Pt/RGO_{Ru\text{-}com}$*. The pattern of pristine RGO displays a prominent signal at 2θ= 26.52º attributed to the (002) crystal reflection of carbonaceous structures, in this case due to the reduced graphene oxide. Such feature differs from those of graphene oxide and graphite and has been reported in literature as "re–graphitized" carbon [13−15]. Moreover, the signal at 2θ=17.02º has been reported for graphitic nanostructures with lattice defects, a characteristic that corresponds with that of the *RGO* structures in this work [16, 17].
The crystallite size of *RGO* calculated with the aid of the Scherrer equation (described in Chapter VI) using the (002) crystal reflection is d=4.70 nm. The lattice parameter planar distance (D_{planar}) has been calculated employing the Bragg's law [18]:

Equation 7.1: $2D_{planar}Sin\theta_{max} = n\lambda_{\alpha 1}$

Where θ_{max} is the peak angle, n=1 and $\lambda_{\alpha 1}$ is the X-ray wavelength (1.54056 Å). The planar distance of RGO is d_{planar}= 0.336 nm, in good agreement with values reported in the literature for *RGO* [19].

Pt/RGO shows the typical signals assigned to polycrystalline fcc Pt with (111), (200), (220) and (311) reflections in 2θ positions at 39.96, 46.36, 67.87 and 81.70º, respectively [20]. The crystallite size (d) of Pt/RGO using (111) plane is 2.72 nm (see Table 7.2). At 2θ around 10°, the reflection is due to the contribution of the (111) and (200) fcc Pt planes.

Table 7.2 Structural parameters of RGO from (002) C reflection and Pt/RGO from (111) Pt reflection.

Material	**d (nm)**	**D_{planar} (nm)**
RGO	4.70	0.336
Pt/RGO	2.72	0.226

In contrast, *Pt/RGO$_{Ru\text{-}dim}$* exhibits significant changes relative to Pt/RGO, i.e. the (111) and (200) Pt planes seem to merge, provoking the formation of a wide peak in the in the 34 to 50° in 2θ range. Additionally, such wide peak overlaps with hcp and fcc Ru planes. Figure 7.5 b) displays the deconvolution of the peak, showing the contributions of the (100), (002) and (101) hcp Ru reflections, as well as the (111) fcc Ru peak. At higher angles, low–intensity reflections attributed to the (110) and (102) Ru planes can also be observed [21]. Moreover, as in the case of Vulcan in Chapter VI, the peak at nearly 9° can be attributed to the different hcp Ru crystal planes, as shown in Figure 7.5 c) [22]. These characteristics strongly suggest the formation of Pt–Ru alloyed phases at *Pt/RGO$_{Ru\text{-}dim}$*, with metallic Ru beings formed the organometallic compound in good agreement from [11].

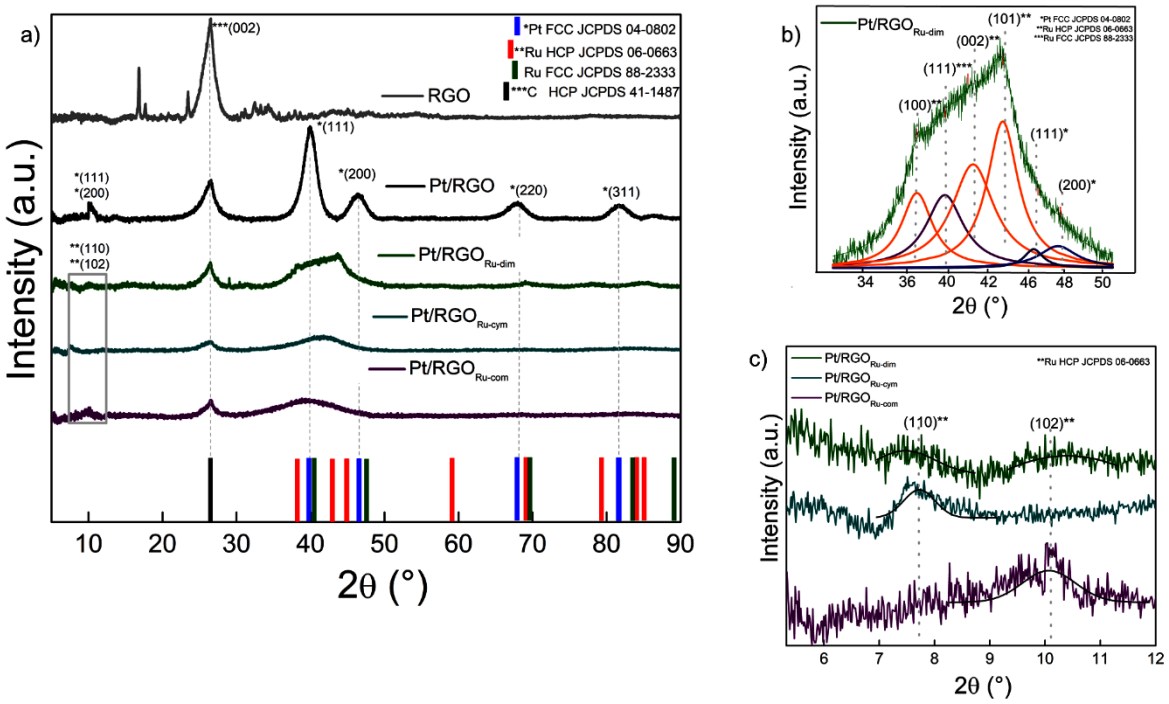

Figure 7.5 a) XRD patterns of *RGO*, *Pt/RGO*, *Pt/RGO$_{Ru-dim}$*, *Pt/RGO$_{Ru-cym}$* and *Pt/C$_{Ru-com}$*. b) Zooming of the 34–50° (2θ) range to *Pt/RGO$_{Ru-dim}$*. c) Zooming of the (110) and (102), hcp Ru reflections.

Similarly, the diffractogram of the *Pt/RGO$_{Ru-cym}$* and *Pt/RGO$_{Ru-com}$* electrocatalysts exhibit a wide peak in the 34 to 50° in 2θ range and a reflection in the interval between 8 and 13° (2θ) due to the hcp Ru structure [22]. Even though no peaks attributed to Ru planes can be detected at higher angles as in the case of *Pt/RGO$_{Ru-dim}$*, the structural characteristics of *Pt/RGO$_{Ru-cym}$* and *Pt/RGO$_{Ru-com}$* also suggest the formation of Pt–Ru alloys [23].

In the patterns of the Pt electrocatalysts, the signal at 17.02° is no longer detectable, probably due to interactions with the graphitic ring in the RGO lattice, in accordance with a consecutive rehybridization during functionalization previous to synthesis of catalysts [16]. Also, the relative intensity of the (002) reflection decreases at the Pt–supported electrocatalysts relative to *RGO*, a characteristic more evident in the case of *Pt/RGO$_{Ru-dim}$*, *Pt/RGO$_{Ru-cym}$* and *Pt/RGO$_{Ru-com}$*, it has not been possible to determine parameters such as crystallite size, lattice parameter and degree of alloying, as in the case when Vulcan has been used as support [11].

7.2 *SEM–EDS*

The chemical composition of the electrocatalysts obtained from EDS analysis is shown in Table 7.3. Pt/RGO has 20.20, 75.89 and 3.91 of Pt, C and O (wt. %), respectively. These values are in accordance with those nominally expected. The Pt content for $Pt/RGO_{Ru\text{-}dim}$, $Pt/RGO_{Ru\text{-}cym}$ and $Pt/RGO_{Ru\text{-}com}$ is 18.01, 16.02 and 22.52 wt. %, respectively, fairly close to the theoretical value of 20 wt. %. The higher Ru content has been determined for $Pt/RGO_{Ru\text{-}dim}$ (16.98 wt. %), followed by around 11 wt. % at $Pt/RGO_{Ru\text{-}cym}$ and $Pt/RGO_{Ru\text{-}com}$. Due to the presence of Ru, the amount of C decreases at $Pt/RGO_{Ru\text{-}dim}$, $Pt/RGO_{Ru\text{-}cym}$ and $Pt/RGO_{Ru\text{-}com}$, explaining in part the lower intensity of the (002) peak at these electrocatalysts, analogous to the behavior with Vulcan in Chapter IV. The Pt electrocatalysts supported on functionalized *RGO* also show O and Cl contents, the later because of the presence of the Ru organometallic compounds. The chemical composition of $Pt/RGO_{Ru\text{-}dim}$, $Pt/RGO_{Ru\text{-}cym}$ and $Pt/RGO_{Ru\text{-}com}$ demonstrates the stability of the Ru compounds as functionalization agents of the carbon support, since their main elements been detected after the synthesis by polyol method of the electrocatalysts.

Table 7.3 Chemical composition of all electrocatalysts from EDS analysis.

Electrocatalysts	C	Pt	Ru	O	Cl
			(wt. %)		
Pt/RGO	75.89	20.20	-	3.91	-
$Pt/RGO_{Ru\text{-}dim}$	52.09	18.01	16.98	12.04	0.88
$Pt/RGO_{Ru\text{-}cym}$	63.39	16.02	11.79	8.18	0.63
$Pt/RGO_{Ru\text{-}com}$	54.37	22.52	11.43	10.83	0.85

7.2.3 *HR–TEM*

HR–TEM analysis has been performed in order to evaluate the morphology of RGO used as support. Figure 7.6 a) shows the area for analyzed at *Pt/RGO* (red square) and the insert is the corresponding fast Fourier transform (FFT) pattern, from which a hexagonal lattice structure typical of graphitic nanostructures has been determined after inversing fast Fourier transform treatment (IFFT), as depicted in Figure 7.6 b) [24]. Figure 7.6 c) shows an image of $Pt/RGO_{Ru\text{-}com}$ with the FFT pattern (insert) attributed to a hexagonal symmetry due to the [001] diffraction pattern from the *RGO* support (red square) functionalized with the Ru-com compound [13, 25].

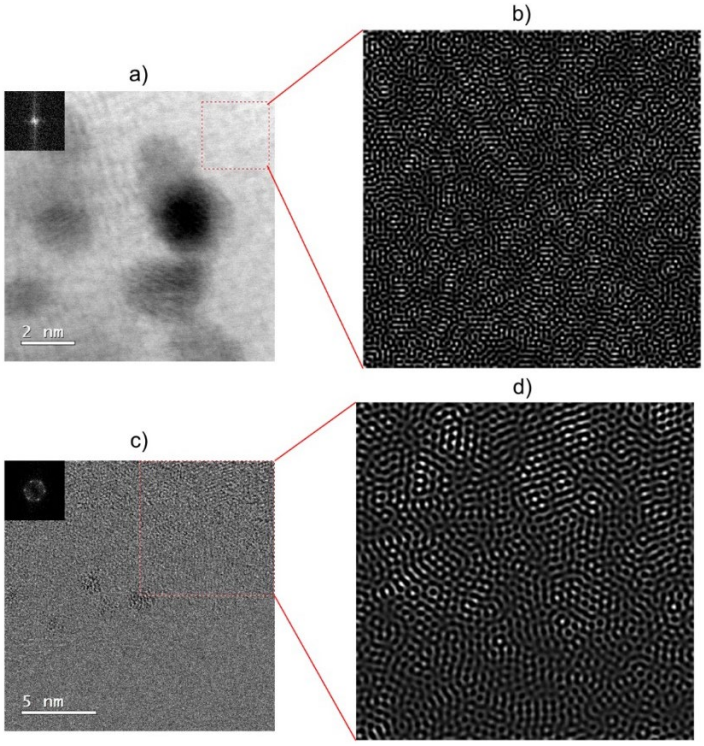

Figure 7.6 a) HR–TEM micrograph (insert: FFT SAED pattern) and b) IFFT image from the region in the red square *Pt/RGO*. c) Image of HR–TEM (insert: FFT pattern) and d) IFFT image from the region in the red square of $Pt/RGO_{Ru\text{-}com}$.

After performing IFFT analysis, the hexagonal structure shown in Figure 7.6 d) has been obtained. It is worth noticing that the *RGO* support in this sample has been submitted to functionalization and synthesis of electrocatalyst. Nevertheless, the graphitic structure preserves a hexagonal symmetry, similar to that of non-functionalized *RGO* in Figure 7.6 b). This behavior indicates the structural stability of *RGO* and suggests that the main process occurring during the polyol synthesis has been the attachment of Pt metallic nanoparticles.

Figure 7.7 a) displays a dark field image of the morphology of *Pt/RGO*. The bright dots are platinum nanoparticles that cover homogeneously the RGO support. The histogram in Figure 7.7 b) indicates an average particle size d= 2.59 nm (Table 7.4), in agreement with 2.72 nm value obtained from XRD analysis here–above. The HR–TEM micrograph in Figure 7.7 c) corroborates the nanostructured nature of Pt dispersed on *RGO* and also includes the FFT pattern from the nanoparticle in the red square. Further treatment of the FFT pattern allowed to obtain the masked IFFT image and the intensity profile shown in Figures 7.7 d) and e), respectively, where a distance between fringes of D_{planar}= 0.225 nm has been determined after averaging 10 planes (Table 7.4). Such value can be assigned to the Pt (111) plane [26, 27].

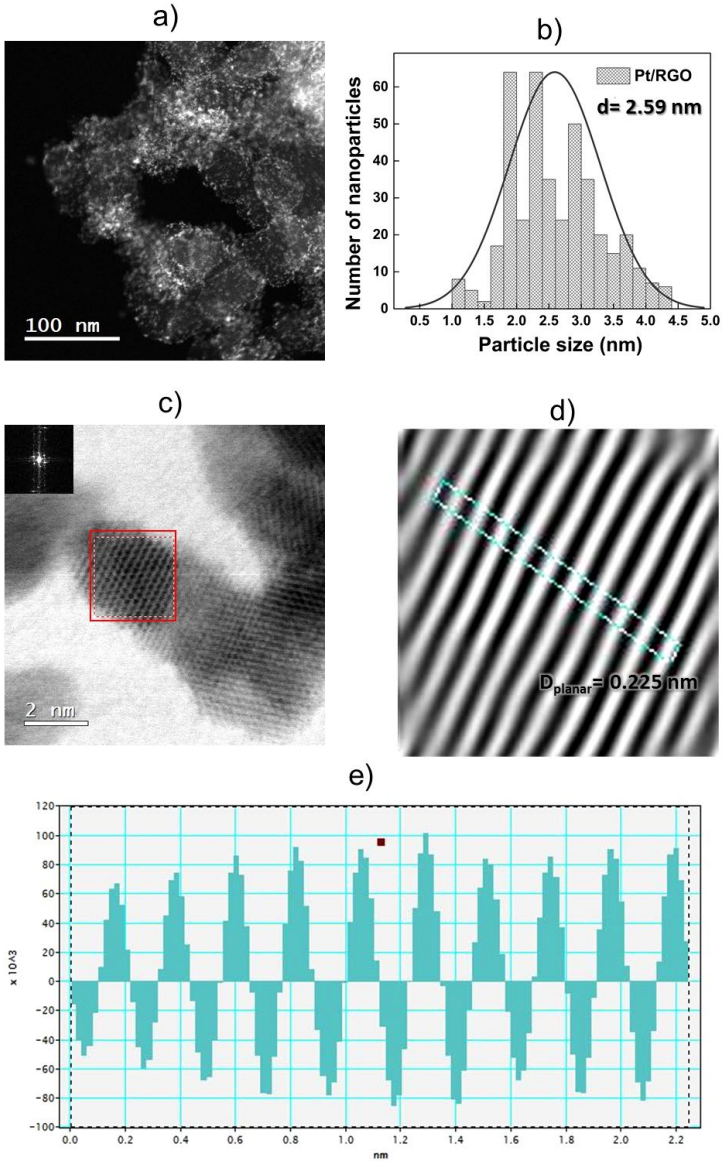

Figure 7.7 TEM analysis of Pt/RGO: a) micrograph showing the Pt nanoparticles dispersed over the support; b) histogram of particle size distribution; c) HR micrograph with FFT pattern from the region in the red square in the inset; d and e) IFFT image and intensity profile constructed from the FFT pattern, showing a distance between fringes (D_{planar}) of 0.225 nm.

Table 7.4 Structural parameters obtained from TEM analysis of electrocatalysts using Pt (111) reflection.

Electrocatalyst	d (nm)	D_{planar} (nm)
Pt/RGO	2.59	0.225
$Pt/RGO_{Ru\text{-}dim}$	2.04	0.201
$Pt/RGO_{Ru\text{-}cym}$	1.85	0.205
$Pt/RGO_{Ru\text{-}com}$	2.28	0.216

Figure 7.8 a) shows the morphology of $Pt/RGO_{Ru\text{-}dim}$ with Pt nanoparticles homogeneously dispersed over the *RGO* support. From the histogram in Figure 7.8 b) an average particle size d= 2.04 nm has been determined, a value smaller than that of Pt/RGO (see Table 7.4). Figure 7.8 c) is HR–TEM image of the electrocatalyst, with FFT pattern from the area marked with the red square in the insert. Additionally, Figures 7.8 d) and e) show the IFFT image and intensity profile from the FFT pattern, respectively, with a distance between planes of 2.01 nm (Table 7.4) assigned to the Pt (111) reflection. This value shows a decrease in distance compared to *Pt/RGO*, which suggests the formation of Pt–Ru alloyed phases due to the presence of metallic Ru nanoparticles at $Pt/RGO_{Ru\text{-}dim}$. The incorporation of ruthenium atoms modifies the structure of platinum, forming alloy [20, 28, 29]. This result supports the observations made after XRD analysis, particularly the wide peak between 34 and 50º (2θ). Moreover, the structural behavior of $Pt/RGO_{Ru\text{-}dim}$ correlates well with that of the $Pt/C_{Ru\text{-}dim}$ electrocatalysts in Chapter VI, at which the formation of Pt–Ru alloyed phases have been determined from XRD and XPS analysis. Thus, it may be concluded that the functionalization of RGO with Ru-dim also leads to the synthesis of a Pt–Ru electrocatalysts. In the case of $Pt/C_{Ru\text{-}dim}$ a degree of alloying of has been calculated after evaluation with Vegard´s Law. Unfortunately, it is not possible to perform such analysis from the XRD pattern of $Pt/RGO_{Ru\text{-}dim}$ in Figure 7.5.

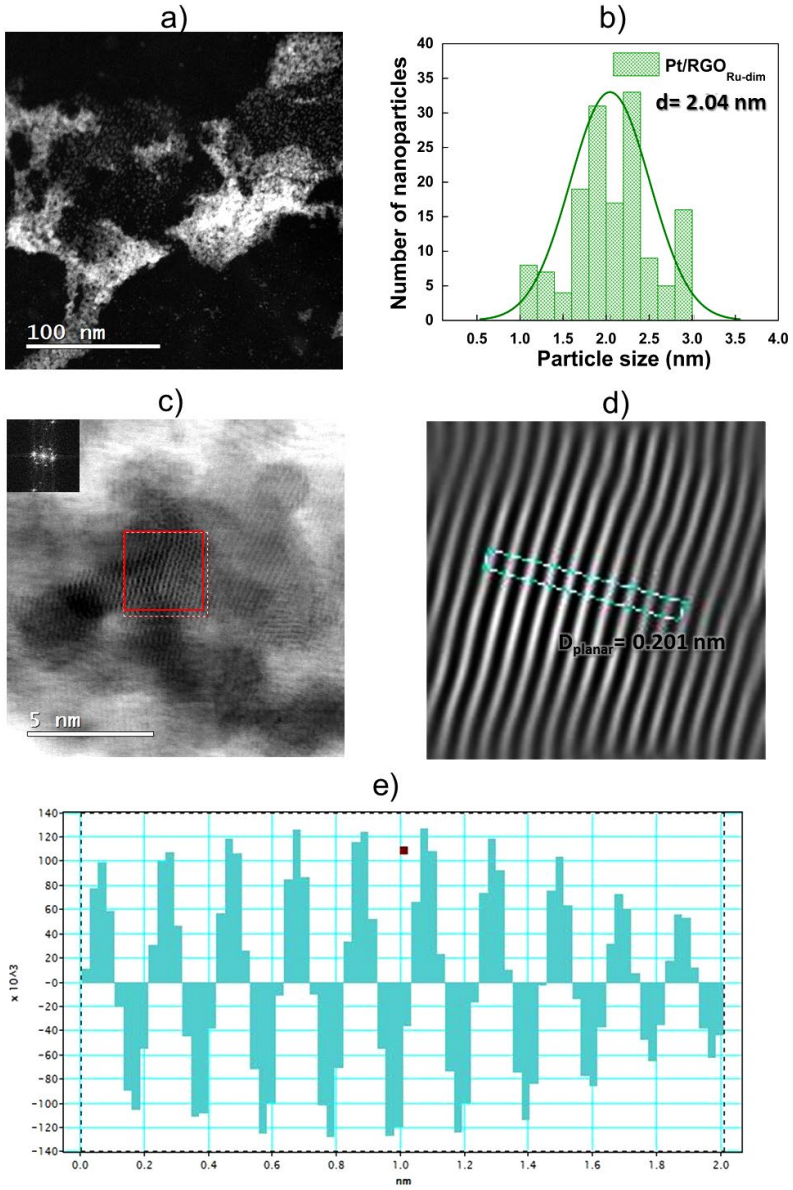

Figure 7.8 TEM analysis of *Pt/ RGO$_{Ru\text{-}dim}$*: a) micrograph showing the Pt nanoparticles dispersed over the support; b) histogram of particle size distribution; c) HR micrograph with FFT pattern from the region in the red square in the inset; d and e) IFFT image and intensity profile constructed from the FFT pattern, showing a distance between fringes (D_{planar}) of 0.201 nm.

Even more, the presence of Pt and Ru dispersed on RGO can be confirmed from the elemental chemical mapping in STEM mode of *Pt/RGO$_{Ru\text{-}dim}$*, in Figure 7.9.

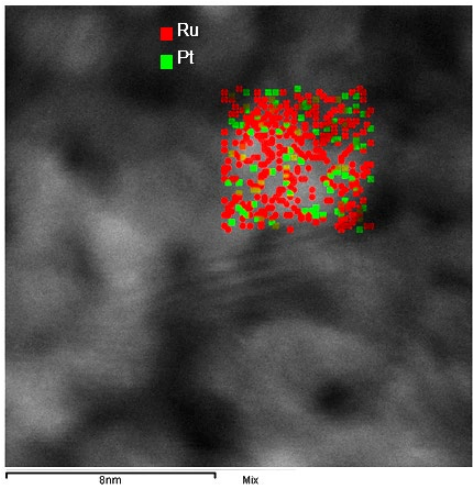

Figure 7.9 Elemental chemical mapping of *Pt/RGO*$_{Ru\text{-}dim}$.

Following the same analysis as in Figures 7.7 and 7.8, Figures 7.10 and 7.11 show the TEM characterization of *Pt/RGO*$_{Ru\text{-}cym}$ and *Pt/RGO*$_{Ru\text{-}com}$. Both electrocatalysts have a homogeneous dispersion of nanoparticles over the support. The particle size has been determined as 1.85 and 2.28 nm for *Pt/RGO*$_{Ru\text{-}cym}$ and *Pt/RGO*$_{Ru\text{-}com}$, respectively (Table 7.4). Also, from the corresponding SAED patterns, the distance between planes (D_{planar}) are 0.205 and 0.216 nm, for *Pt/RGO*$_{Ru\text{-}cym}$ and *Pt/RGO*$_{Ru\text{-}com}$, respectively, (Table 7.4).

From the TEM characterization, it can be seen that *Pt/RGO*$_{Ru\text{-}dim}$, *Pt/RGO*$_{Ru\text{-}cym}$ and *Pt/RGO*$_{Ru\text{-}com}$ have a smaller average particle size and distance between fringes of the (111) Pt plane, compared to *Pt/RGO* (Table 7.4). Among them, *Pt/RGO*$_{Ru\text{-}dim}$ shows the largest contraction, suggesting a higher degree of alloying between Pt and Ru metallic nanoparticles.

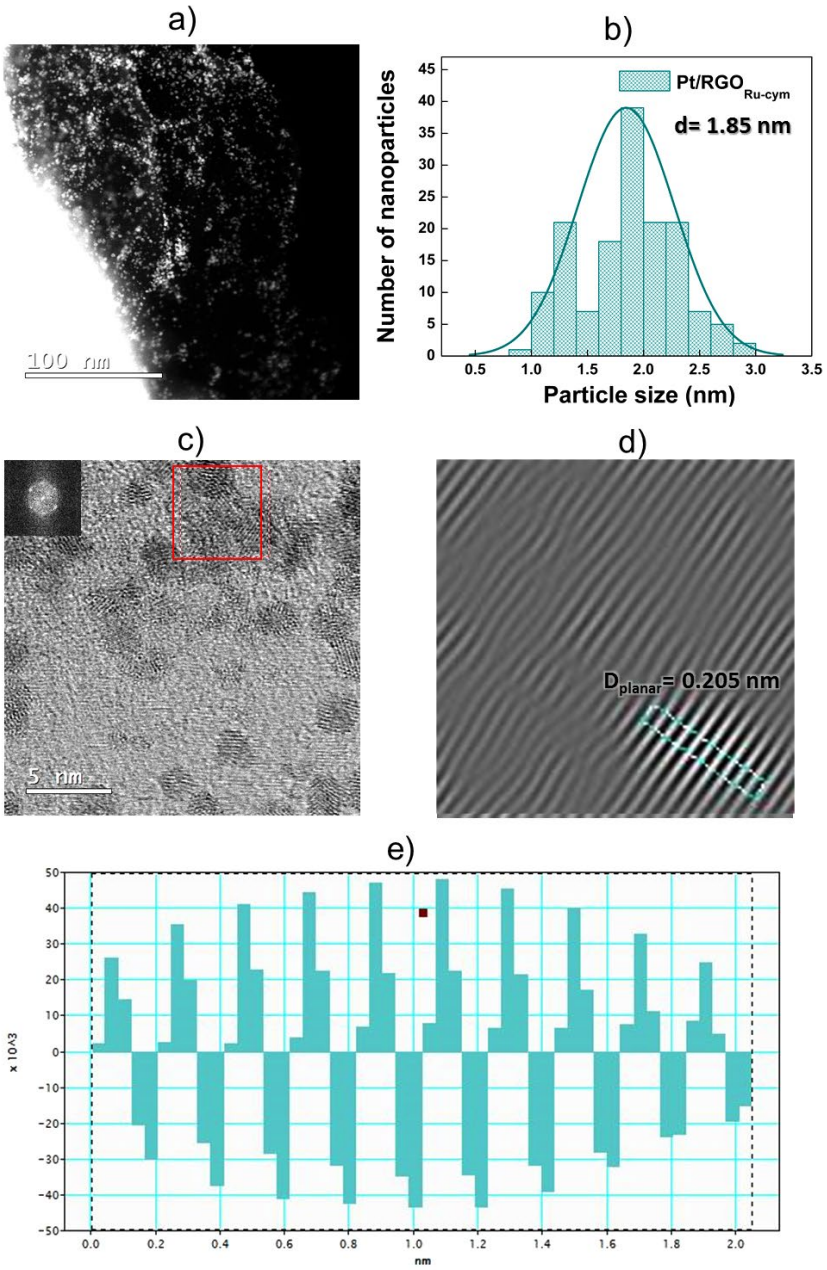

Figure 7.10 TEM analysis of *Pt/RGO*$_{Ru\text{-}cym}$: a) micrograph showing the Pt nanoparticles dispersed over the support; b) histogram of particle size distribution; c) HR micrograph with FFT pattern from the region in the red square in the inset; d and e) IFFT image and intensity profile constructed from the FFT pattern, showing a distance between fringes (D_{planar}) of 0.205 nm.

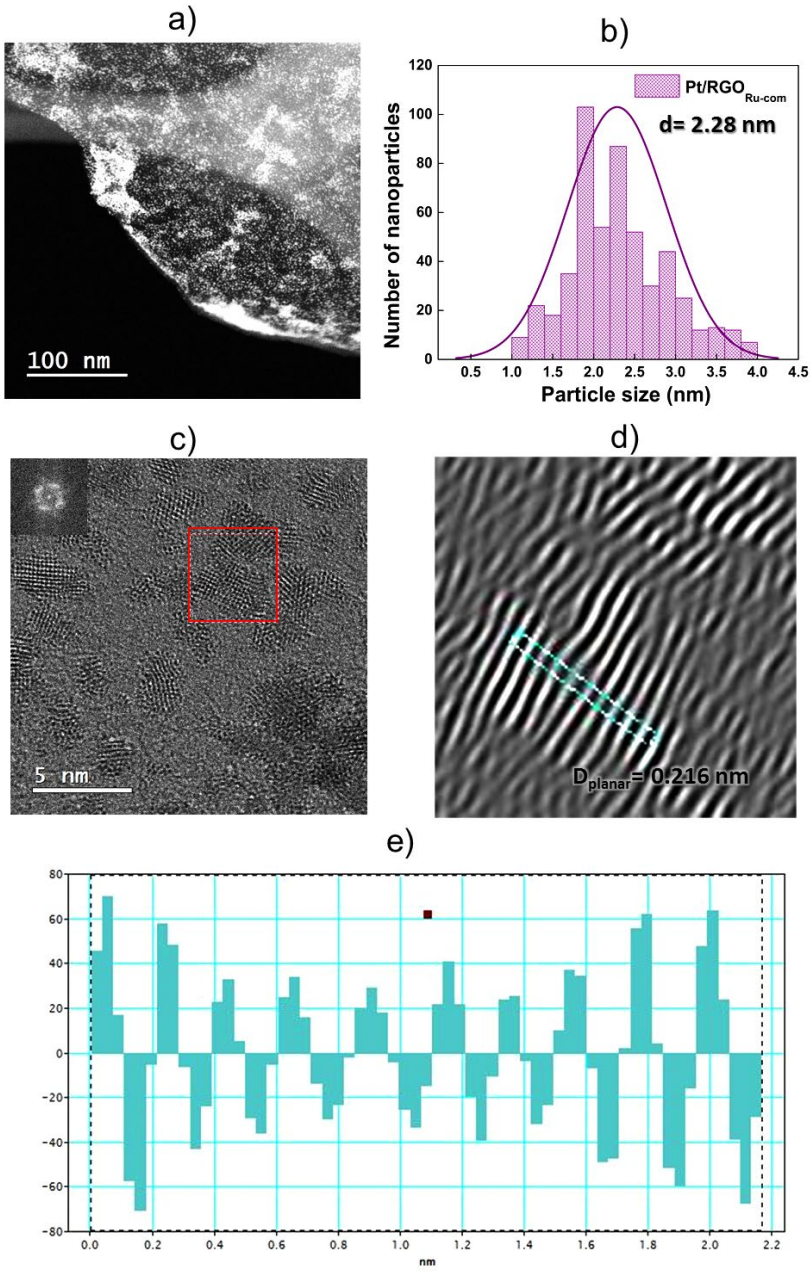

Figure 7.11 TEM analysis of *Pt/RGO*$_{Ru\text{-}com}$: a) micrograph showing the Pt nanoparticles dispersed over the support; b) histogram of particle size distribution; c) HR micrograph with FFT pattern from the region in the red square in the inset; d and e) IFFT image and intensity profile constructed from the FFT pattern, showing a distance between fringes of (D_{planar}) 0.216 nm.

7.2.4 *XPS*

In Figure 7.12 a), the C1s photoelectron emission region of Pt/RGO is shown. The carbon sp^2 hybridization at a binding energy (BE) of 284.81 eV is more intense than its sp^3 counterpart at BE= 286.20 eV. Several carbon species that can be ascribed to an RGO structure [30, 31] are displayed after deconvolution: C=C, C−C, C−O, C=O, O−C=O. Among them, the highest concentration is that of the C=C bonds, with 57.05 at. % (Table 7.5).

Figures 7.12 b−d) show the overlapping of the C1s BE and the Ru 3d spectra at *Pt/RGO*$_{Ru\text{-}dim}$, *Pt/RGO*$_{Ru\text{-}cym}$ and *Pt/RGO*$_{Ru\text{-}com}$, respectively. In the case of *Pt/RGO*$_{Ru\text{-}dim}$ and *Pt/RGO*$_{Ru\text{-}cym}$, their relative concentrations of Ru° species is higher compared to that of Ru^{IV}, while it is the opposite for *Pt/RGO*$_{Ru\text{-}com}$ (i.e., more RuO_2 than Ru at the later). On this issue, *Pt/RGO*$_{Ru\text{-}dim}$ and *Pt/RGO*$_{Ru\text{-}cym}$ have higher Ru° concentrations (4.36 and 7.81 at. %) than *Pt/RGO*$_{Ru\text{-}com}$ (4.87 at. %), as seen in Table 7.5. The spin−orbit splitting of the Ru species shown in Table 7.5 correlates well with those reported in the literature for ruthenium interacting with carbon [32, 33].

Figures 7.13 a−d) display the Pt 4f BE region of the electrocatalysts. Spin−orbit splitting (SOS) showing doublets due to the $4f_{7/2}$ and $4f_{5/2}$ states is observed in all cases. The signals can be ascribed to metallic Pt and PtO (Pt^0 and Pt^{II}, respectively). The highest Pt concentration has been determined for *Pt/RGO* (11.92 and 2.65 at. % Pt^0 and Pt^{II}, respectively, see Table 7.5). Meanwhile, the Pt concentration is relatively high at the other electrocatalysts. For Pt^0: 5.04, 4.23 and 4.43 (at. %) at *Pt/RGO*$_{Ru\text{-}dim}$, *Pt/RGO*$_{Ru\text{-}cym}$ and *Pt/RGO*$_{Ru\text{-}com}$, respectively. For the Pt^{II} species: 1.35, 0.67 and 0.62 (at. %) at *Pt/RGO*$_{Ru\text{-}dim}$, *Pt/RGO*$_{Ru\text{-}cym}$ and *Pt/RGO*$_{Ru\text{-}com}$, respectively. Thus, among the electrocatalysts supported on functionalized RGO, *Pt/RGO*$_{Ru\text{-}dim}$ has the highest concentration of Pt (6.39 at. %, Table 7.13). The Pt spin-orbit splitting are larger on *Pt/RGO* (3.26 and 3.80 eV), compared to the other electrocatalysts. Only *Pt/RGO*$_{Ru\text{-}cym}$ shows a larger splitting for Pt^{II} (3.82 eV).

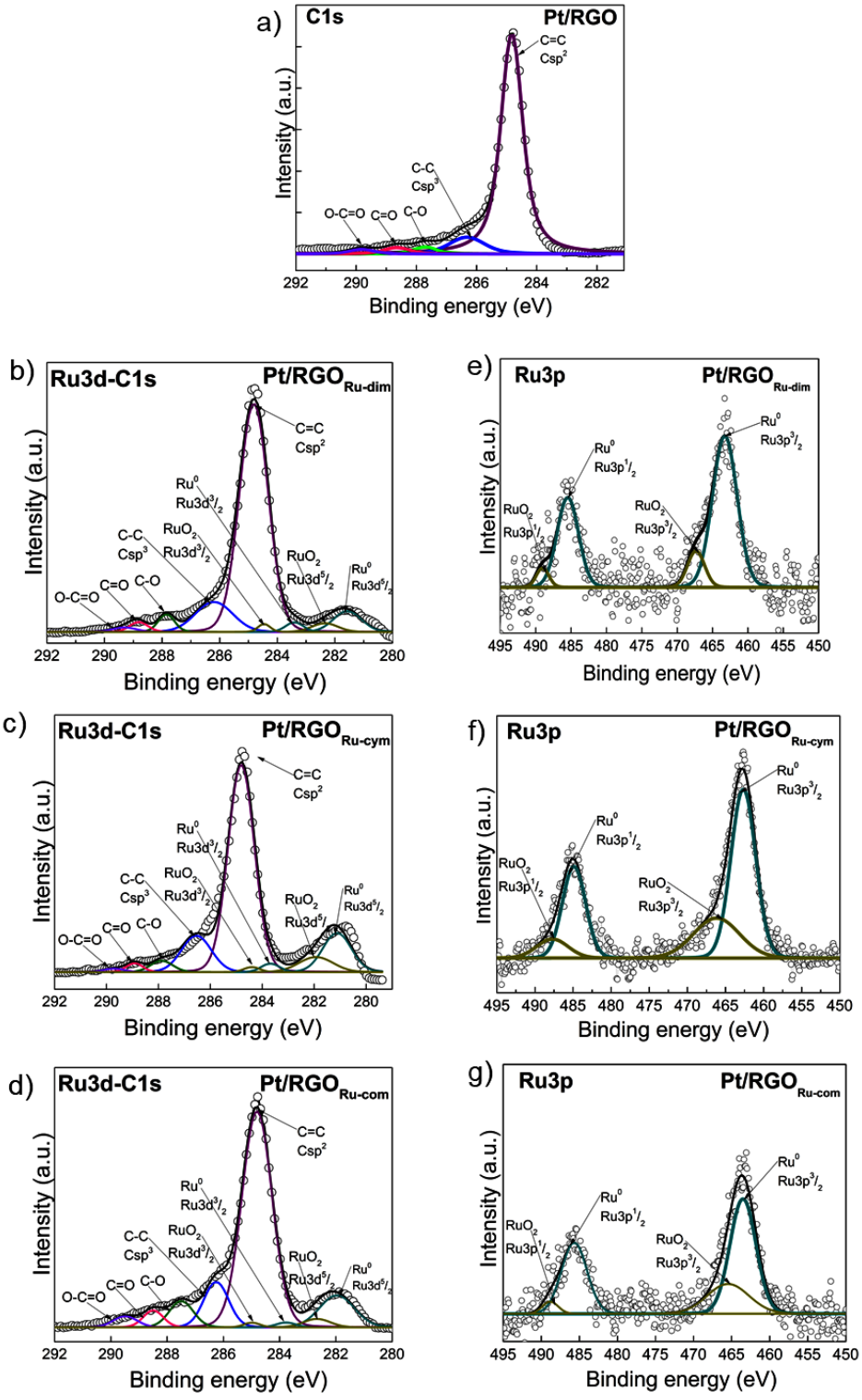

Figure 7.12 XPS spectra of the electrocatalysts: a) C1s region of *Pt/RGO*, b−d) Overlapped Ru3d-C1s regions of $Pt/RGO_{Ru\text{-}dim}$, $Pt/RGO_{Ru\text{-}cym}$ and $Pt/RGO_{Ru\text{-}com}$, e-g) Ru3p region of $Pt/RGO_{Ru\text{-}dim}$, $Pt/RGO_{Ru\text{-}cym}$ and $Pt/RGO_{Ru\text{-}com}$.

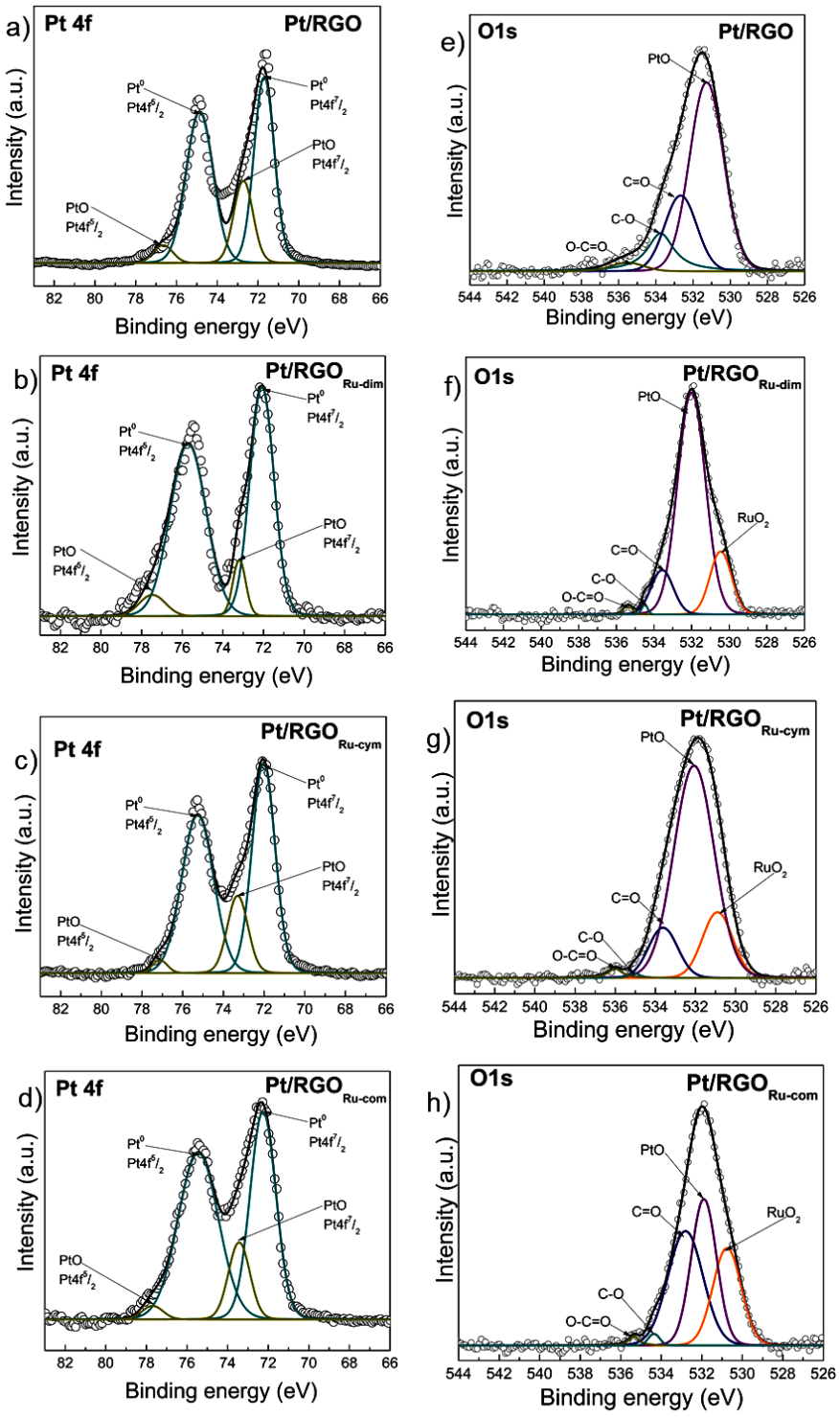

Figure 7.13 XPS spectra of *Pt/RGO, Pt/RGO*$_{Ru\text{-}dim}$*, Pt/RGO*$_{Ru\text{-}cym}$ and *Pt/RGO*$_{Ru\text{-}com}$: a−d) Pt 4f region, e−h) O1s region.

On the other hand, the BE of Pt^0 in the $4f_{7/2}$ state shifts from 71.58 eV in the case of Pt/RGO, to 72.27 eV for *Pt/RGO*$_{Ru\text{-}dim}$ (~0.7 eV displacement), 72.01 for *Pt/RGO*$_{Ru\text{-}cym}$ (~0.4 eV displacement) and 72.24 (~0.6 eV displacement) for *Pt/RGO*$_{Ru\text{-}com}$. Such behavior is attributed to the electronic modification of the electrocatalysts and corresponds to a change of the *d*-valence band of Pt, due to an electron transfer from Ru to Pt atoms. These shifts are considerable larger than those reported in Chapter VI for Pt/C$_{Ru\text{-}dim}$ and in reference [34] and therefore the formation of Pt–Ru alloyed phases can be confirmed due to the presence of Ru sites, after functionalization of RGO with either the organometallic compound or the commercial salt [35, 36].

Meanwhile, the O1s spectrum corresponding to Pt/RGO in Figure 7.13 e) exhibits the formation of the PtO, C=O, C−O and O−C=O species [37]. Additionally, the spectra of *Pt/RGO*$_{Ru\text{-}dim}$, *Pt/RGO*$_{Ru\text{-}cym}$ and *Pt/RGO*$_{Ru\text{-}com}$ in Figs. 7.13 f–h) show the presence of RuO_2, besides PtO, C=O, C−O and O−C=O. The XPS analysis indicates carbon sp^2 contents of 57.03, 54.70 and 53.25 (at. %) for *Pt/RGO*$_{Ru\text{-}dim}$, *Pt/RGO*$_{Ru\text{-}cym}$ and *Pt/RGO*$_{Ru\text{-}com}$, respectively, while that of *Pt/RGO* is 57.05 at. %. This composition shows a lower value of sp^2 species at non–functionalized *RGO* compared with non-functionalized Vulcan in Chapter VI (78.82 at. %) due to the intrinsic physicochemical characteristics of the graphene support. On the other hand, the sp^2 contents of the electrocatalysts supported on functionalized *RGO* are higher than those of *Pt/C*$_{Ru\text{-}dim}$ and *Pt/C*$_{Ru\text{-}com}$ (also in Chapter VI), suggesting an enhanced constructive rehybridization during functionalization of *RGO* with the different Ru compounds.

The higher concentration of Pt and Ru species, the shifting in the BE of doublets attributed to Pt 4f and Ru 3p, in addition with lower carbon concentration (see Table 7.5) to *Pt/RGO*$_{Ru\text{-}dim}$, suggest the similar behavior of *Pt/C*$_{Ru\text{-}dim}$ catalyst, promoting the higher electrocatalytic activity compared to *Pt/RGO*$_{Ru\text{-}cym}$, *Pt/RGO*$_{Ru\text{-}com}$ and *Pt/RGO*. The *Pt/RGO*$_{Ru\text{-}dim}$ electrocatalyst

Table 7.5. XPS parameters of the electrocatalysts.

Electrocatalyst	Species	State	BE (eV)	Doublet splitting (eV)	Composition (at. %)
Pt/RGO	Pt^0	Pt $4f_{7/2}$	71.58	3.26	4.82
		Pt $4f_{5/2}$	74.84		7.10
	PtO	Pt $4f_{7/2}$	72.70	3.80	2.04
		Pt $4f_{5/2}$	76.50		0.61
		O1s	531.26		7.74

	C=C	C1s	284.81		57.05
	C-C	C1s	286.20		5.26
	C-O	C1s	287.67		4.31
	C=O	C1s	288.90		2.67
	O-C=O	C1s	290.15		3.39
	C-O	O1s	532.65		2.93
	C=O	O1s	533.73		1.74
	O-C=O	O1s	535.52		0.34
$Pt/RGO_{Ru\text{-}dim}$	Pt^0	Pt 4f $_{7/2}$	72.27	3.24	2.94
		Pt 4f $_{5/2}$	75.51		2.10
	PtO	Pt 4f $_{7/2}$	74.00	3.25	1.11
		Pt 4f $_{5/2}$	77.25		0.24
		O1s	531.93		12.37
	Ru^o	Ru3p $_{3/2}$	463.26	22.44	1.82
		Ru3p $_{1/2}$	485.70		1.83
	RuO_2	Ru3p $_{3/2}$	467.22	21.76	0.47
		Ru3p $_{1/2}$	488.98		0.24
		O1s	530.44		2.73
	C=C	C1s	284.80		57.03
	C-C	C1s	286.18		9.72
	C-O	C1s	287.83		2.57
	C=O	C1s	288.79		1.62
	O-C=O	C1s	289.31		0.97
	C-O	O1s	533.55		1.98
	C=O	O1s	534.48		0.11
	O-C=O	O1s	535.36		0.15
$Pt/RGO_{Ru\text{-}cym}$	Pt^0	Pt 4f $_{7/2}$	72.01	3.24	1.74
		Pt 4f $_{5/2}$	75.25		2.49
	PtO	Pt 4f $_{7/2}$	73.28	3.82	0.57
		Pt 4f $_{5/2}$	77.10		0.10
		O1s	531.83		11.91
	Ru^o	Ru3p $_{3/2}$	462.62	22.23	2.85
		Ru3p $_{1/2}$	484.85		2.89
	RuO_2	Ru3p $_{3/2}$	466.14	21.54	1.25
		Ru3p $_{1/2}$	487.68		0.82
		O1s	530.88		2.75
	C=C	C1s	284.79		54.70
	C-C	C1s	286.53		10.77

	C-O	C1s	287.86		2.52
	C=O	C1s	288.90		1.50
	O-C=O	C1s	289.70		0.73
	C-O	O1s	533.60		2.05
	C=O	O1s	535.02		0.10
	O-C=O	O1s	535.99		0.26
$Pt/RGO_{Ru\text{-}com}$	Pt^0	Pt 4f $_{7/2}$	72.24	3.28	1.63
		Pt 4f $_{5/2}$	75.52		2.80
	PtO	Pt 4f $_{7/2}$	73.43	3.67	0.50
		Pt 4f $_{5/2}$	77.10		0.12
		O1s	531.88		6.04
	Ru^o	Ru3p $_{3/2}$	463.37	22.22	1.80
		Ru3p $_{1/2}$	485.59		1.88
	RuO_2	Ru3p $_{3/2}$	466.23	22.29	0.67
		Ru3p $_{1/2}$	488.52		0.52
		O1s	530.74		4.49
	C=C	C1s	284.79		53.25
	C-C	C1s	286.24		9.20
	C-O	C1s	287.48		5.16
	C=O	C1s	288.48		2.78
	O-C=O	C1s	289.47		2.19
	C-O	O1s	532.79		6.54
	C=O	O1s	534.34		0.21
	O-C=O	O1s	535.33		0.22

The XPS analysis indicates the stability in the at. % relative concentration of carbon sp^2 hybridization to functionalized electrocatalysts with 57.03, 54.70 and 53.25 at. % to *$Pt/RGO_{Ru\text{-}dim}$*, *$Pt/RGO_{Ru\text{-}cym}$* and *$Pt/RGO_{Ru\text{-}com}$*, respectively. Therefore, strongly suggests the contribution to constructive rehybridization process during functionalization procedure.

7.3 Electrochemical characterization of the Pt/RGO electrocatalysts.

The use of RGO as carbon support for fuel cell electrocatalysts represents advantages due to its high electronic conductivity and chemical stability. Additionally, the interaction between the *d*–orbitals of Pt atoms and π-orbitals of sp^2 hybridization of carbon atoms from RGO promotes an electronic modification of the metallic electrocatalyst. Moreover, the Ru atoms

participating as co-catalyst contribute to increase the catalytic activity for the MOR in acid media.

7.3.1 Catalytic activity of Pt/RGO$_{Ru\text{-}dim}$, Pt/RGO$_{Ru\text{-}cym}$, Pt/RGO$_{Ru\text{-}com}$ and Pt/RGO for the MOR.

Figure 7.14 shows the CVs of *Pt/RGO, Pt/RGO$_{Ru\text{-}dim}$, Pt/RGO$_{Ru\text{-}cym}$ and Pt/RGO$_{Ru\text{-}com}$* electrocatalysts, with: i) the typical hydrogen adsorption and desorption ($H_{ads/des}$) region at potentials between 0.05 and 0.3 V vs. SHE; ii) the double layer region in the potential interval of 0.3 to 0.6 V vs. SHE; iii) the Pt oxidation-reduction region in the potential of 0.6 to 1.2 V vs. SHE. The CV of *Pt/RGO* exhibits two peaks due to the H_{des} process in the 0.12–0.2 V vs. SHE range [38]. Additionally, its double layer is narrow. It also shows a current density slope in the positive scan starting at 0.8 V vs. SHE corresponding to the oxidation of Pt, along with a peak current density at ca. 0.79 V in the negative scan assigned to the reduction of Pt oxides [39]. The *Pt/RGO$_{Ru\text{-}com}$* electrocatalyst shows a broad $H_{ads/des}$ region without detectable peaks, a wider double layer region with a current density slope starting at about 0.6 V vs. SHE, and a Pt-oxides region not as well defined as in the previous case. These characteristics are typically observed for Pt-Ru/C alloys [39, 40], indicating that alloyed phases have been formed at *Pt/RGO$_{Ru\text{-}com}$*, in good agreement with the XPS analysis.

Meanwhile, the CVs of *Pt/RGO$_{Ru\text{-}dim}$* and *Pt/RGO$_{Ru\text{-}cym}$* have intense and broad $H_{ads/des}$ regions without peaks and a remarkable increase in the width of their double layer with a current density slope starting at about 0.3−0.4 V vs. SHE. Thus, the Pt–oxides formation/reduction region is not observed at these two electrocatalysts. These characteristics strongly suggest the formation of a Pt-Ru alloy when synthesizing the *Pt/RGO$_{Ru\text{-}dim}$* and *Pt/RGO$_{Ru\text{-}cym}$* electrocatalysts [40−42], and also confirm the finding after XPS characterization.

Figure 7.15 b) depicts the polarization curves (mass catalytic activity, taking into account the Pt content at the electrodes determined by EDS) of the MOR at *Pt/RGO, Pt/RGO$_{Ru\text{-}dim}$, Pt/RGO$_{Ru\text{-}cym}$ and Pt/RGO$_{Ru\text{-}com}$*. Clearly, *Pt/RGO$_{Ru\text{-}dim}$* was obtained delivers the maximum higher mass current density (j_{mass}) of 491.49 mA mg^{-1}_{Pt}. followed by *Pt/RGO$_{Ru\text{-}com}$* (271.53 mA mg^{-1}_{Pt}) > *Pt/RGO$_{Ru\text{-}cym}$* (197.85 mA mg^{-1}_{Pt}) > *Pt/RGO* (108.92 mA mg^{-1}_{Pt}), as seen in Table 7.6.

The onset potential (E_{onset}) at *Pt/RGO$_{Ru\text{-}dim}$* is 0.26 V vs. SHE, notably more negative than the values obtained at the other electrocatalysts (Table 7.6). Furthermore, the highest j_f/j_b ratio is that of *Pt/RGO$_{Ru\text{-}dim}$*, (2.27, see Table 7.6). The electrochemical parameters from Figure 7.15 and given in Table 7.6 indicate that the mass catalytic activity for the MOR decreases in the

order *Pt/RGO*$_{Ru\text{-}dim}$ > *Pt/RGO*$_{Ru\text{-}com}$ > *Pt/RGO*$_{Ru\text{-}cym}$ > *Pt/RGO*. According of these results, it is confirmed that the electrocatalysts supported on *RGO* functionalized with Ru compounds (organometallic and commercial) have a higher mass catalytic activity for the MOR. Considering the organometallics, Ru-dim interacts with *RGO* and Pt more efficiently than *Ru−cym*, which is less active to promote the reaction even than the commercial Ru−com. However, it is evident that the catalytic activity for the MOR is increased by the presence of Ru atoms, either from the organometallics or the commercial salt, an effect attributed to the bifunctional mechanism as described in Chapters I and VI. This means that on *RGO* as in the case of Vulcan, $(OH)_{ads}$ species are also formed on the Ru sites (generated from the compounds) at low potentials and transported to the Pt sites, promoting the MOR at more negative potentials. Such mechanism is more evident when using the organometallic complex in *Pt/RGO*$_{Ru\text{-}dim}$.

A comparison of the catalytic performance of *Pt/RGO*$_{Ru\text{-}dim}$ for the MOR with similar electrocatalysts in the literature, indicates that its j_{mass} value is higher than that reported by Sharma *et al*. with a *Pt/RGO* anode containing 73.71 wt. % Pt (134.0 mA mg^{-1}_{Pt}), with a j_f/j_b ratio slightly lower here (2.62 in that work) [38]. Moreover, *Pt/RGO*$_{Ru\text{-}dim}$ delivered higher j_{mass} and j_f/j_b ratio than the *PtRu/RGO/PVP* and *PtRu/RGO* (30 wt. % PtRu in both cases) electrocatalysts (j_{mass}= 146 and 92.4 mA mg^{-1}_{Pt}; j_f/j_b: 1.87 and 1.78, respectively), reported by Bin et al. [40]. Thus, it can be concluded that *Pt/RGO*$_{Ru\text{-}dim}$ is a high-performance anode for the MOR.

Furthermore, as has been indicated in Chapter IV, CO_{ads} species poison the Pt catalytic sites, reducing the catalytic activity of Pt/C electrocatalyst. The use of *RGO* has been considered as an attractive option to increase the tolerance of Pt to CO_{ads} due to a metal-support effect, under which the on−set potential of the CO oxidation reaction shifts towards more negative potentials [43, 44]. Then, the Pt-active sites become free to continue with the reaction.

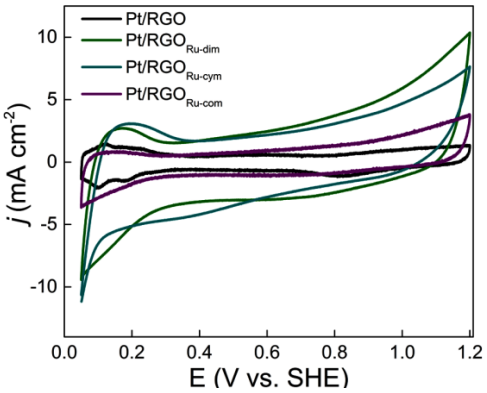

Figure 7.14 CVs of *Pt/ RGO, Pt/ RGO*$_{Ru\text{-}dim}$*, Pt/RGO*$_{Ru\text{-}cym}$ *and Pt/RGO*$_{Ru\text{-}com}$ in Ar-saturated 0.5 M H_2SO_4. Scan rate: 20 mV s^{-1}.

Figure 7.15 b) depicts the CO-stripping voltammograms of *Pt/RGO, Pt/RGO$_{Ru\text{-}dim}$, Pt/RGO$_{Ru\text{-}cym}$ and Pt/RGO$_{Ru\text{-}com}$*. The *Pt/RGO* electrocatalyst displays three peaks in the 0.65–0.85 V region, indicating that CO_{ads} species with different adsorption energy are being oxidized at different potentials [45]. The peak current density is j= 2.98 mA cm^{-2}, while E_{onset}= 0.65 V vs. SHE (Table 7.6). The presence of three peaks can be attributed to an electronic effect of the sp^2 hybridization of RGO on Pt nanoparticles, which favors to the adsorption and oxidation of CO_{ads} species at lower energies (i.e., more negative potentials) [43, 44].

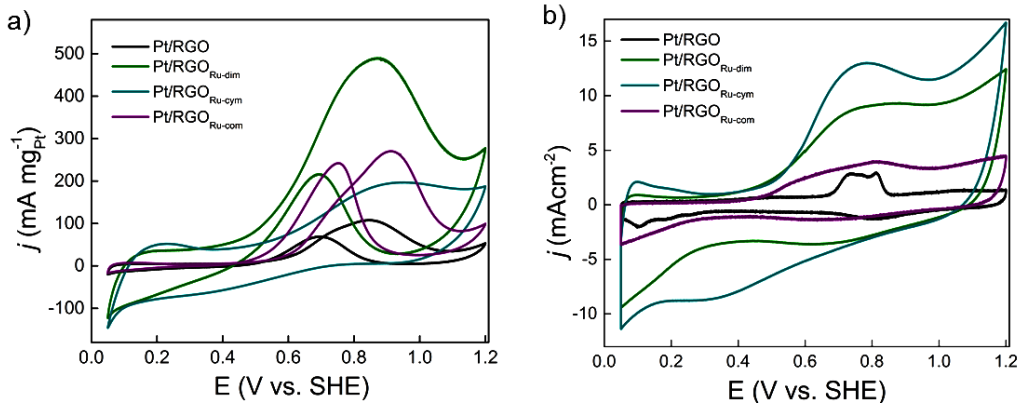

Figure 7.15 a) CVs of the ROM at *Pt/RGO, Pt/ RGO$_{Ru\text{-}dim}$, Pt/RGO$_{Ru\text{-}cym}$ and Pt/RGO$_{Ru\text{-}com}$*. Electrolyte: Ar–saturated 0.5 M H_2SO_4 + 0.5 M CH_3OH. Scan rate: 20 mV s^{-1}. b) CO–stripping curves for the electrocatalysts in 0.5 M H_2SO_4 at the same scan rate.

On the other hand, the electrocatalysts supported on functionalized RGO deliver higher j and more negative E_{onset} values compared to *Pt/RGO*: *Pt/RGO$_{Ru\text{-}dim}$* (9.31 mAcm^{-2} and 0.28 V), *Pt/RGO$_{Ru\text{-}cym}$* (13.07 mAcm^{-2} and 0.33 V) and *Pt/RGO$_{Ru\text{-}com}$* (4.01 mAcm^{-2} and 0.33 V), see Table 7.6. Accordingly, these results show the significant contribution of functionalizing RGO with Ru compounds to increase the tolerance of Pt nanoparticles to CO_{ads} species. In particular, E_{onset} of the CO oxidation is 0.28 V at *Pt/RGO$_{Ru\text{-}dim}$*, i.e., 370 mV more negative relative to *Pt/RGO*. Therefore, CO_{ads} is weakly adsorbed on *Pt/RGO$_{Ru\text{-}dim}$*, similar to the good performance shown by *Pt/C$_{Ru\text{-}dim}$* in Chapter VI, even though the E_{onset} value on *Pt/RGO$_{Ru\text{-}dim}$* is clearly more negative (0.48 V in Chapter VI). The high performance of *Pt/RGO$_{Ru\text{-}dim}$*, *Pt/RGO$_{Ru\text{-}cym}$* and *Pt/RGO$_{Ru\text{-}com}$* for the oxidation of CO can be in part attributed to the bifunctional mechanism, as indicated here-above for the MOR and in Chapter VI.

Table 7.6. Electrochemical parameters for *Pt/ RGO, Pt/ RGO$_{Ru\text{-}dim}$, Pt/RGO$_{Ru\text{-}cym}$ and Pt/RGO$_{Ru\text{-}com}$* during the MOR and the CO-stripping evaluation.

Electrocatalyst	**MOR**			**CO-Stripping**	
	j_{mass} (mA mg^{-1}_{Pt})	**E_{onset} (V)**	**j_f/j_b ratio**	**j (mA cm^{-2})**	**E_{onset} (V)**
Pt/RGO	108.92	0.40	1.54	2.98	0.65
Pt/RGO$_{Ru\text{-}dim}$	491.49	0.26	2.27	9.31	0.28
Pt/RGO$_{Ru\text{-}cym}$	197.85	0.37	-	13.07	0.33
Pt/RGO$_{Ru\text{-}com}$	271.53	0.38	1.12	4.01	0.37

Figure 7.16 shows the chronoamperometric (CA) curves of the MOR at the electrocatalysts. In all curves, *j* decays rapidly, a behavior that can be attributed to the formation of CO_{ads} and other carbonaceous intermediaries at the electrodes surface during the MOR. However, it is important to note that the Pt/RGO$_{Ru\text{-}dim}$ electrocatalyst exhibits a higher j over the test, demonstrating an enhanced stability for the MOR. On the contrary, Pt/RGO$_{Ru\text{-}cym}$ shows a poor stability for the reaction, with *j* values similar to those of *Pt/RGO*.

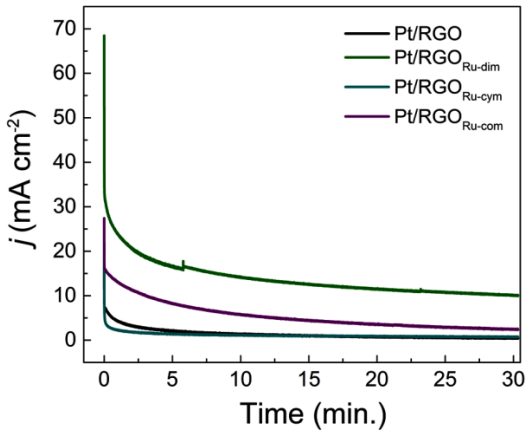

Figure 7.16 a) Chronoamperometric curves of the MOR at the *Pt/RGO, Pt/RGO$_{Ru\text{-}dim}$, Pt/RGO$_{Ru\text{-}cym}$ and Pt/RGO$_{Ru\text{-}com}$* electrocatalysts. Electrolyte: Ar-saturated 0.5 M H_2SO_4 + 0.5 M CH_3OH. Applied potential: 0.75 V vs. SHE.

As the results show, the *Pt/RGO$_{Ru\text{-}dim}$* electrocatalyst displays a clearly enhanced catalytic activity for the MOR and CO oxidation, compared to *Pt/RGO$_{Ru\text{-}cym}$*, *Pt/RGO$_{Ru\text{-}com}$* and *Pt/RGO*. Its high performance can be attributed to an electronic effect (alloying with Ru, as concluded from XPS analysis) and the bifunctional mechanism. A comparison between *Pt/RGO$_{Ru\text{-}dim}$* and *Pt/RGO$_{Ru\text{-}cym}$* shows that the former has more Pt^0 and P^{II} and thus a higher total Pt content (Table 7.5), which may have contributed to its higher catalytic activity. On the other hand, *Pt/RGO$_{Ru\text{-}cym}$* has a larger BE shift of the Pt $4f_{7/2}$ state (i.e., higher degree of alloying with Ru), and higher Ru^0 and RuO_2 contents. These characteristics provide *Pt/RGO$_{Ru\text{-}cym}$* with a high tolerance to CO_{ads}. However, its performance for the MOR is poor (even lower than that of *Pt/RGO$_{Ru\text{-}com}$*), which may be due to a low tolerance to other intermediate species generated during the oxidation of the alcohol (for example formaldehyde and formic acid).

Conclusions

Chapter VII

RGO was functionalized with the organometallic compounds $[(\eta^6–C_6H_5OCH_2CH_2OH)RuCl_2]_2$ (*Ru–dim*) and $[(\eta^6–C_6H_4(CHMe_2)Me)RuCl_2]_2$ (*Ru–cym*), to produce modified supports having several functional groups as identified by FT–IR. Raman analysis demonstrates the constructive rehybridization of ruthenium compounds over *RGO* structure preserving the sp^2 hybridization to functionalized supports: $RGO_{Ru\text{-}dim}$, $RGO_{Ru\text{-}cym}$ and $RGO_{Ru\text{-}com}$

$Pt/RGO_{Ru\text{-}dim}$ showed physicochemical characteristics that strongly suggest the formation of alloyed Pt–Ru phases.

- From XRD: shift in diffraction peaks, presence of reflections attributed to Ru, contraction at low angles at range 2θ of 5–10º and overlapping signals on interval 2θ of 34–50º.
- From TEM: chemical mapping showing the homogeneous dispersion of Pt and Ru nanoparticles, and decrease in grain size d= 2.05 nm and planar distance D_{planar}= 0.201 nm compared to Pt/RGO (d= 2.59 nm, D_{planar}= 0.225).

- From XPS: The identification of Ru^0 and RuO_2 bonds, besides those of Pt^0 and PtO. A shift to higher BE of Pt^0 in the $4f_{7/2}$ state similar to $Pt/C_{Ru\text{-}dim}$.

$Pt/RGO_{Ru\text{-}dim}$ showed a higher catalytic activity for the MOR considering the j, E_{onset} and j_f/j_b values. It also demonstrated a significant increased tolerance to CO_{ads} relative with reported to $Pt/C_{Ru\text{-}dim}$.

The physicochemical characterization of $Pt/RGO_{Ru\text{-}dim}$ exposes remarkable positive enhanced to catalytic activity compared to $Pt/RGO_{Ru\text{-}cym}$, despite using a support functionalized with organometallic complex Ru–cym.

References

Chapter VII

[1]Y. Gong, D. Li, Q. Fu, Ch. Pan, Influence of graphene microstructures on electrochemical performance for supercapacitors, Prog. Nat. Sci.: Mater. Int. 25 (2015) 379–385.

[2] V. Ţucureanu, A. Matei, A. M. Avram, FTIR spectroscopy for carbon family study, Crit. Rev. Anal. Chem. (2016) 1–19. doi: 10.1080/10408347.2016.1157013

[3] B. Mensah, D. Kumar, D-K Lim, S. G. Kim, B.-H. Jeong, Ch. Nah, Preparation and properties of acrylonitrile–butadiene rubber–graphene nanocomposites, J. Appl. Polym. Sci. 2015 42457 (1–12).

[4] P. K. Nayak Ed. Recent Advances in Graphene Research. E. Jimenez-Cervantes Amieva, J. López-Barroso, A. L. Martínez-Hernández, C. Velasco-Santos. In Graphene-Based Materials Functionalization with Natural Polymeric Biomolecules. INTECH, Singapore, (2016).

[5] Sh. Mori, T. Mochida, Organometallic ionic liquids from cationic arene−ruthenium complexes, Organometallics 32 (2013) 780–787.

[6] Z.Tang, L. Zhang, Ch. Zeng, T. Lina, B. Guo, General route to graphene with liquid-like behavior by non-covalent modification, Soft Matter. 8 (2012) 9214–9220.

[7] R. P. Antony, Preethi L.K., B. Gupta, T. Mathews, S. Dash, A.K. Tyagi, Efficient electrocatalytic performance of thermally exfoliated reduced graphene oxide-Pt hybrid, Mater. Res. Bull. 70 (2015) 60–67.

[8] S. Claramunt, A. Varea, D. López-Díaz, M. M, Velázquez, A. Cornet, A, Cirera, The importance of interbands on the interpretation of the raman spectrum of graphene oxide, J. Phys. Chem. C 119 (2015) 10123−10129.

[9] A. Kaniyoor, S. Ramaprabhu, A raman spectroscopic investigation of graphite oxide derived graphene, AIP Advances, 2 (2012) 032183 1–13.

[10] Q. A. Khan, A. Shaur, T. A. Khan, Y. F. Joya, M.S. Awan. Characterization of reduced graphene oxide produced through a modified Hoffman method, Cogent Chemistry, 3 (2017) 1298980 1−9.

[11] A. A. Siller-Ceniceros, M. E. Sánchez-Castro, D. Morales-Acosta, J. R. Torres Lubian, E. Martínez G, F. J. Rodríguez Varela, Innovative functionalization of Vulcan XC-72 with Ru organometallic complex: Significant enhancement in catalytic activity of Pt/C electrocatalyst for the methanol oxidation reaction (MOR), Appl. Catal., B. 209 (2017) 455−467.

[12] Ch. Yang, J. Shen, Ch. Wang, H. Fei, H. Bao, G. Wang, All-solid-state asymmetric supercapacitor based on reduced graphene oxide/carbon nanotube and carbon fiber paper/polypyrrole electrodes, J. Mater. Chem. A, 2 (2014) 1458–1464.

[13] P- Cui, J. Lee, E. Hwang, H. Lee, One-pot reduction of graphene oxide at subzero temperatures, Chem. Commun. 47 (2011) 12370–12372.

[14] Q. A. Khan, A.Shaur, T. A.Khan, Y. F. Joya, M.S. Awan, Characterization of reduced graphene oxidebproduced through a modified Hoffman method, Cogent Chemistry (2017) 3 1298980 1–9.

[15] W. Niu, L. Li, X. Liu, W. Zhou, W. Li, J. Lu, S. Chen, One-pot synthesis of graphene/carbon nanospheres/graphene sandwich supported Pt3Ni nanoparticles with enhanced electrocatalytic activity in methanol oxidation, Int. J. Hydrogen Energy, 40 (2015) 5106−5114.

[16] M. Aziz, F. S. Abdul Halim, J. Jaafar. Preparation and characterization of graphene membrane electrode assembly. Jurnal Teknologi 69 (2014) 11−14.

[17] Y. Devrim, A. Albostan, Graphene-supported platinum catalyst-based membrane electrode assembly for PEM fuel cell. J. Electron. Mater 45 (2016) 3900−3907.

[18] W. D. Callister Ed., Materials Science and Engineering 7th Ed. Chapher 3 The structure of crystalline solids, Jhon wiley & sons, Inc. New York (2007) 38–79.

[19] J-H. Yun, Y. H. Ng, R. J. Wong, R. Amal, Reduced graphene oxide: control of water miscibility, conductivity, and defects by photocatalysis, Chem. Cat. Chem. 5 (2013) 3060−3067.

[20] E. Antollini, F. Cadellini, Formation of carbon supported PtRu alloys: an XRD analysis, J Alloys Compd. 315 (2001) 118 –122.

[21] J. Liu, P. Bai, X. S. Zhao, Ruthenium nanoparticles embedded in mesoporous carbon microfibers: preparation, characterization and catalytic properties in the hydrogenation of D−glucose, Phys. Chem. Chem. Phys. 13 (2011) 3758−3763.

[22] Y. C. Hsieh, Y. Zhang, D. Su, V. Volkov, R. Si, L. Wu, Y. Zhu, W. An, P. Liu, P. He, S. Ye, R. R. Adzic, J. X. Wang, Ordered bilayer ruthenium-platinum core-shell nanoparticles as carbon monoxide-tolerance fuel cell catalyst, Nat. Commun. 4 (2013) article number: 2466.

[23] G. Yang, Y. Sun, P. Lv, F. Zhen, X. Cao, X. Chen, Z. Wang, Z. Yuan, X. Kong, Preparation of Pt–Ru/C as an Oxygen-reduction electrocatalyst in microbial fuel cells for wastewater treatment, Catalysts 6 (2016) 1−10.

[24] R. P. Antony, P. L. K., B. Gupta, T. Mathews, S. Dash, A. K. Tyagi, Efficient electrocatalytic performance of thermally exfoliated reduced graphene oxide-Pt hybrid, Mater. Res. Bull. 70 (2015) 60−67.

[25] C. Virojanadara, A. A. Zakharov, S Watcharinyanon, R Yakimova, L. I. Johansson, A low−energy electron microscopy and x-ray photo−emission electron microscopy study of Li intercalated into graphene on SiC(0001), New J. Phys. 12 (2010) article number: 125015.

[26] Z. Rong, Z. Sun, Y. Wang, J. Lv, Y. Wang, Selective hydrogenation of cinnamaldehyde to cinnamyl alcohol over graphene supported Pt–Co bimetallic, Catalysts Catal. Lett 144 (2014) 980−986.

[27] V. Radmilovic´, H. A. Gasteiger, P. N. Ross Jr. Structure and Chemical Composition of a Supported Pt-Ru Electrocatalyst for Methanol Oxidation. J Catal. 154 (1995) 98−106.

[28] S-A. Lee, K-W. Park, J-H. Choi, B-K. Kwon, Y-E. Sung. Nanoparticle Synthesis and Electrocatalytic Activity of Pt Alloys for Direct Methanol Fuel Cells. J Electrochem Soc. 149 (2002) A1299−A1304.

[29] E. S. Steigerwalt, G. A. Deluga, D. E. Cliffel, C. M. Lukehart, A Pt-Ru/graphitic carbon nanofiber nanocomposite exhibiting high relative performance as a direct-methanol fuel cell anode catalyst, J. Phys. Chem. B 105 (2001) 8097−8101.

[30] X. Wang, X. Zhang, X. He, A. Ma, L. Le, S. Lin, Facile electrodeposition of flower-like PMo_{12}-Pt/rGO composite with enhanced electrocatalytic activity towards methanol oxidation. Catalysts (2015) 5 1275−1288.

[31] J. V. Rojas, M. Toro−Gonzalez, M. C. Molina−Higgins, C. E. Castano, Facile radiolytic synthesis of ruthenium nanoparticles on grapheneoxide and carbon nanotubes, Mater. Sci. Eng. B 205 (2016) 28−35.

[32] P. Wanga, H. Liu, Q. Tan, J. Yang, Ruthenium oxide-based nanocomposites with high specific surface area and improved capacitance as a supercapacitor, RSC Adv. 4 (2014) 42839−42845.

[33] T. H. Thi−Vua, T. T. Thi−Trana, H. N. Thi−Lea, L. T. Trana, P. H. Thi−Nguyena, M. D. Nguyena, B. N. Quynh, Synthesis of Pt/rGO catalysts with two different reducing agents and their methanol electrooxidation activity, Mat. Res Bul. 73 (2016) 197–203.

[34] M. Wakisaka, S. Mitsui, Y. Hirose, K. Kawashima, H. Uchida, M. Watanabe, Electronic structures of Pt–Co and Pt–Ru alloys for CO-tolerant anodecatalysts in polymer electrolyte fuel cells studied by EC–XPS, J. Phys. Chem. B110 (2006) 23489–23496.

[35] E. A. Anumol, A. Halder, C. Nethravathi, B. Viswanath, N. Ravishankar, Nanoporous alloy aggregates: synthesis and electrocatalytic activity. J. Mater. Chem. 21 (2011) 8721–8726.

[36] K.I.B. Eguiluz, G.R.P. Malpass, G. Salazar Banda, L. Avaca, L.A. Avaca, Synthesis, characterization, and electrocatalytic activity toward methanol oxidation of carbon-Supported Pt_x–$(RuO_2$–$M)_{1-x}$ Composite Ternary Catalysts (M = CeO_2, MoO_3, or PbO_x), Energ. Fuel. 24 (2010) 4012–4024.

[37] R. Vinoth, S. G. Babu, V. Bharti, V. Gupta, M. Navaneethan, S. Venkataprasad Bhat, C. Muthanizhchelvan, P. C. Ramamurthy, Ch. Sharma, D. K. Aswal, Y. Hayakawa, B. N. Neppolian. Ruthenium based metallopolymer grafted reduced graphene oxide as a new hybrid solar light harvester in polymer solar cells, Scientific Reports 7:43133, doi: 10.1038/srep43133.

[38] S. Sharma, A. Ganguly, P. Papakonstantinou, X. Miao, M. Li, J. L. Hutchison, M. Delichatsios, S. Ukleja, Rapid microwave synthesis of CO tolerant reduced graphene oxide-supported platinum electrocatalysts for oxidation of methanol, J. Phys. Chem. C 114 (2010) 19459–19466.

[39] G. Vishwakshan-Reddy, P. Raghavendra, B. Ankamwar, P. Sri Chandana, S. M. Senthil-Kumard, L. Subramanyam Sarma, Ultrafine Pt–Ru bimetallic nanoparticles anchored on reduced graphene oxide sheets as highly active electrocatalysts for methanol oxidation, Mater. Chem. Front. 1 (2017) 757–766.

[40] D. Bin, F. Ren, H. Wang, K. Zhang, B. Yang, Ch. Zhai, M. Zhu, P. Yanga, Y. Du, Facile synthesis of PVP-assisted PtRu/RGO nanocomposites with high electrocatalytic performance for methanol oxidation, RSC Adv. 4 (2014) 39612–39618

[41] D. He, K. Cheng, T. Peng, X. Sun, M. Pan, Sh. Mu, Bifunctional effect of reduced graphene oxides to support active metal nanoparticles for oxygen reduction reaction and stability, J. Mater. Chem. 22 (2012) 21298–21304.

[42] X. Chen, D. He, H. Wu, X. Zhao, J. Zhang, K. Cheng, P. Wu, Sh. Mu, Platinized graphene/ceramics nano-sandwiched architectures and electrodes with outstanding performance for PEM Fuel Cells, Sci. Rep. 5 (2015) Article number: 16246.

[43] W. Huang, H. Wang, J. Zhou, J. Wang, P. N. Duchesne, D. Muir, P. Zhang, N. Han, F. Zhao, M. Zeng, J. Zhong, Ch. Jin, Y. Li, S.-T. Lee, H. Dai, Highly active and durable methanol oxidation electrocatalyst based on the synergy of platinum–nickel hydroxide–graphene, Nat. Commun. 6 (2015) Article number: 10035.

[44] P. Kanninena, N. D. Luong, L. H. Sinhb, J. Flórez-Montaño, H. Jiang, E. Pastor, J. Seppälä, T. Kallio, Highly active platinum nanoparticles supported by nitrogen/sulfur

functionalized graphene composite for ethanol electro-oxidation, Electrochim. Acta 242 (2017) 315–326.

[45] W. J. Pech–Rodríguez, D. González–Quijano, G. Vargas–Gutiérrez, C. Morais, T.W. Napporn and F. J. Rodríguez–Varela. Electrochemical and in situ FTIR study of the ethanol oxidation reaction on PtMo/C nanomaterials in alkaline media. Appl. Catal., B. 203 (2017) 654–662.

Academic production:

Journal publications

- **Evaluation of supported and unsupported Pd–CeO_2 nanostructured anode electrocatalysts for the formic acid and the glycerol oxidation reactions in acid media**.

A. Altamirano–Gutiérrez, A. M. Fernández, Kalasapurayil Kunhiraman Aruna, Ramasamy Manoharan, Palanisamy Karthikeyan, A. Siller–Ceniceros, P. Meléndez–González , P. Bartolo–Pérez , F. J. Rodríguez-Varela. J Appl. Electrochem. 45 (2015) 1195–1204.

- **Innovative functionalization of Vulcan XC-72 with Ru organometallic complex: Significant enhancement in catalytic activity of Pt/C electrocatalyst for the methanol oxidation reaction (MOR).**

A. A. Siller–Ceniceros, M. E. Sánchez–Castro, D. Morales–Acosta, J. R. Torres–Lubian, E. Martínez G, F. J. Rodríguez–Varela. Appl. Catal., B. 209 (2017) 455−467.

- **Easy synthesis of N-doped graphene by milling exfoliation with electrocatalytic activity towards the Oxygen Reduction Reaction (ORR)**

Juan C. Carrillo–Castillo, Ivonne L. Alonso–Lemus, A. A. Siller–Ceniceros, E. Martínez G., Pedro Pizá Ruiz, Gregorio Vargas–Gutiérrez, F. J. Rodríguez–Varela. Int. J. Hydrogen Energy, article in press (2017) 1−6.

- **Organometallic functionalization of RGO: Novel route to form Pt-Ru alloys as electrocatalyst for Methanol Oxidation Reaction.**

A.A. Siller-Ceniceros, M.E. Sánchez-Castro; D. Morales–Acosta, J.R. Torres–Luvian, E. Martínez–Guerra, Gregorio Vargas–Gutiérrez, F.J. Rodríguez–Varela. In preparation.

Distinctions

- ***Best poster prize** in **XIV International Congress of the Mexican Hydrogen Society**, 2014 in Cancún México.*
- ***Best poster prize** in **67th annual meeting of the international society of electrochemistry**, 2016 in The Hague, The Netherlands.*

Research stay

- Courses of: **Thoretical and practical of computational chemistry and molecular modeling** by Dr. Mario Sánchez Vázquez.

From 13 May – 16 June 2014 in the Centro de Investigación de Materiales Avanzados (CIMAV-Unidad Monterrey).

Congress

International

- **XIV International Congress of the Mexican Hydrogen Society 2014**.

From 30 September to 4 October 2014 in Cancún México. Poster Presentation of the work: **Theoretical study of Ru-organometallic compounds-functionalized graphene as catalyst supports for low-temperature fuel cells**.

- **67th annual meeting of the international society of electrochemistry**

From 21 to 26 August 2016 in The Hague, The Netherlands. Poster Presentation of the work: **Functionalization of Vulcan with Ru-compounds: novel Pt-Ru interactions to enhance the catalytic activity of Pt/C electrocatalyst for the Methanol Oxidation Reaction (MOR).** A.A. Siller−Ceniceros; M.E. Sánchez−Castro; J.R. Torres−Luvian; D. Morales−Acosta; E. Martínez−Guerra; F.J. Rodríguez−Varela.

- **XVI International Congress of the Mexican Hydrogen Society 2016**

From 27 to 30 September 2016 in Querétaro city, México. Oral presentation: **Organometallic functionalization of graphene: Novel route to form Pt-Ru alloys as electrocatalyst for Methanol Oxidation**

National

- **XXXI Congreso Nacional de la Sociedad Mexicana de Electroquímica 2016 and 9th Meeting of the Mexican Sction of the Electrochemical Society.**

From 30 May to 03 June 2016 in Universidad Autónoma de Nuevo León (UANL). Oral presentation: "**Funcionalización de Vulcan XC-72 con [(η^6-$C_6H_5OCH_2CH_2OH$)$RuCl_2$]$_2$ para su uso como soporte de nanoparticulas de Pt: novedosa generación de interacciones Pt-Ru para incrementar la actividad catalítica en la oxidación de metanol".**

- **1er Congreso de la Asociación de Carbono (AMEXCARB−2015)**

From 10−13 November 2015 in Instituto Potosino de Investigación Científica y Tecnológica (IPICYT). Poster presentation: "**Estudio de la Innovadora Funcionalización de Sistemas Carbonosos con el Compuesto Organometálico [(η^6-C_6H_5O CH_2CH_2OH)$RuCl_2$]$_2$"**.

- **7º Encuentro de Química Inorgánica (EQI-2015)**

From 22−25 September 2015in Camino Real Hotel (Saltillo, Coah.). Oral presentation: "**Funcionalización de Vulcan XC-72 con [(η^6-$C_6H_5OCH_2CH_2OH$)$RuCl_2$]$_2$ y su uso como soporte de nanoparticulas de Pt: novedosa generación de interacciones Pt-Ru para incrementar la actividad catalítica en la oxidación de metanol".**

Courses and workshop

- Course: **"Técnicas Electroquímicas en el dominio del tiempo y la frecuencia para la caracterización de procesos de corrosión" by PhD Homero Castañeda.** On 29 May 2016, 9th Meeting of the Mexican Sction of the Electrochemical Society. Universidad Autónoma de Nuevo León (UANL) Monterrey N. L. México.

- Course: "**CNT / polymer nanocomposites**" **by PhD. Peng-Cheng Ma.** From 11−14 October 2016, **"3er Taller de Nanomateriales y Nanocompuestos del Sureste"** Centro de Investigación científica de Yucatán (CICY), Mérida Yuc.

- Course: "**Multi-scale hybrid composites for Smart sensing**" **PhD. Erik Thostenson.** From 11−14 October 2016, **"3er Taller de Nanomateriales y Nanocompuestos del Sureste"** Centro de Investigación científica de Yucatán (CICY), Mérida Yuc.

- Course: "**Nanocellulose composites" Dr. Kristofer Gamstedt.** From 11−14 October 2016, **"3er Taller de Nanomateriales y Nanocompuestos del Sureste"** Centro de Investigación científica de Yucatán (CICY), Mérida Yuc.

- Workshop: "Nanoestructuras Funcionales para la Generación de Energía" by M.C. Adriana A. Siller Ceniceros and M. C. Anayantzin Hernández Ramírez. From 18−19 November 2014 at CINVESTAV Unidad Saltillo.

- Workshop: "X Escuela de Ciencia de Materiales y Nanotecnología−Morelia" (X−ECMyN) and "6to Foro de Vinculación Universidad−Industria" by Dr. Omar Solorza Feria, Dr. Luis Pérez Pozo, Dr. Raúl Valenzuela Monjarás and PhD. Robin Drew and Dr. Karina Suárez. From 3−7 Agoust 2015 at Instituto de Investigación en Materiales (UNAM Unidad Morelia). Morelia Mich.